Mechanical behavior of granular material considering particle breakage

Yuqi Zhang

To cite this version:

Yuqi Zhang. Mechanical behavior of granular material considering particle breakage. Mechanics of materials [physics.class-ph]. Université de Lorraine, 2018. English. NNT : 2018LORR0041 . tel-01811061

HAL Id: tel-01811061
https://theses.hal.science/tel-01811061

Submitted on 8 Jun 2018

École doctorale EMMA

THÈSE

Pour l'obtention du titre de :

DOCTEUR DE L'UNIVERSITÉ DE LORRAINE

Spécialité : ingénierie géotechnique

Présentée par : Yuqi ZHANG

Comportement mécanique du matériau granulaire en tenant compte de la rupture des particules

---

Thèse soutenue publiquement le janvier 2018 à Metz devant le jury composé de :

Pierre-Yves HICHER	Professor	Ecole Centrale de Nantes, France	Rapporteur
Belouettar SALIM	DR HDR	Luxembourg Institute of Science and Technology, Luxembourg	Rapporteur
Marion MARTINY	Professor	Université de Lorraine, France	Examinateur
Christophe DANO	MCF	l'Université Grenoble Alpes UGA, France	Examinateur
Nadia BENAHMED	Chargé de Recherche	Irstea, Unité de Recherche RECOVER/Equipe G2DR - FRANCE	Examinateur
Jrad MOHAMAD	MCF	Université de Lorraine, France	Invité
Ali DAOUADJI	Professor	INSA Lyon, France	Directeur
El Mostafa DAYA	Professor	Université de Lorraine, France	Co-Directeur

LEM3 - 7 Rue Félix Savart, 57073 Metz
Université de Lorraine

UNIVERSITÉ
DE LORRAINE

École doctorale EMMA

THESIS

To obtain the title of:

DOCTOR OF THE UNIVERSITY OF LORRAINE

Specialty: geotechnical engineering

Presented by : Yuqi ZHANG

Mechanical behavior of granular material considering particle breakage

---

Thesis publicly defended on January 2018 in Metz in front of the jury composed of:

Pierre-Yves HICHER	Professor	Ecole Centrale de Nantes, France	Rapporteur
Belouettar SALIM	DR-HDR	Luxembourg Institute of Science and Technology, Luxembourg	Rapporteur
Marion MARTINY	Professor	Université de Lorraine, France	Examinateur
Christophe DANO	MCF	l'Université Grenoble Alpes UGA, France	Examinateur
Nadia BENAHMED	Chargé de Recherche	Irstea, Unité de Recherche RECOVER/Equipe G2DR - FRANCE	Examinateur
Jrad MOHAMAD	MCF	Université de Lorraine, France	Invité
Ali DAOUADJI	Professor	INSA Lyon, France	Directeur
El Mostafa DAYA	Professor	Université de Lorraine, France	Co-Directeur

LEM3 - 7 Rue Félix Savart, 57073 Metz
Université de Lorraine

Acknowledgments

When this part of a thesis is started, it indicates that my doctoral student stage is coming to the finish line. Thinking back the day in October 2014, I landed in CDG only with a new suitcase. Maybe one month later, the only partner who goes to CDG accompanied with me will be the old suitcase. Three years has passed like a white pony's shadow across a crevice. What's in exchange is a piece of paper proving this period, and memory of happiness and sorrow, friendliness and loneliness, luckiness and helplessness

I would like show my most sincere thankfulness to my supervisor, Prof. Ali DAOUADJI, an extraordinary and meticulous scientist. It is my honor to acquire his guidance and help. He is my guidepost on the road of science.

I am particularly grateful to my co-supervisor, Prof. El Mostafa DAYA for all the enthusiastic help and encourage during my doctoral career. I would like to express my appreciation to Jrad MOHAMAD for his help on my experimental and numerical works.

I also owe a special debt of gratitude to all the teachers such as BIAN Hanbing, Mahdia HATTAB, YIN Zhenyu, Guillaume BOBIN, MATHIEU Norman who offered advices during my study. I would like to thank the other colleagues in LEM3 who offer me assistance, Jacqueline DECKER, Nathalie KASPRZAK, Anne BLUM, Arlette JACQUIERRE, and Julien OURY.

I am indebted to all my friend, CHEN Cai, ZHAO Yajun, WEN Jing, ZHAO Dan, XU Shun, ZENG Ling, GAO Qianfeng, LIU Tao, HUANG Qun, HE Zhongming, XU rui, ZHOU Jialing, YANG Zhengtian, CHEN Xiaolei .... It is difficult to mention all your names here. It is you who shear tears and laughs with me and make this foreign town like home. It is about to leave and I don't know whether we can meet somewhere and sometime again. I will bless you.

I would like give my most special thanks to my parents. Without your infinite, selfless, unconditional support, it is too far today that can't walk really. Finally, thank you very much to my love, Dongxia. Without your sweet courage from China, I don't know whether I can insist on. Thank you for walking in my world.

To my family

To Dongxia

13-11-2017

Metz

Table of Contents

List of Figures

List of Tables

Introduction

A granular material is a collection of discrete, macroscopic particles with different morphology and mechanical properties. A basic characteristic of this material is that, there would be a loss of energy between two particles when they interact with each other [1]. Generalized concept of granular material contains solids, liquids and gases [2]. However, in this thesis, the studied granular material refers only to a collection of solid particles which are big and heavy enough to give their interaction forces dominance compared with the intermolecular forces. Therefore, liquids and gases are not studied in this thesis. Besides, solids ashes which are less cohesive and easily suspended in the gas due to its tiny sizes and light weights are not considered in this work.

Granular material is ubiquitous in numerous domains. Sugar, salt and cereal are used in the food processing industry. Besides, the operation of powders is also common in manufacturing medical drugs in the pharmaceutical industry. Sand, soil and rock are the objects of study in construction engineering or roads and bridges engineering field, such as excavating foundation and laying roadbed. Obviously, the mechanical behaviour of granular material is different from other continues material, which may make a huge impact on our daily life. For example, the Canoas Novos Dam of Brazil was regarded as the third highest dam of concrete rock fill dam in the world and cost 6671 million dollar. While in 2006, water ran out following a break in the dam wall. One of the key reasons was that a lot of particles of the soil below the bottom of the dam crushed which caused strength reduction of the foundation [3].

So far, several researchers have investigated the complex behavior of granular material. Three different scales including macroscopic, mesoscopic and microscopic can be used to study this kind of material. Till now, soil mechanics could be a set of theories about granular material which are mature enough to be applied to solve practical engineering problems [4]. The three basic assumptions of soil mechanics are continuity, homogeneity and isotropic [5]. Therefore, this theory is still available on macro and mesoscopic scales such as Mohr-Coulomb elastic-ideally plastic model, hypoplastic or elastoplastic models and so on. All the models above consider granular material as a continuous and homogenous media containing an infinite but sufficient number of unbreakable and inseparable particles, leading to a poor understanding of particle-scale mechanics [6].

In fact, the property of granular materials also depends on the particle scale which is smaller than the macroscopic scale, but larger than the atomic dimension. The behavior of granular material is strongly affected by the mechanical behavior of single particles and the relative arrangement of voids and particles. In 1727, Stephen Hales [7] started the study of geometrical arrangements of a set of objects packing randomly. He also used the dimple patterns on peas that had been expanded in a closed, water-filled container. However, Hales' work did not emphasize the mechanical behavior but was limited to the sap of vegetables. The first study of packing of granular material from the perspective of the mechanics began in 1929 by Furnas [8]. In addition, the single particle strength which is a basic property influencing the behavior of granular material was primarily studied by Jaeger in 1967 [9]. Since then, scientists have examined mechanical behavior of individual particle through using several methods. Regarding the mechanical behavior of multiple particles, scientists found that under high effective stress, crushing of particles may occur and act as a significant factor which influences the physical and mechanical behavior of granular material. [10] [11] [12] and [13].

In the present study, experiments and simulations have been performed to investigate the mechanical behavior of granular material at a particle scale with the consideration of particles breakages and particles arrangements. Specifically, nearly spherical particles made by expanded clay would be the experimental samples. Through experimental and numerical methods, the mechanical behavior of single particle considering particle breakage when influenced by pressure would be studied. The fabric characteristic of a packing of spherical particles would be studied with an experimental method and analyzed by software written with MATLAB code. The mechanical and kinematical behavior of multiple particles when suffering biaxial load would be investigated.

In the first chapter, the research background and present conditions in the fields involved in the thesis were reviewed. The basic theories employed in the later chapters would be presented.

In the second chapter, uniaxial compression tests would be performed on approximately spherical single particles. μ-CT technology would be applied to build the geometry of the particle. The geometry would be meshed and imported into Abaqus for further simulation. Comparisons and analyzes would be made about the results of the laboratory tests and simulations.

In the third chapter, biaxial tests would be performed on several groups of particles which were set in a Plane Strain Chamber composed by PMMA. Photos were taken to record the tests. Software was compiled with Matlab code to analyze the fabric of the packing of granular material when undertaking biaxial load.

In the forth chapter, biaxial tests would be performed on several groups of particles with different test setting. Photos were taken during the process of the tests. Mechanical behavior was observed from the tests. Software compiled with Matlab code was used to trace the displacement of each particle in each test in order to investigate the kinematical characteristic of multiple particles when under biaxial loading.

In the fifth chapter, a conclusion would be made of the whole thesis and a prospective would be described.

Chapter I. Literature Review

I.1.Introduction

This chapter introduces the research background and present conditions in the fields involved in the thesis. The basic theories employed in the later chapters will be also presented. In the second part of this chapter, failure behavior of single particle when with compression tests conditions would be reviewed. The research achievements of other scholars about fabric of packing of granular material are presented in the third part. In the fourth part, the mechanical behavior of multiple particles considering particles failure would be reviewed.

I.2.Failure behavior of single particle under compression

The failure of particles plays a crucial role in the properties of the assembly. It could affect the particle size distribution [14], the shear strength [15], [16] and [17], the solid fraction [18], the yielding surface [19], and so on. Consequently, it is thought that controlling the crush would improve the mechanical performance and reduce the instability. To investigate the global behavior of granular material influenced by particle crush, some scientists performed some investigations on the failure behavior of single particle. In general, the objects are mainly on process mechanical characteristic during loading. In this part, a review will be made on the numerous work achievement and research methods.

I.2.1.Experimental studies on single particle failure behavior

a.One dimensional compression tests

For one dimensional compression tests, the yield stress of calcareous sands is lower than that of siliceous sands, because the calcareous particles are more friable [20]. Particle breakage was found to be the principal source of plastic volumetric compression on the normal compression line by McDowell et al [21] who related the micromechanics of grain fracture to the macroscopic deformation of crushable aggregates. As early as in 1948 and 1958, Terzaghi et al [22] and Roberts et al [23] performed one dimensional compression tests. In One dimensional compression test, vertical load is applied while lateral restraints are applied on a sample, so the sample could have only vertical compression and without lateral deformation. The yield stress of one–dimensional compression is an important parameter which indicates the initiation of particle crushing. The value of yield stress is always defined at the point where the relation of the deformation to the stress increment changes rapidly on a plot of semi-logarithmic coordinates. With the same kind of tests to aggregates, McDowell et al [21] indicated that the yield stress and the particle tensile strength exists a directly proportional relationship. With the same test principle, Yoshimoto et al [24] performed tests on granulated coal ash to evaluate the crushing behavior of each single particle. Besides, he demonstrated that, when the crushing strength rises, the shear stiffness increased and the compressive volumetric strain decreased. In addition, he also found the crushing strength of single particle shows no relationship with its dimension.

b.Brazilian test

A kind of widely used tests for rock mechanical applications, Brazilian tests, which could be treated as a 2D displacement-controlled single particle compression tests. The Brazilian test is a simple indirect testing method to obtain the tensile strength of brittle material such as concrete, rock, and rock-like materials, in which, a cylinder is diametrically compressed to failure [25]. Four typical loading configurations are shown in Fig I-1 [26].

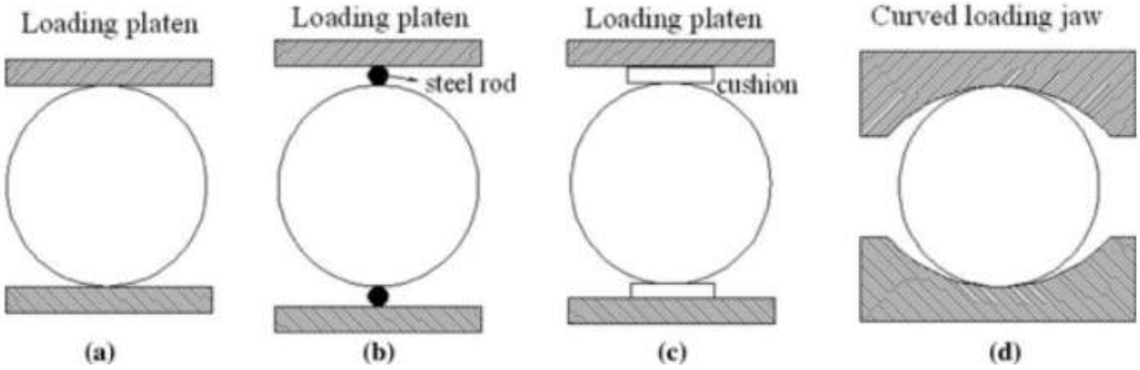

Fig I-1 Four types of Brazilian tests loading configurations in Li's work [26]

(a) Flat loading platens, (b) Flat loading platens with two steel rods, (c) Flat loading platens with cushion, and (d) Curved loading jaws

Carneiro et al [27] invent the Brazilian testing method to obtain the tensile strength of concrete in 1943. Mellor et al [28] measured tensile strength by Brazilian tests on discs and annuli for Griffith-type materials. In addition, he also designed a curved-jaw loading jig to reduce the stress concentration at the loading points and concluded that the Brazilian test could successfully give a good measure of uniaxial tensile strength. Newman et al [29] carried out statistical experimental studies on the effect of specimen geometry and stress rate on the determination of the tensile strength of sandstone by the Brazilian tests in 1990 and concluded that the length-to-diameter ratio of the specimen exerts a significant effect on the tensile strength.

Salami et al [33] performed several multipoint crushing tests on cylindrical samples to investigate the affect of coordination number on particle crushing (Fig I-2). His tests demonstrated that the amount of orientations of contacts plate could influence the fragmentation of a single particle and the critical force was highly dependent on the contact area.

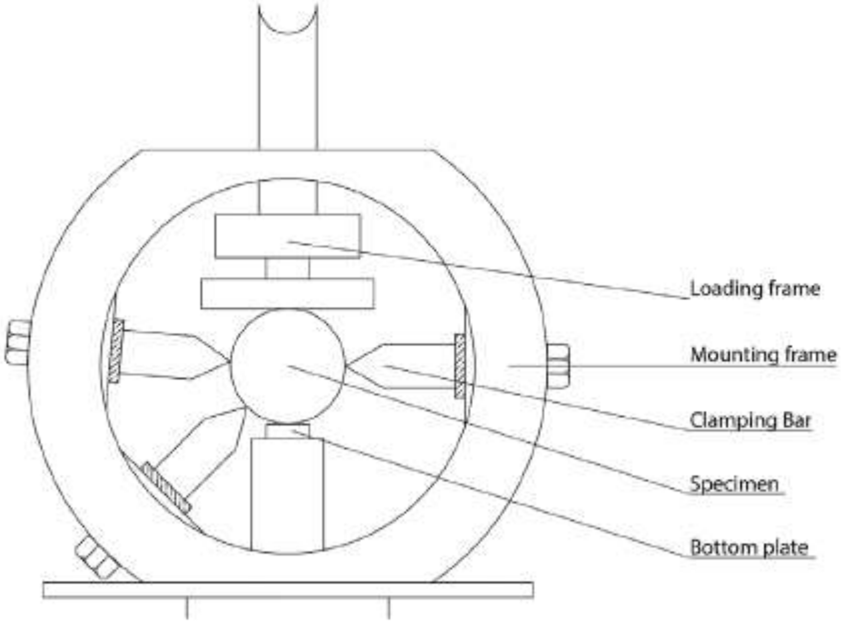

Fig I-2 Sketch of testing apparatus of Salami's work [33]

c.3D single particle compression tests

As for 3D displacement–controlled single particle compression tests, singles particles are applied displacement controlled loads from one or several directions. McDowell [30] performed tests on 30 silica sand grains of different diameters and found that the yield stress of a particle increased with the increase of tensile strength and the decrease of particle size. Nakata et al [31] conducted single particle crushing tests to investigate the relationship between single particle crushing characteristics and one-dimensional compression behavior. According to the results, the particle characteristic stress grows when the void ratio increases or the coordination number decreases. Cavarretta et al [32] carried out compression tests on glass ballotini which were used to simulate soil and concluded that the initial plastic displacement has relationship with its topography and bulk character and the surface rigidity. Moreover, he also designed a new particle-particle friction apparatus (Fig I-3) to study the influence of particle roughness. His tests indicated that the plastic strain appeared at the contact surface and related to plastic yield.

In addition to particle strength, some scientists also found the coordination number could act as another factor which influences particle crushing. It can be concluded that larger particles with a higher coordination number due to their sizes are difficult to crush. By contrast, the smaller ones which have a higher probability of having a low coordination are easier to crush [14].

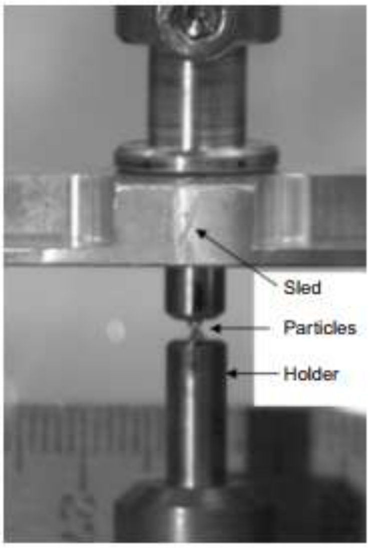

Fig I-3 The inter-particle friction apparatus designed by Cavarretta et al [32]

I.2.2.Numerical simulation on single particle crushing behavior

a.FEM methods

As a progress of computer and algorithm, scientists started to combine numerical simulation with laboratory experiments. Tang et al [34] simulated 2D disk samples and 2D irregularly shaped particles under diametric loading with RFPA^{2D} which is a finite element method (FEM) software used to study their crushing behavior following different loading conditions (Fig I-4). In this software, Weibull's distribution law is used with a homogeneous index *m* to describe the heterogeneous mechanical properties of the model elements. Breaking an element means reducing the element's stiffness and strength, but the broken elements may restore their stiffness when they are highly compressed. He has concluded that the failure mode during loading is suddenly splitting and gradually crushing. In addition, he also found that the confinement stress increases the sample's initial stiffness and breaking strength. Loading with lateral constraint produces finer sub-particles because of shear failure especially in the vicinal zone of the contact points. However, loading without lateral constraint could lead to an increasing number of coarse sub-particles because of splitting parallel to loading diameter.

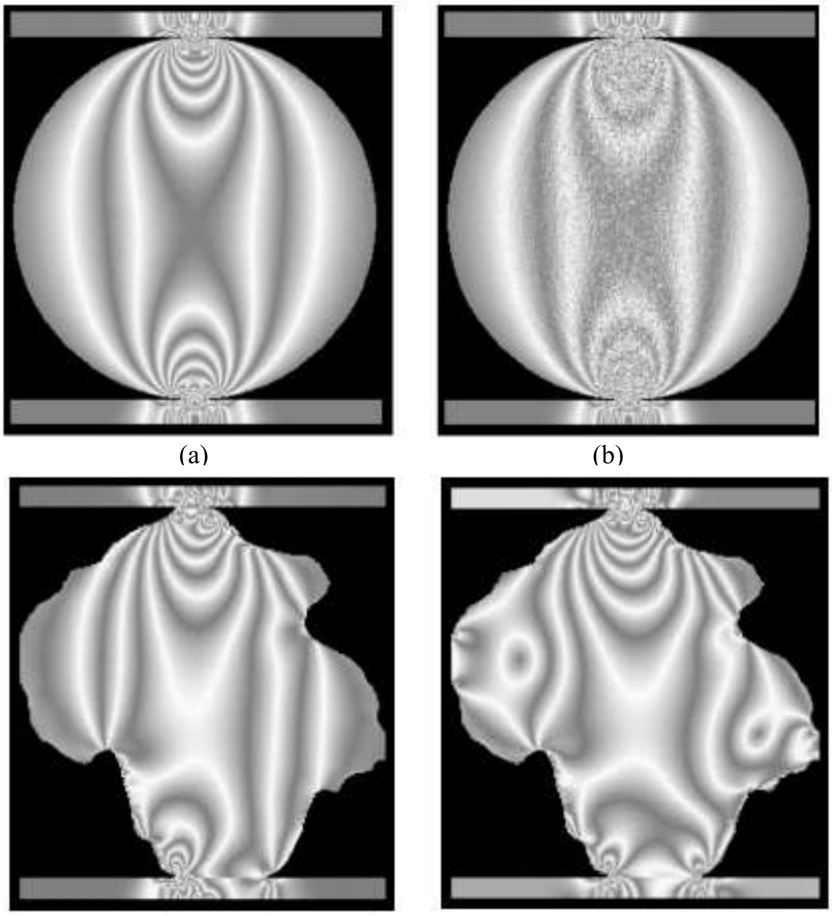

(a) (b)

(c) (d)

Fig I-4 The fringe contours of samples of different condition under diametral loading of Tang's work : (a) homogeneous disk, (b) heterogeneous disc, (c) irregular shape particle without confinement, (d) irregular shape particle with confinement [34]

b.DEM methods

For FEM, the continuum assumptions permit the elements to undergo only small strains. Therefore, even when fracturing is allowed, large-scale opening, sliding, or complete detachment of elements is not possible. Compared with FEM, discrete element method (DEM) is more extensively used for modelling crushing of particles with an advantage of providing a microscopic insight of the progressive failure phenomena and breakage mechanism. The difference of the two methods is that for FEM, a particle acts as a whole and is separated to several elements while calculating. However, for DEM, a particle breakage is modelled by an agglomerate of bonded spheres [35] or replaced by a group of fragments based on suitable failure criteria [36]. In the sphere bonding models, there are two specific implementations, namely, parallel bond and contact bond. In the parallel bond, a bond disk is defined between the two bonded spheres to transfer normal force, shear force and bending moment of oppose rolling. The contact bond model does not have the bond disk as defined in the parallel bond model, and can only resist normal and shear forces at the contact point (Fig I-5).

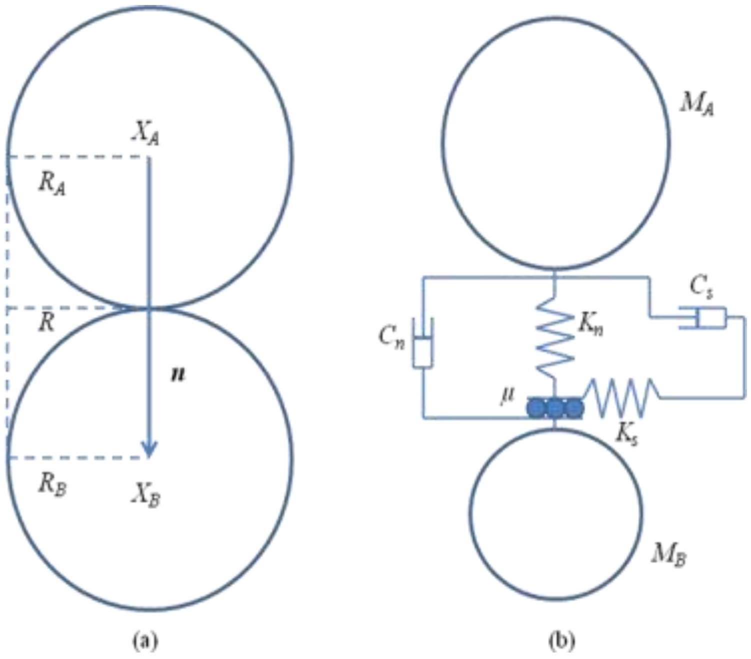

Fig I-5 Interaction between two spheres: (a) Parallel bond model; (b) Contact bond model

The corresponding parallel bond is shown in Fig I-5 (a) where X_A and X_B are the position vectors of sphere *A* and sphere *B*, $\boldsymbol{n}$ is the contact normal vector. As a result of the constant normal and shear stiffness of the bond, a force and a moment are developed within the bond induced by the relative motion at the contact. For the contact point interaction between spheres, the linear visco-elastic model is adopted, as shown in Fig I-5 (b) where M_A and M_B are the mass of sphere *A* and *B*, K_n and K_s are the normal and tangential stiffness, C_n and C_s are the normal and tangential damping coefficient, μ is the friction coefficient.

Cil et al [38] and Yan et al [39] modelled fracture of irregularly shaped particles which were generated as an agglomerate of large numbers of spherical sub-particles connected by contact bonds with moment and tension through using Particle Flow Code 3D (PFC3D) and Sphere-base Discrete Element Method (SDEM), respectively. According to their studies, cracks appeared with a few bond breakages at the contact point. Then, more bonds breakages appeared and the contact forces increase. Finally, the particle was divided into several smaller parts with a dramatic decrease of contact forces and increase number of broken bonds. In Cil's work, the investigation demonstrated that particle crushing is affected by boundary conditions. Additionally, the micro behavior of agglomerates caused by particle crushing could not regenerate a stress-strain behavior at large scale. In Yan's work, four stages of a particle crushing linear elastic (O-A), crack initiation (A-C), softening(C-D) and final splitting (E-G) was described with a view on the bond according to the stress-strain relationship. In the crack initiation stage, a few bonds broke. In the soften stage, more bonds broke and the stress declined rapidly. In the final splitting stage, particle split into several sub-particles with a drastic increase of bonds breakages (Fig I-6). Sukumaran et al [40] conducted DEM simulation with PFC to explore the influence of coordination number to the crushing strength of particles. She concluded that, for 2D particles (disks), the critical force F_c follows

$$F_c = d^2 \sigma_c f_D f_{CN} \tag{I-1}$$

where σ_c is the critical tensile stress. f_{CN} describes the effect of coordination umber

$$f_{CN} = (C-1)exp\,(\frac{D}{d})\frac{(c-2)(c-3)}{4c} \tag{I-2}$$

where C is the coordination number, d is the diameter of the crushed particle and D is the diameter of the surrounding particles.

f_D describes the effect of diameter of surrounding particles

$$f_D = \frac{({}^{D}/_{d})}{\left({}^{D}/_{d}\right)+1} \tag{I-3}$$

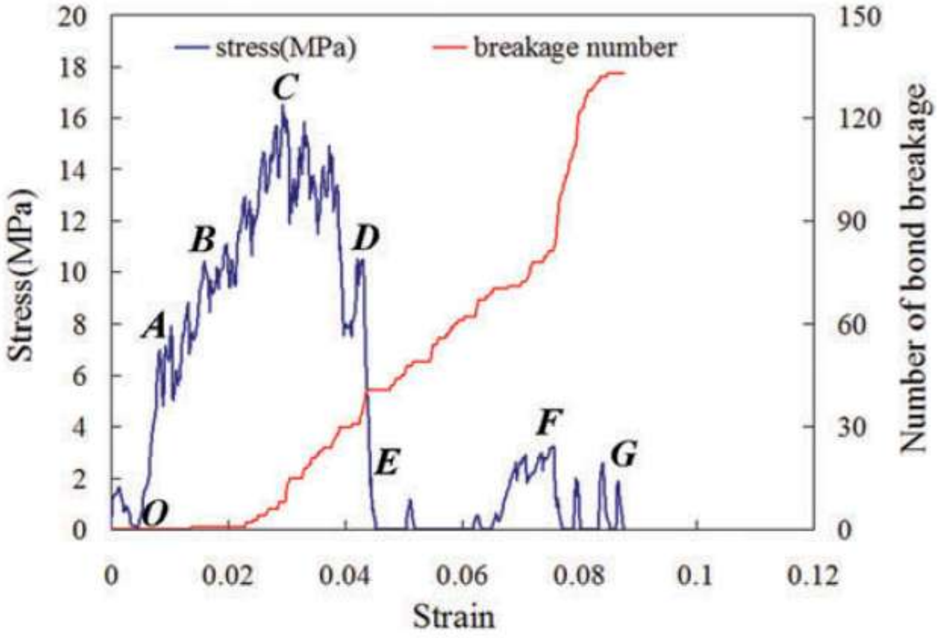

Fig I-6 Stress-strain curve and number of bond breakage of Yan's work [39]

c.A combination of FEM and DEM

Since deformability can be well described by FEM, and fractures can be explicitly represented by DEM, to combine the advantages of FEM and DEM, several studies used a merging of the two methods. For example, Bagherzadeh et al [41] and Ma et al [42] used a combined finite-discrete element method (FDEM). In this system, each particle is modelled with FEM mesh, while all the relationship between particles such as contacts, displacement, inter-particle force, are calculated with DEM (Fig I-7). When a contact is detected by the software, a linear contact model will be generated to calculate contact force. The numerical results indicated that higher confining pressures gave rise to a larger numbers of particles breakage. Additionally, the particles in the shear band were more likely to break.

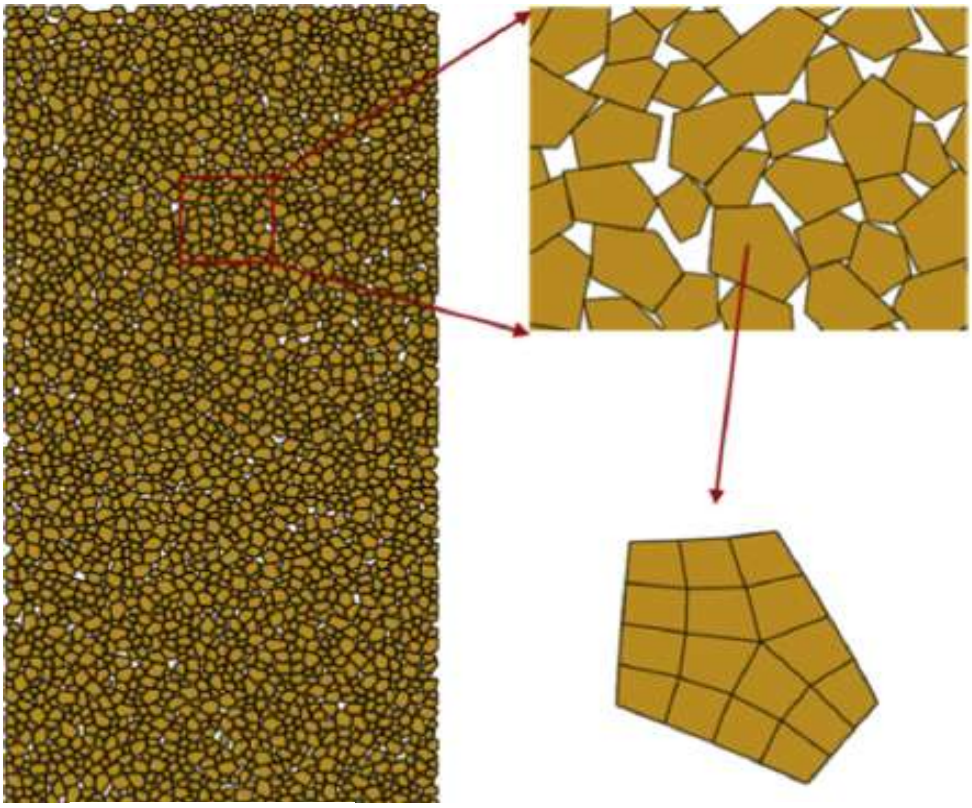

Particle assemblies Finite element mesh

Fig I-7 Particle assembly simulated by FDEM in Ma's work [42]

Mahabadi et al [43] believed that precious FDEM codes had some shortcomings. For example, there was no appropriate friction law to describe quasi-static friction and in the fracture model, there is no friction component. To overcome such limitations, a new numerical code Y-GEO is developed based on FDEM framework mainly for rock mechanics. A micro-scale model of a heterogeneous Brazilian disc test was studied to prove Y-Geo could be capable of accurately estimating crack trajectories and the failure mechanism of the specimen (Fig I-8).

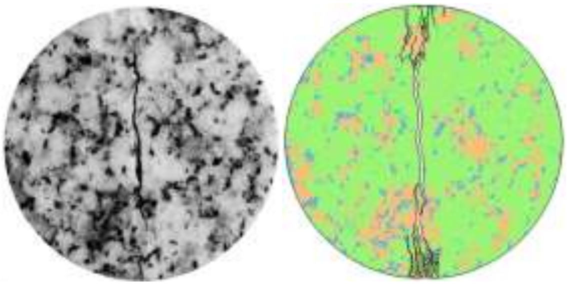

(a) (b)

Fig I-8 Fracture pattern of the Brazilian disc of Mahabadi's work : (a) sample failed in the laboratory; (b) simulation result

Similarly, more methods on the basis of the same fundamental principals have been applied by other scientists. Each of them made some improvement on the FDEM methods. For example, Multiple-particle finite element method (MPFEM) combines discrete behavior of particles assemblies with the analysis ability of large contact deformation. The advantage is there is no simplifying assumption for the particle kinematics and contact mechanics like DEM. Move over, this method could simulate compression to high relative densities [44]. Meshed discrete element method (MDEM) was developed to overcome the limitation on basic DEM that the existing contact laws could not analysis all physical phenomena of granular material. It could give an accurate description of the particles' deformation and produce more accurate results [45].

I.2.3.The exploration of the inside structure of a particle

a.Computed Tomography technology

Admittedly, all the traditional laboratory experiments are based on the particle's external morphologies and obtain its external displacement and strain. Even for numerical simulation, especially for the some kinds of particles whose internal structure is complicated enough to influence its mechanical behavior, the internal structure whose parameters are confirmed based on the traditional laboratory experiments results could not reflect the internal microstructure behavior during the crushing process. To investigate the internal geometry, X-ray Computed tomography (CT) technology could provide an effective instrument. X-Ray CT is a non-destructive, 3D high resolution imaging method that allows the internal microstructure of a particle to be understood. This technology was invented for medical domain and was started to be utilized for geotechnical engineering field in about recent 30 years. A CT scan utilizes lots of X-ray projections taken from different perspectives to produce enough cross-sectional images of a sample, in order to reconstruct its inner appearance [46]. X-Ray Computed Tomography Scan was first successfully utilized in geotechnical field research in 1996 by J. Desrues et al [47]. He studied strain localization in triaxial tests on sand and the shear band could be shown in his research (Fig I-9). Recently, with a progress of the instrument manufacturing, scientist performed more CT tests and some improved version of CT tests with smaller resolutions.

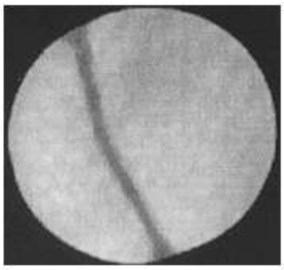

Fig I-9 A shear band of a sand from Dersures' work [47]

Zhao et al [48] performed CT scan four Leighton Buzzard sand (LBS) particles and four highly decomposed granite (HDG) particles during loading to study the mechanism of particle breakage behavior when under single particle compression (Fig I-10). He demonstrated that particle morphology and initial microstructure significantly influence the fracture pattern. The complicated morphology and microstructure could result in a complicated fraction pattern. For the LBS particles, the fracture planes were mainly parallel to the loading direction. For HDG particles whose external morphologies and internal microstructures are more complex, the initial internal voids, impurities resulted in the generation of different forms of tensile, shear and bending cracks through cleavage planes, mineral boundaries, voids or impurities. Although the LBS particles had much larger sphericity and convexity values than the HDG particles, fracture caused their values to decrease and converge to the same level. In contrast, while the initial aspect ratios were similar, the final values were lower for LBS particles. The stronger LBS particles tended to produce lower aspect ratio fragments with lower angularity, but resulted in the same level of sphericity and convexity as the HDG fragments.

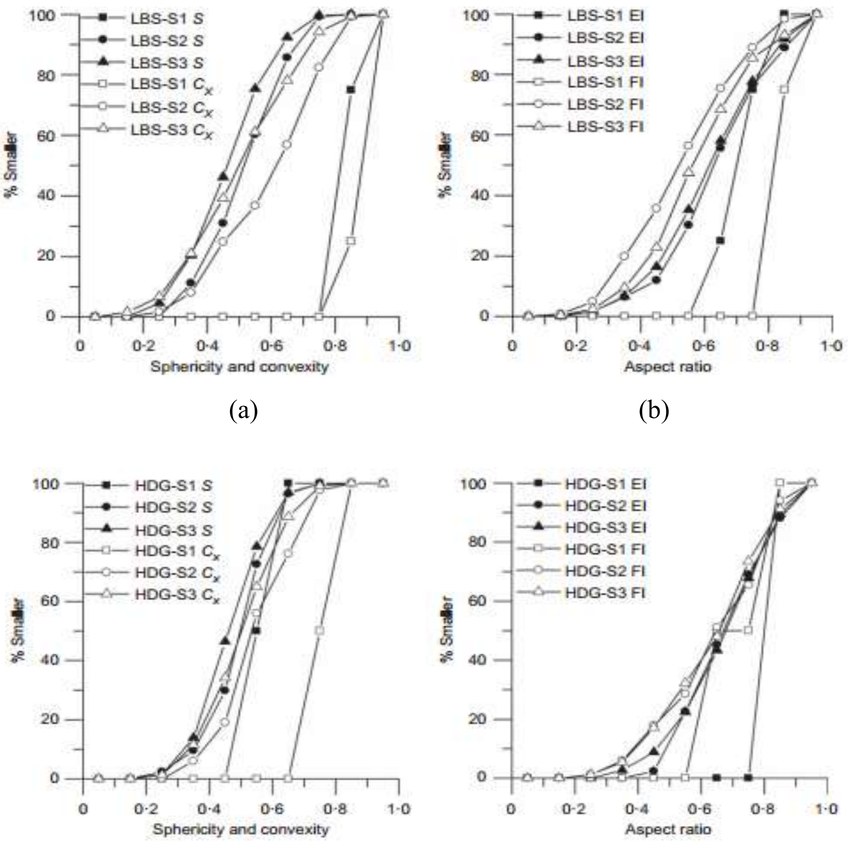

(a) (b)

(c) (d)

Fig I-10 Evolution of the shape parameters for the LBS and HDG particles in Zhao's work [48]

(a) sphericity and convexity of LBS; (b) aspect ratio of LBS ;(c) sphericity and convexity of LBS; (d) aspect ratio of LBS (*S*: sphericity; C_X: convexity; EI: elongation index; FI: flatness index)

b.Some enhanced instruments

Based on fundamental CT technology, some other enhanced instruments were developed and utilised. At first, the accuracy was improved dramatically. One of the most popular equipment is currently Micro CT or μ-CT whose higher resolution could ensure the precision of the results. The word *micro* is used to indicate that the pixel sizes of the cross-sections are in the micron range. In addition, some scientists also call it High-resolution CT (HRCT) [49].

Druckrey et al [50] used Synchrotron Micro-computed Tomography (SMT) which could be regarded as an enhanced instrument to industrial CT system by producing images with a higher resolution (in the order of 5 micron/voxel) to capture and reconstruct the geometry of single silica sand particle. For soft X-ray, its stronger attenuation might lead to beam hardening effects in the reconstructed images. Synchrotron radiation could solve this problem through providing an intense hard X-ray with high photon flux which could make it possible to acquire reconstructed images with high resolution and low noise ratio (Fig I-11). He found that cracks appeared from the contact point between the particle and the loading system and since the failure started, the elastic stress decreased rapidly and a brittle failure appeared and separate the particle to several parts.

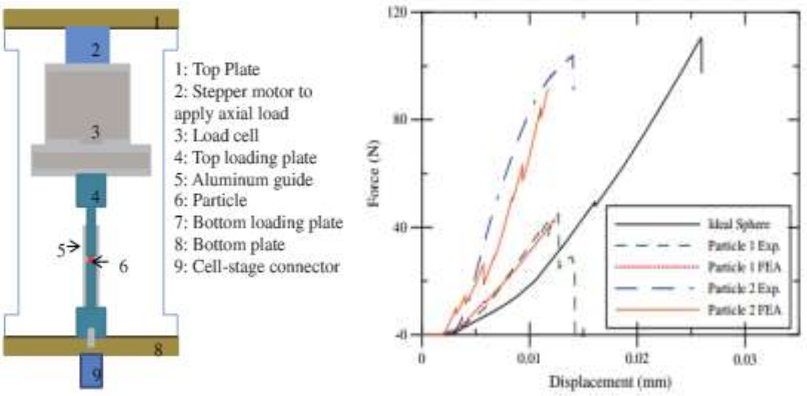

(a) (b)

Fig I-11 Sketch and results of test of Druckrey's work [50] : (a) Sketch of the SMT tests; (b) Load-displacement relationships from experiments (Exp) and FE analyze (FEA) for ideal sphere and the two real particles

Alshibli et al [51] considered that, although CT scan could provide the inner geometry including voids of a sample, it cannot measure the contact stress and strain. In contrast, three-dimensional X-ray diffraction (3DXRD) microscopy is a promising technique that has the potential to measure lattice strains and crystallographic orientation of crystalline materials. Consequently, he tried to use 3DXRD method to determine volume averaged lattice strain tensor components of individual silica sand particles under axial loading condition (Fig I-12). His work demonstrated that 3DXRD technique could collect diffraction data which could be utilized to calculate particle lattice strain. Besides, he also found that before particle crushing, the vertical force and vertical normal strain fit a linear elastic relationship (Fig I-13).

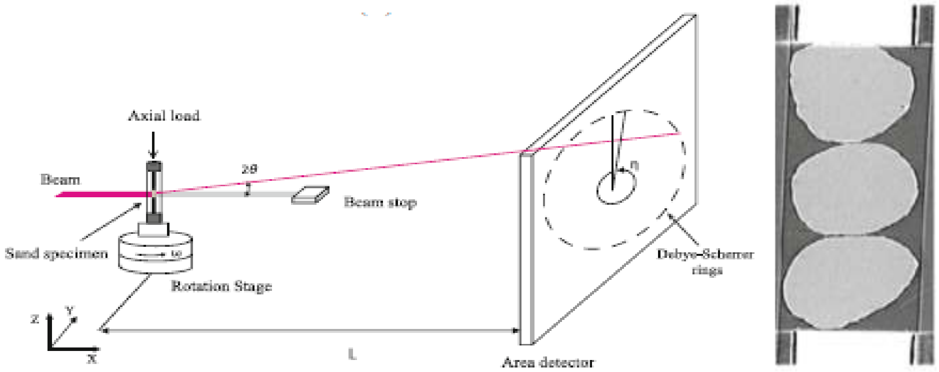

(a) (b)

Fig I-12 Test methedology of Alshibli's work [51] (a) Far field of 3DXRD measurement geometry and (b) particles setting

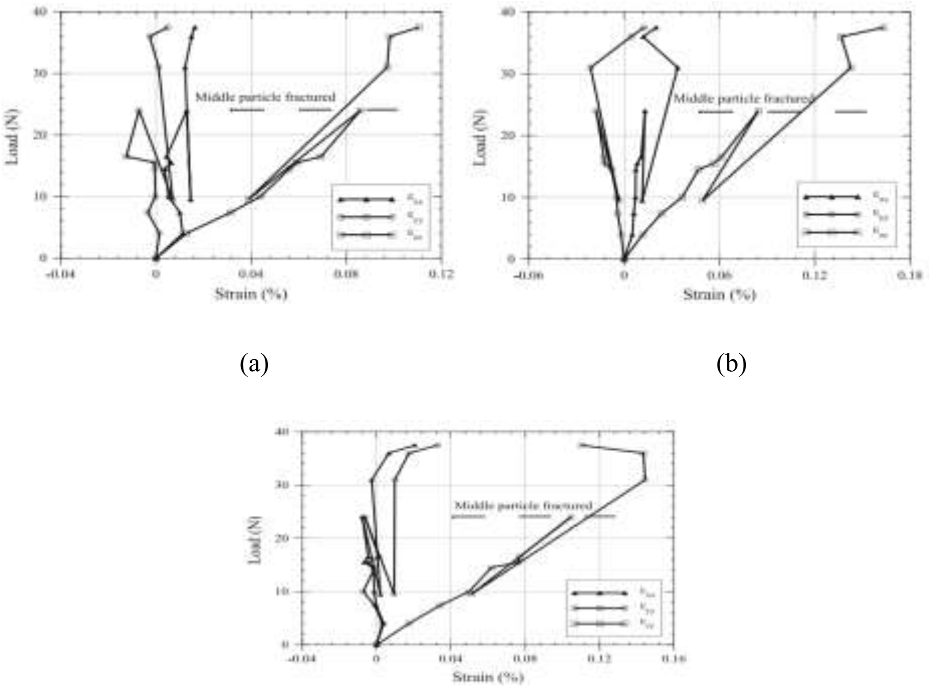

(a) (b)

(c)

Fig I-13 Evolution of lattice strain measurements as a function of axial load for Test 3 for (a) top particle, (b) middle particle, and (c) bottom particle

I.3.Fabric of packing of granular material

Particulate systems play an important role in the world we live in. Numerous scientists tried to make some breakthrough on this field. A packed bed is the most fundamental research topic of granular material due to all particles. The definition of *fabric* is the arrangement of particles, particle groups, voids and their correlation [14]. Different initial fabric could cause a lot of considerable differences on the mechanical behavior of one kind of granular material [53] [54]. Early studies established on mathematical derivation and laboratory experiments such as Oda's work [55] and Finney's work [68]. Recently, with the development of computer technology and image processing, more investigations have been applied in this field.

I.3.1.Basic quantities of fabric of granular material

Based on experimental observation of Oda et al [55], fabric of a random assembly of spherical granular were introduced such as density of contacts, average branch length and second-order symmetric tensor. Coordination number, radial distribution function and packing density are the most commonly used and fundamental parameters to characterize a structure of a granular material [56] [57].

At the particle scale, the granular fabric involves three basic vectors based on which other local geometrical variables could be defined. For a pair of particles contacting particles 1α and 2α sharing the contact α, a) the branch vector $\vec{l}$ joins the centres of particles, b) the contact orientation vector $\vec{n}$ defined as the unit vector normal to the particle boundary at the contact point α and c) the contact vectors $\vec{c}$ joins the particle centres to the contact point. The contact force $\vec{f}$ indicated the force at the contacting point.

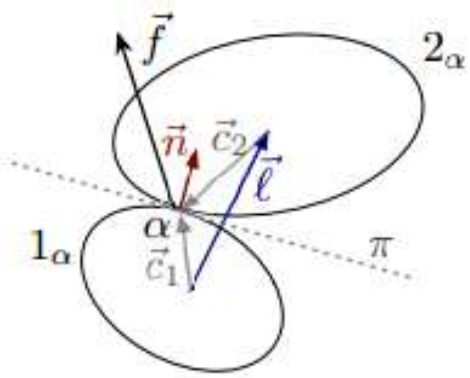

Fig I-14 Local vectors at the contact α between two particles 1α and 2α:

I.3.2.Particle connectivity

The connectivity of a granular assembly refers to the set of active contacts. The connectivity is described most basically by the *coordination number* which appeared as a concept in chemistry field and originally defined in 1893 by Alfred Werner et al [58]. The coordination number of a central atom in a molecule or crystal is the number of its near neighbours. For granular material, the coordination number has two meanings for two kinds of study object. For one particle, the coordination number indicates the number of its neighbour particles [59]. For a random arrangement of particles, the coordination number means the average number of particles touching a given one. Besides, the detailed calculating methods of the coordination number were introduced by Jouannot-Chesney et al [60]. The packing density means the volume fraction of the space dominated by particles. Obviously, for a certain material, the packing density plus the porosity equals to 1. Lochmann et al [61] studied the geometrical organization of four different kinds of packing structures including monosized, binary, power-low and Gausian sized distribution. The results demonstrated that the fabric of granular material is closely associated with radial distribution function.

Considering a finite population of particles, N_p corresponds to the number of particles. For particle number i, it may contact with another particle number j. Each of the contact is given a name $c_{i\text{-}j}$. N_c corresponds to the total number of contacts.

$$N_c = \sum c_{i-j} \qquad \text{I-4}$$

N_{co} means the coordination number of the material.

$$N_{co} = \frac{N_c}{N_p} \qquad \text{I-5}$$

It is worthwhile of noting that, associated with one contact surface, there are two contacts and each of the contact belongs to a particle at one side. Therefore, $c_{i\text{-}j}$ and $c_{j\text{-}i}$ refer to two contacts of two opposite direction of one contact surface.

If δ is the density of particles centre located in a chamber whose volume is V.

$$N_p = V\delta \qquad \text{I-6}$$

If the radial distribution function could be given by a probability density function $f(r)$

$$\int_{r_{min}}^{r_{max}} f(r)dr = 1 \qquad \text{I-7}$$

For any function (r) , $\bar{\Phi}$ is the mean value based on the probability density function

$$\bar{\Phi} = \int_{r_{min}}^{r_{max}} \Phi(r)f(r)dr \qquad \text{I-8}$$

Let V_s be the total solid volume and e be the void ratio, the total volume V equals to $(1+e)V_s$. Therefore

$$V_s = \int_{r_{min}}^{r_{max}} \frac{4}{3}\pi r^3 N_p f(r)dr = \frac{4}{3}\pi N_p \overline{r^3} \qquad \text{I-9}$$

$$\delta = \frac{N_p}{V} = \frac{3}{4\pi(1+e)\overline{r^3}} \qquad \text{I-10}$$

the density of contacts is

$$N = \frac{N_c}{2V} = \frac{N_{co}\delta}{2} = \frac{3N_{co}}{8\pi(1+e)\overline{r^3}} \qquad \text{I-11}$$

Some scientists studied the relation between the contact coordination number and the void ratio of the material. Oda [62] found that the N_{co} and e are independent of the radial distribution function (Fig I-15). The relationship is shown as follow:

$$N_{co} = G(e) \qquad \text{I-12}$$

Thus, the density of contacts

$$N = \frac{3G(e)}{8\pi(1+e)\overline{r^3}} \qquad \text{I-13}$$

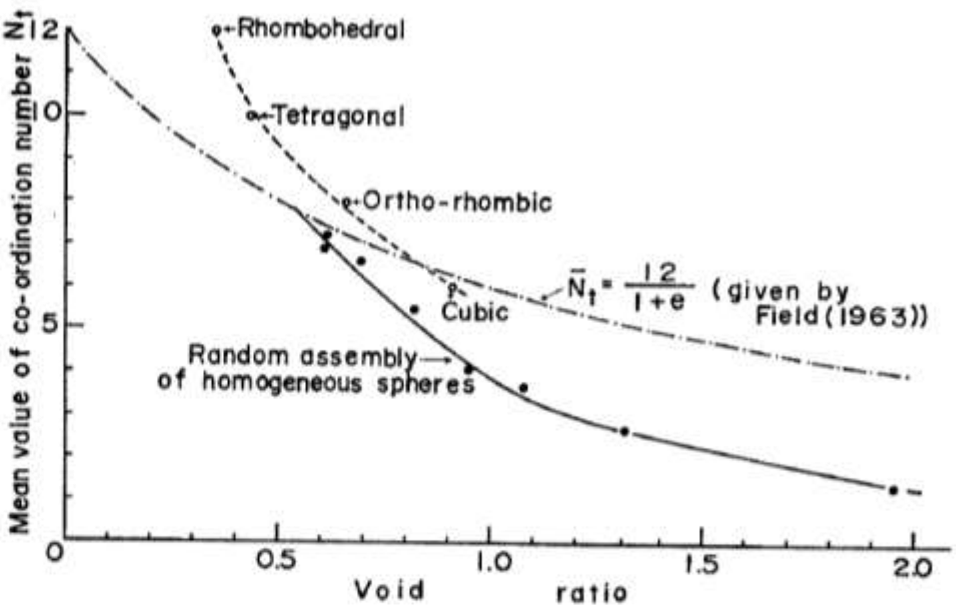

Fig I-15 The relationship between void ratio and coordination number of Oda's work [62]

The concept of *coordination number* has a limitation that all the particles contact each other at single points or the contacting areas which could be simplified to points. Therefore, this kind of contact has a limitation on the particles shapes. For example, for the cuboid or sheet particles, the contact surface cannot be points. Therefore, a definition *contact index* was proposed by Fonseca which considers the contact area.

$$I_c = \left({}^{1}\!/_{N_p}\right)\left(\sum_{i=1}^{N_p} {}^{1}\!/_{Sp_i}\right)\left(\sum_{j=i}^{N_{c,i}} Sc_j\right) \qquad \text{I-14}$$

where Sp_i is the surface area of particle *i*, Sc_j is the surface area of the contact *j* and $N_{c;i}$ is the number of contacts involving particle *i* [63].

The contact normal which is also called contact orientation vector is defined as the unit vector normal to the contact boundary. Besides, the vector joining the centres of contacting particles is called the branch vector. The vector connecting the centre of a given particle and its nearest neighbours is called doublet vector (Fig I-16) [64].

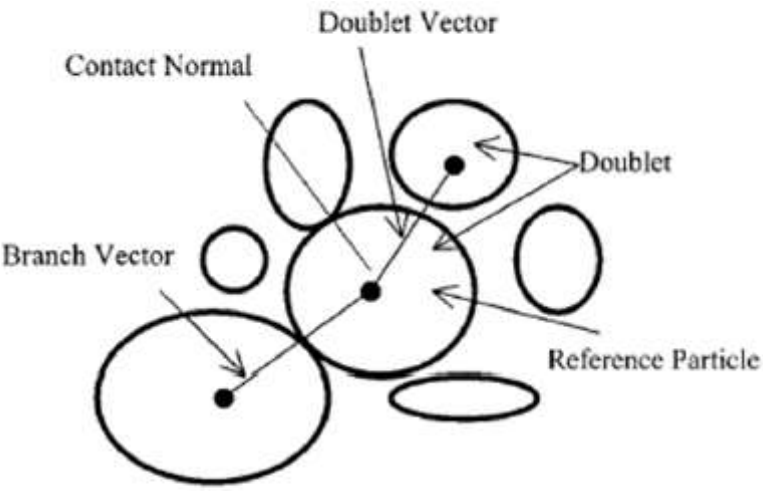

Fig I-16 Illustration of contact normal, branch vectors and doublet vectors from Wang's work [64]

To express vectors of a given set of particles, the most Intuitive approach is to build rose diagrams (Fig I-17) [65][67].

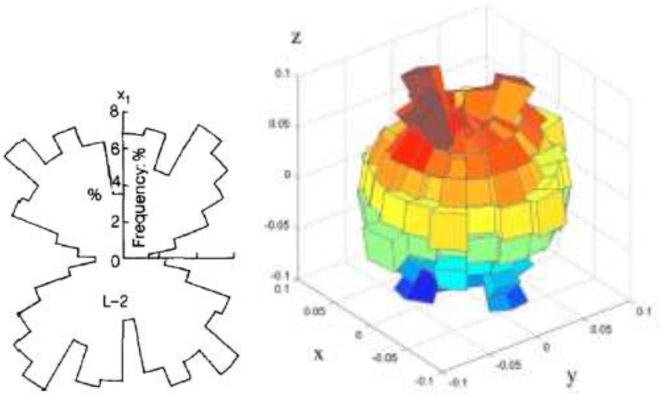

(a) (b)

Fig I-17 Distribution of the contact normals

(a) 2D example from Oda's work [65] (b) 3D example from Wang's work [67]

These rose diagrams could offer a qualitative description of fabric orientations, and the likelihood of the orientation could be described by a probability function.

$$\int_{\Omega} P(\vec{n})d\Omega=1 \tag{I-15}$$

where $d\Omega$ is the differential solid angle in a spherical coordinate system and $\vec{n}$ is the vectors of contact normal.

I.3.3.Contact anisotropy

The shear strength of dry granular materials is generally affected by the buildup of an anisotropic texture due to friction between the particles and as a result of arrangement effects depending on particle shapes and sizes [65] [66].

From the experimental values, an experimental probability density function $P_{exp}(\vec{n})$ which can be approximated by a theoretical distribution$P(\vec{n})$) could be defined. The theoretical approximation could be obtained by means of the least square method which amounts to minimizing the function

$$E = \int_{\Omega} (P(\vec{n}) - P_{exp}(\vec{n}))^2 d\Omega \qquad \text{I-16}$$

Let P be expanded as a polynomial sum

$$P(\vec{n}) = C_0 + C_{ij} n_i n_j + C_{ijkl} n_i n_j n_k n_l + \mathrm{h.o.t} \qquad \text{I-17}$$

Because of the even parity of P, all the odd terms are dropped. The function P is parameterized by the tensors C_{ij}... of increasing order. It can be shown that for an approximation of order m, all terms of order below m should be omitted since they can be expressed through the higher-order terms. For example, using the identity tensor I, we can write $C_{ij}n_i n_j=(C_{ij}I_{kl})n_i n_j n_k n_l$, since $I_{kl}n_k n_l=1$. Hence, the most general polynomial expression of order m is simply given by

$$P(\vec{n}) = C_{i_1 i_2 \dots i_m} n_{i_1} n_{i_2} \dots n_{i_m} \qquad \text{I-18}$$

For 2D system, Radjai et al [65] introduced the concept of anisotropy and studied the method for description of granular texture with anisotropy. A representation of the probability density function of the contact normal distribution is produced as a Fourier expansion and the second order expansion of P could be expressed as

$$P(\vec{n}) = \frac{1}{2\pi}[1 + a\cos 2(\theta - \theta_c)] \qquad \text{I-19}$$

where α is the second order fabric anisotropy, θ is orientation of $\vec{n}(\cos\theta, \sin\theta)$ θ_c defines the direction of the fabric anisotropy.

The second order fabric tensor is given by

$$F_{\alpha\beta} = \frac{1}{N_c} \sum_{c \in V} n_\alpha^c n_\beta^c \qquad \text{I-20}$$

where α and β are the components in a reference frame. By definition, *tr(F)=1.* The anisotropy of the contact network is given by the difference between the principal values F_1 and F_2.

$$a = 2(F_1 - F_2) \qquad \text{I-21}$$

$\theta_{i\text{-}j}$ is used to express the orientation of the contact $c_{i\text{-}j}$. To be specific, $\theta_{i\text{-}j}$ means the angles of the normal of the contact surface with horizontal plane. With $\theta_{i\text{-}j}$, the contacts orientation of each image could be shown with rose diagrams. Therefore, it could be easily imagined that, the difference *of* $\theta_{i\text{-}j}$ and $\theta_{j\text{-}i}$ is π.

$$a = \frac{2}{N_c} \left| \sum \sin^2\theta_{i-j} - \sum \cos^2\theta_{i-j} \right| \qquad \text{I-22}$$

If *a* equals to 0, the material is absolute isotropy. However, if *a* equals to 1, the material shows a significant anisotropy.

I.3.4.Factors which influenced the packing process

The granular fabric develops mainly because of contact loss and gain. The fraction of lost and gained contacts depends on the contact orientation. Some factors which influenced packing process are studied by some scientists.

a.Shape of particles

The particle shape is one of the most important variables in the packing process. Many authors focused on some shapes of particles, e.g., spheres [68], ellipsoids [69] and regular convex polyhedral [70] to study packing characteristic and performed some experimental tests. In addition, the relationship between particle shape and packing density has been studied. The effect of different 3D object such as cube, cylinder, spherocylinder, cone, tetrahedron, and sphere on packing density of granular material has been revealed. It has been found that the packing density reached peak value when the particles are cube and decreased as the number of sides increased [71]. Additionally, the relation between Aspect ratio, particle size and the fabric of the packing of granular were investigated [72] [73] [74]. Zhao et al [72] used two parameter η and ζ, representing aspect ratio and blockness respectively, to describe different type of particles (Fig I-18) composing different packing and investigated the relationship between these parameters and packing density. The results obtained with a numerical simulation of a super ellipsoid model using DEM showed that η and ζ could significantly affect packing density, correlation number and anisotropy while the distribution of particle orientation is more sensitive to ζ than to η. Abreu et al [75] performed DEM simulation with different packing of various shapes of spherocylinder particles. In his simulation, the shape of spherocylinder could be described by the aspect ratio φ which could be calculated as the ratio between its length and diameter (Fig I-19). To study the effect of shape, all the packing has particles with the same volume and density but different aspect ratio. According to his result, the porosity decreases to minimum value then increases with aspect ratio increasing. Thus, the aspect ratios affect the porosity significantly and an extreme point of aspect value could be found to make the packing densest (Fig I-20).

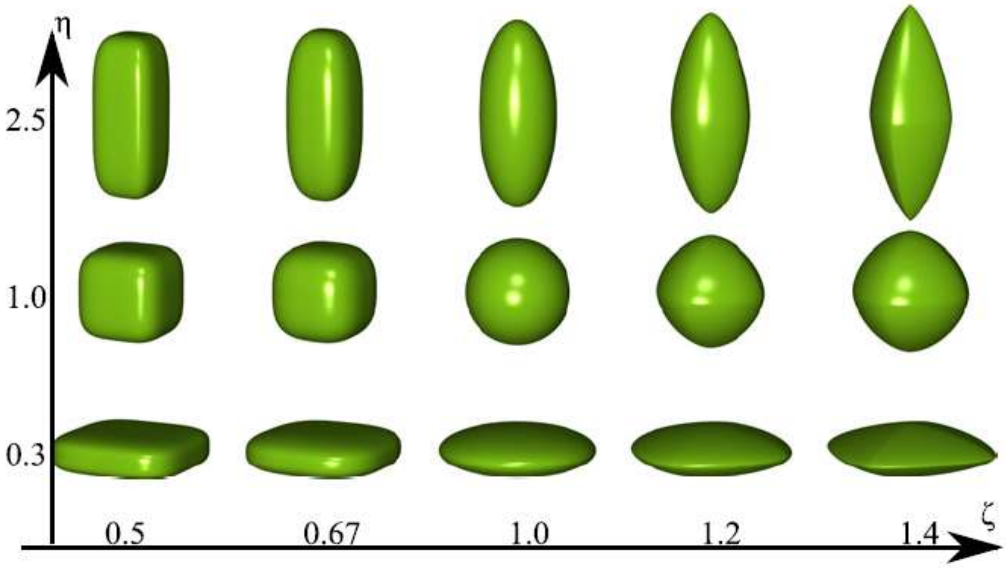

Fig I-18 Examples of shapes used in Zhao's work

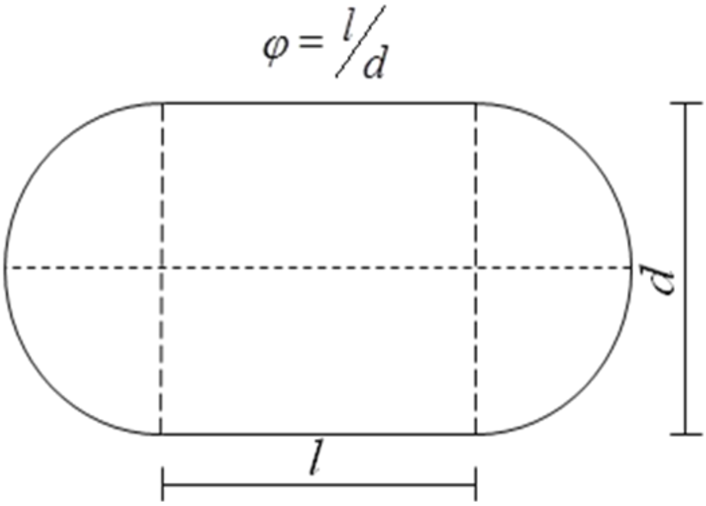

Fig I-19 Representation of a spherocylinder

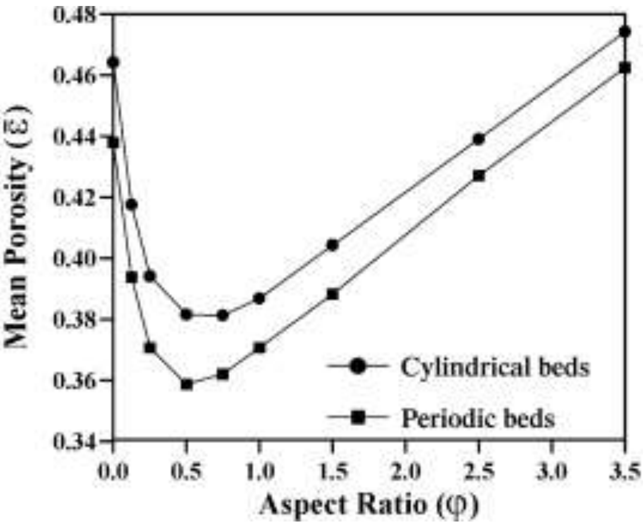

Fig I-20 Porosity as functions of particle aspect ratios of Abreu' work [75]

b.Diameter conditions of particles

The influence of particles diameter has been studied in several works. For monosized and polysized particles, the mechanical behaviour of granular material showed great difference [76] [77].

For monosized particles sample, there are two packing states including random loose packing (RLP) and random close packing (RCP). The definitions of the two states were given by Berryman in 1983[78]. He considered that, in the RCP state, any increase in packing density is impossible. On the contrary, the RLP refers to the loosest packing which could maintain mechanical stability. That is to say, for the particles whose scales are big enough to get rid of Van der Waals force, the RCP state would give a maximum packing density. In three dimensions and two dimensions, the packing density is 0.6366±0.02 and 0.82±0.02, respectively [79]. As for RLP, the packing density is affected by the particle's mechanical behavior. For cohesive particles, the packing fraction of RLP can range from 0 to 0.64. For cohesionless particles, since friction between particles may decline the packing density [80], it may vary with friction coefficients in a narrower range, probably from 0.554 to 0.64. For cohesionless and frictionless particles, it is the same as RCP [81].

The comparison between packing densities obtained with different particles diameter conditions has been made by Wong et al [82]. He explained that, ideally, the packing density of polysized particles is bigger than the packing density of monosized ones. The reason is that the particles of smaller sizes could fill up the gaps between the bigger ones. If the process of filling up could be extended infinitely by smaller and smaller particles, all the voids could be filled up and the packing density could be close to 1. The process above was called filling effect. Nevertheless in reality, the above process is very difficult to achieve due to a lot of restriction. For example, it is easy to imagine that the diameter of big particles and the diameter of smaller particles which filled up the gaps should maintain a certain proportion. By contrast, if the fine particles are not small enough to fill up the gaps between larger ones, the larger particles would be pushed apart which causes an increase in void volume and decrease in packing density and this process was called loosening effect [83] (Fig I-21).

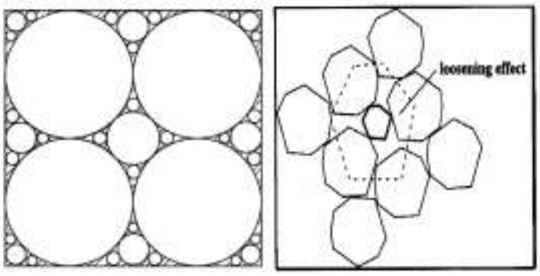

(a) (b)

Fig I-21 Different effects of packing of polysized particles [83]

(a): Filling effect. (b): Loosening effect

Some works showed interesting in the influence of some dynamic factors on material properties [84] [85]. Silbert et al [86] found the relationship between dropping height and packing density from the direction of energy and found that a bigger dropping height usually leads to a denser packing due to a faster energy accumulation. However, a faster energy consummation caused by friction, deposition, may result in a loose packing. Random closed packing states could be achieved by some physical methods such compaction and vibration. An applied DEM model simulates the process from random loose packing state to random close packing state through one dimensional vibration to acquire the proper vibration amplitude and frequency.

Casagrande [88] defined the concept of critical state to study granular material. When the phase of critical state is reached, deformation continues without changes of packing density (Fig I-22). For dense packing, the granular material reaches critical state as s result of dilation. However, for the material of loose packing, it would reach critical state when under contraction. In several works, it is believed that critical coordination number and critical anisotropy should be considered as a combination that describes critical state. It is found that the relationship between packing density and coordination number is influenced by anisotropy of the contact orientations.[89] [90].

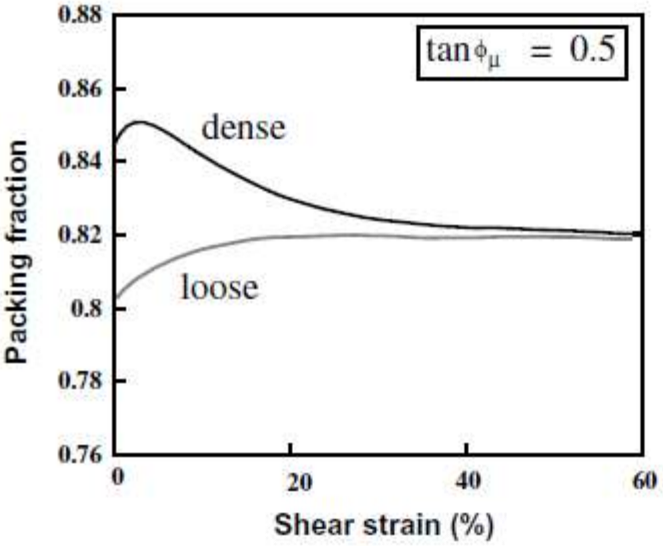

Fig I-22 Simulated tests on loose and dense assemblies of Casagrande's work [88]

I.4.Mechanical behavior of multiple particles considering particle failure

Mechanical behavior of granular material has been studied for hundreds of years. Some classical theories were born concentrating on this field. For example, the Mohr–Coulomb theory which is named in honour of Charles-Augustin de Coulomb and Christian Otto Mohr is used to describe the shear strength of soil [91]. Karl von Terzaghi studied the filtration theory of consolidation and principal of effect stress [92]. Moreover, the crushing of particles which act as components of granular may exert significant influence on the mechanical property of granular material due to changed grain size distribution. It may lead to an upheaval of the micro structure. As a result, particles' crushing has attracted great attention in recent years.

I.4.1.Factors influencing the mechanical behavior of granular assemblies

It is found that except for the stiffness of single particles, some other factors also influenced the mechanical behavior of granular media. It is believed that particle size and shape are affected by its generation history. In return, particle size and shape reflect the material behavior. In addition, the grain size distribution (GSD) and the interparticular friction also make a crucial impact on the mechanical response of the material. Moreover, microstructures which are formed in the connection paths of contact points between particles also influence the mechanical behavior of granular assemblies.

a.Influence of particle shape

Wadell [93] and Krumbein [94] introduced three important parameters in particle shape. Sphericity or eccentricity refers to the global form of the particle and describes the uniformity among the particle's length, height, and width (Fig I-23). Sphericity can be calculated as the diameter of the largest inscribed sphere relative to the diameter of the smallest circumscribed sphere. Roundness or angularity describes the scale of major surface features which are typically one order of magnitude smaller than the particle size. Roundness could be quantified as the average radius of curvature of surface features relative to the radius of the maximum sphere that can be inscribed in the particle. Smoothness or roughness describes the particle surface texture relative to the radius of the particle.

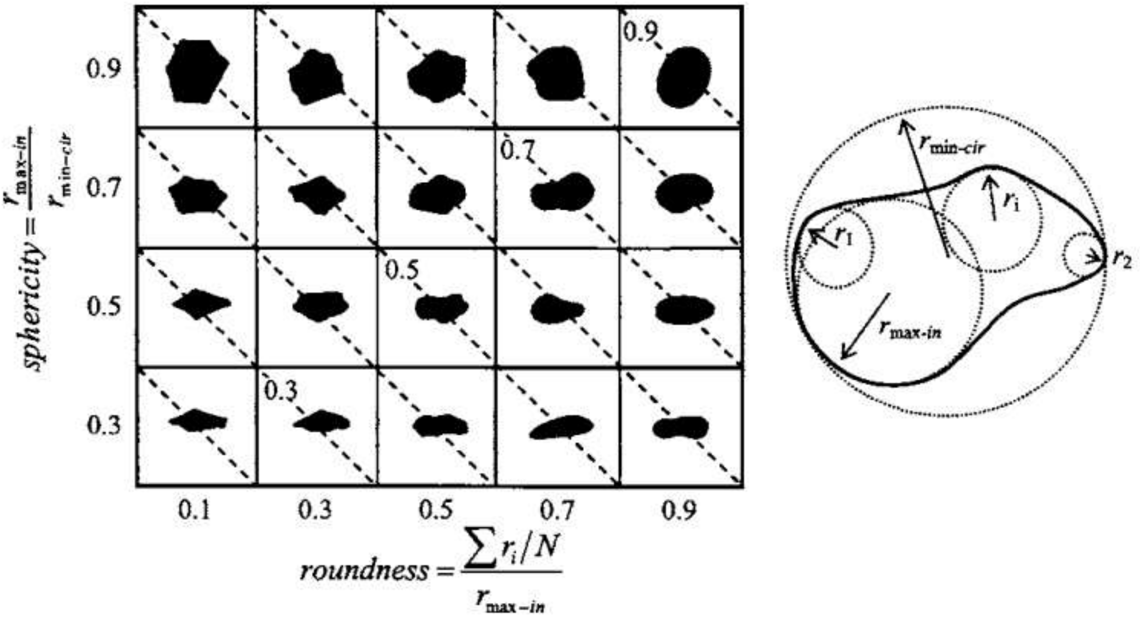

Fig I-23 Particle shape determination—sphericity *S* and roundness *R* chart.[94]

In addition, Wadell [93] also believed that sphericity, roundness, and smoothness form an independent set. Sphericity and roundness increase because of abrasion, however they do not increase proportionally. Furthermore, although chipping of a particle may increase the sphericity, it decreases the roundness. All in all, round particles can have nonspherical shape and equidimensional particles can be very angular

Cho et al [95] studied the results from published papers to explore the effects of particle shape on void ratio. For the particle assembles with similar GSD, both e_{max} and e_{min}, and the void ratio difference $I_e=e_{max}-e_{min}$ increase as roundness and sphericity decrease (Fig I-24). The reason is that irregularity hinders particle mobility and their ability to attain dense packing configurations. In the case of low sphericity, platy particles bridge gaps over grains and create large open voids.

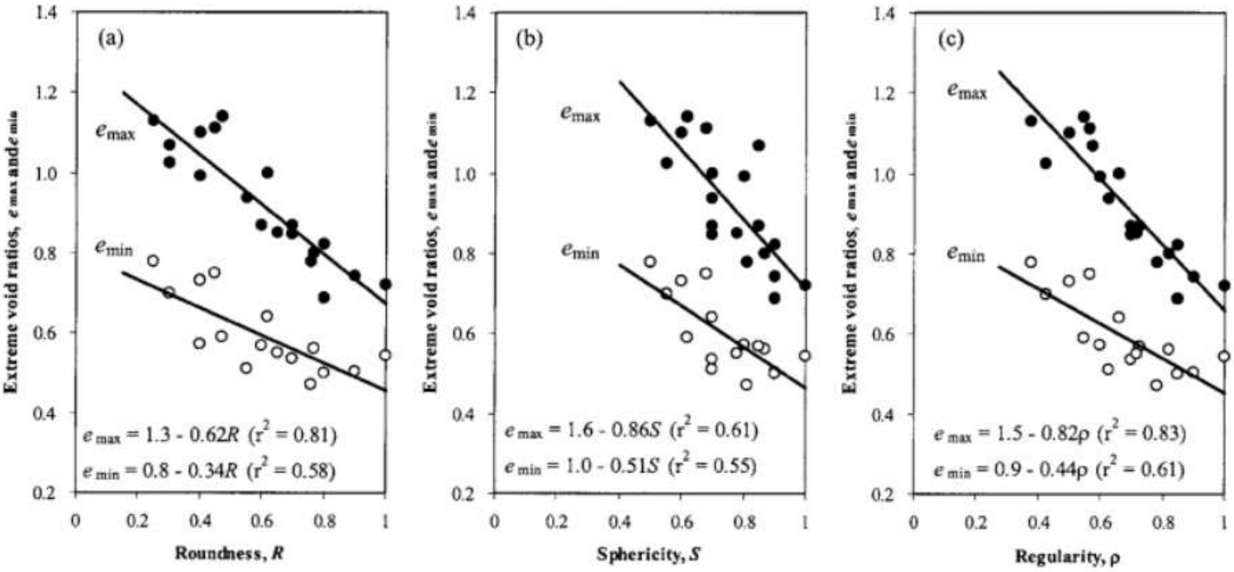

Fig I-24 Effect of particle shape on void ratios from Cho's phenomenon [95]

Ashmawy et al [96] used DEM to model the liquefaction of angular soils. In this work, a new method was applied to model angularity of particles as a series of overlapping, rigid connected distinct elements of equivalent properties. Simulation of cyclic shear tests were carried out on representative volumes of six materials with the same size distribution to evaluate the dependence of liquefaction susceptibility on particle morphology. Based on the result, at the maximum void ratio, the susceptibility to liquefaction is independent of particle shape. However, the liquefaction resistance increases with particle irregularity in the case of samples prepared at the same void ratio.

Maeda et al [97] simulated the deformation of granular material with different particle shapes via 2D DEM under different stress levels and densities. Circular (Fig I-25a) and non circular (Fig I-25b-e) particle elements were considered to investigate grain shape effects on macro bahavior of granular material. He found that macro deformation and failure of granular materials were induced by not only interparticular sliding but also particle rotation due to the buckling of the microstructure. The coordination number N_{co}, which represented the stability of fabric, increased under isotropic compression and decreased under shearing. Consequently, N_{co} was revealed to have a critical state which corresponds to the relation $e-p-q$ in critical state soil mechanics The results also demonstrated that the critical line moved upward with the increase of angularity (Fig I-26).

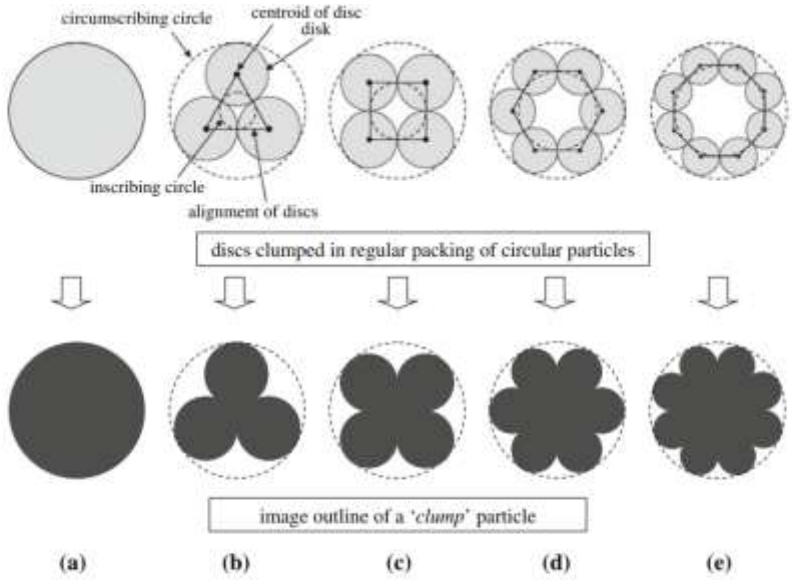

Fig I-25 Particle types used in the DEM in Maeda's work: a c101 (circle); b c103 (triangle); c c104 (quadrate); d c106 (hexagon); e c108 (octagon) [97]

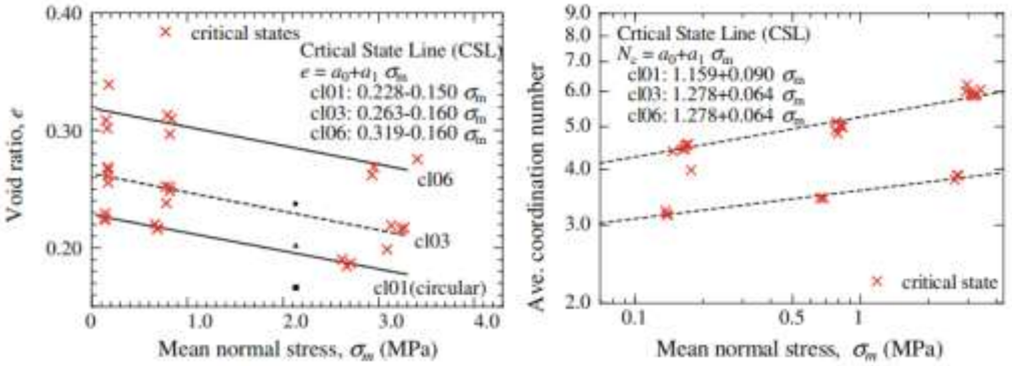

(a) (b)

Fig I-26 Particle shape effect on critical state line of DEM samples in Maeda's work [97]

(a): Critical state line in void ratio (b): critical state line in coordination numbers

b.Influence of GSD

Igwe et al [98] performed tests on three silica sand samples, well graded, intermediately graded and narrowly graded to investigate the GSD effect on the mechanical behavior of granular material. The results suggested that as the coefficient of uniformity increased, both the peak and critical strength of sand increased. Well graded samples have a higher static liquefaction resistance the poorly graded samples.

Through simulating a series of numerical triaxial tests, Wood et al [99] used DEM method to study the influence of GSD on the mechanical behavior. The results indicated that the initial GSD influences the critical state of the material. To be specific, the critical state lines in the *e-p'* plane shift downward with an almost constant slope as the coefficient of uniformity increases (Fig I-27).

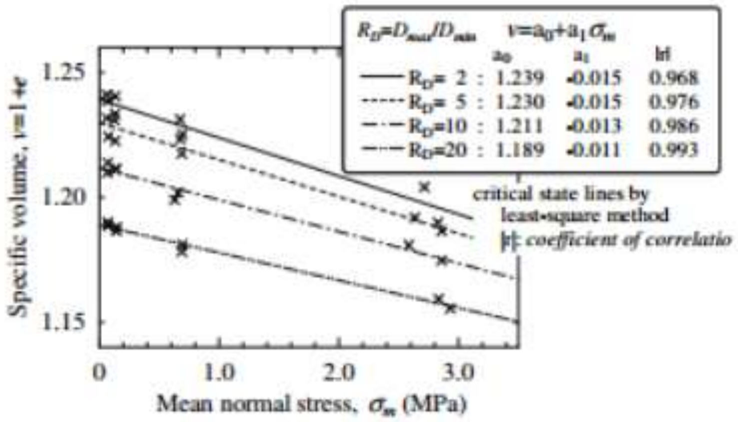

Fig I-27 Critical state lines for different values of R_d from Wood's work [99]

Bandani et al [100] performed a series of triaxial tests to investigate the effect of particle breakage on the current location of the critical state line. He found that the critical state line shift with the particle breakage. The current GSD could affect the behavior of the material yet the initial still acts as a key function.

I.4.2.The factors influencing particles crushing

Particles crush is a complex mechanical behavior affecting the material during loading. Under some specified tests conditions, particles of granular material may crush. In addition, several works investigating the factors which could influence the particles crush has been also been carried out.

a.Particles' strength

The nature and strength of the source rock from which the particles originate are critical in assessing the vulnerability of the material to particle failure Single particles mechanical resistance such as tensile strength [101] and shear strength [102] could affect the granular material behavior. Billam [103] proposed a compilation of several particle crushing tests of different particles. It is observed that the breaking force depends on the nature of the material (glass, quartz, limestone, sand and chalk). Lo et al [104] performed triaxial tests on materials of different mineralogy but with the same initial particle size. The results indicated that the particles breakage depends on mineralogy (Fig I-28). Yamamuro et al [105] performed drained triaxial compression tests on dense Cambria sands. He found that the most fundamental factor influencing crushing degree is the inherent strength and the effective stress state.

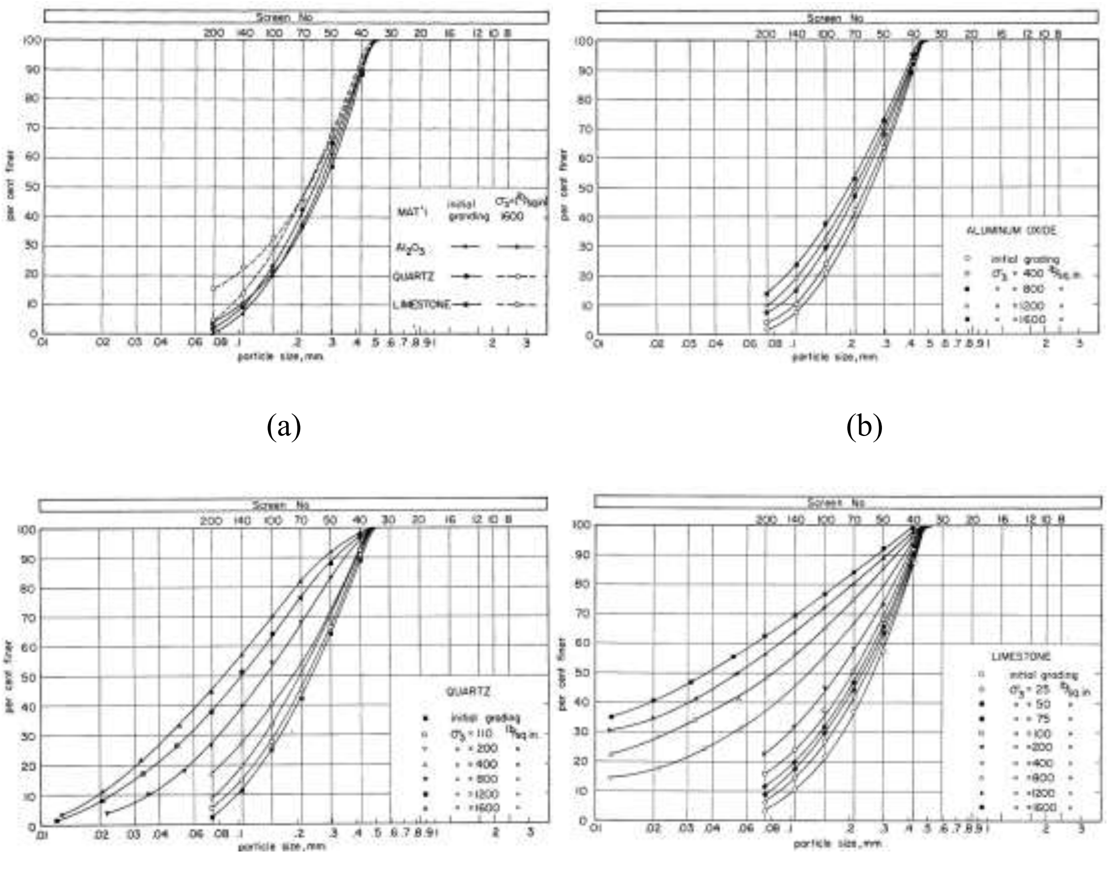

(a) (b)

(c) (d)

Fig I-28 Influence de la minéralogie sur la rupture des grains of Lo’s work (a) GSD of beginning and after consolidation, (b) GSD of aluminium oxide after tests, (c) GSD of quartz sand after tests and (d) GSD of limestone sand after tests

However, larger stress levels always result in larger amount of particle crushing. In the case of creep, the amount of particle crushing is also a function of time. In addition, if the stress states could reach a certain value, particle crushing keeps occurring at a decreasing rate although the loading process has stopped [106].

b.Shapes of particles

Particle shape is another dominant factor affecting particle breakage behavior. Santamarina et al [107] summarized three principle scales to describe a particle shape including sphericity, angularity and roughness which affect soil behavior. The sphericity could influence the fabric anisotropy, resulting in an effect on deformation, strength, conduction and diffusion. Briefly, sphericity could increase the stiffness and residual friction angle. Additionally, the increase of angularity and roughness could cause a decrease in small-strain stiffness and a growth in high-strain strength. Afshar et al [108] proposed that particles with same size may have different shapes which may influence particle crushing behavior. Therefore, he built a DEM model for recycled construction and demolition materials on particles assembly crushing tests. Flaky, elongated and bulky particles were simulated respectively. The results show that the granular material which is closer to sphere has a higher resistance to crushing. However, the granular material with a higher flakiness is earlier to break under loading condition (Fig I-29).

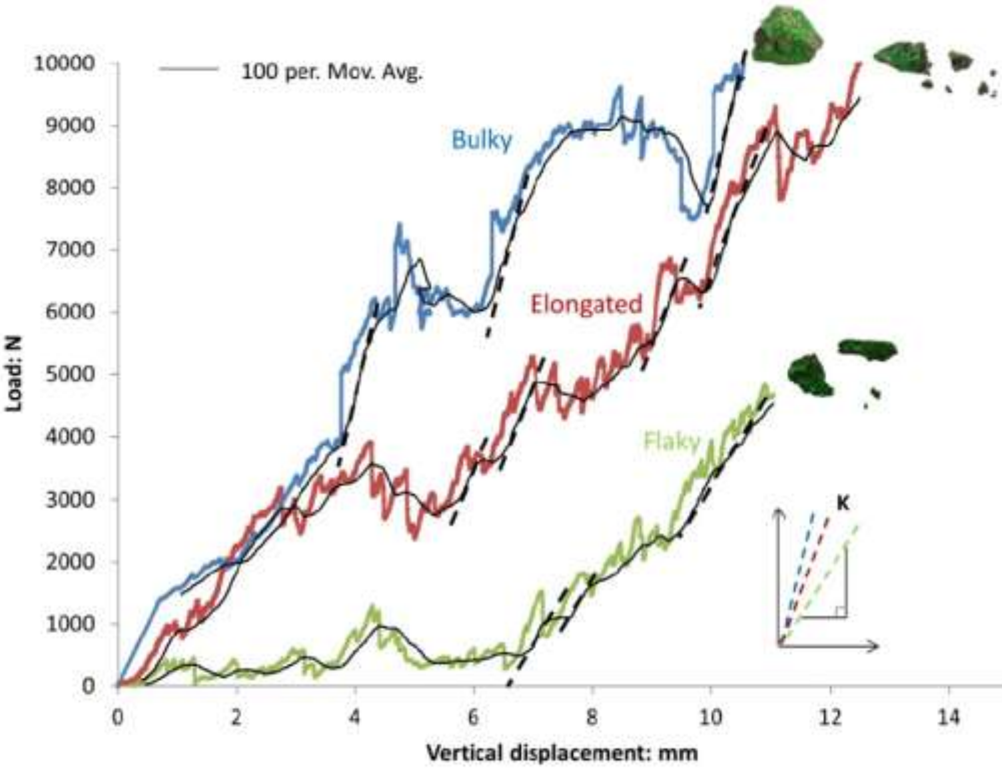

Fig I-29 Comparison of different particle shape in particles assembly crushing tests of Afshar's work [108]

c.Initial GSD of the material

Another factor influencing the grain crushing is the grain size distribution (GSD) of the granular material. As early as in 1965, Marsal [109] indicated that, the possibility of breakage of a soil particle increase with its size because the increasing particle size could lead to a growing of the normal contact force. Moreover, if the defects inside the particle are considered, the increasing particle size would also result in a growing probability of defects. In most cases, we consider that a granular material with a better GSD could experience a better mechanical property. However, according to several research, this rule does not work on the breakage behavior of granular material. As early as in 1985, Hardin [110] analyzed data of several granular materials with different sized particles under loading. He used b_p to describe the potential for breakage of a particle whose size is D.

$$b_p = log_{10}\left[{}^{D}/_{D_{min}}\right] \text{ for } D \geq D_{min} \tag{I-23}$$

$$b_p = 0 \text{ for } D < D_{min} \tag{I-24}$$

where D_{min} refers to the minimum size of particle which could crush for a certain kind of granular material. This value needs to be estimated with laborotary tests.

When b_p represents the potential for breakage for a given size fraction and df is a differential of percent passing divided by 100.The potential for breakage of the granular could be the integration of B_p.

$$B_p = \int_0^1 b_p \, df \qquad \text{I-25}$$

The amount of crushing could be represented by

$$B_t = \int_0^1 (b_{p0} - b_{pl}) \, df \qquad \text{I-26}$$

Where b_{p0} equals to the initial value of b_p and b_{pl} equals to the value of b_p after loading.

Measurements show that the values of B_t are approximately proportional to B_p is the samples are loaded along a specified effective stress path to the same state of effective stress. In other word, if the only variable is GSD, B_t is proportional to B_p (Fig I-30).

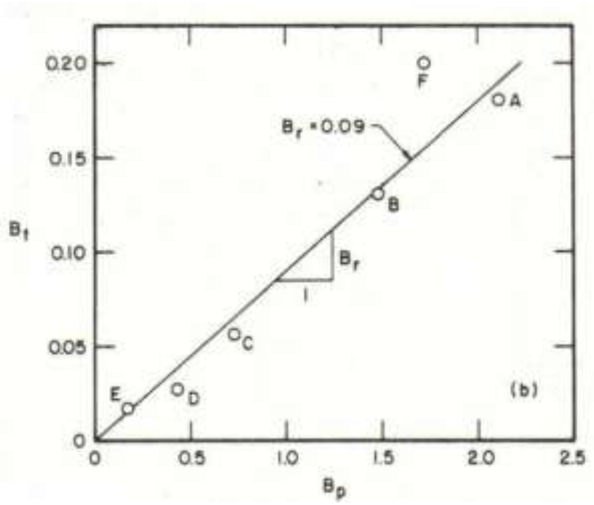

Fig I-30 Relationship between total breakage and breakage potential [110]

The relative breakage could be represented by

$$B_r = {B_t}/{B_p} \qquad \text{I-27}$$

Therefore, the relative breakage B_r is independent of particle size distribution if the particle size distribution is the only variable.

Recently, Rozenblat et al [111] compared 12 kinds of granular material with diameters speared from 0.7-1mm to 4-5mm. He found that the gap of crushing stress is less than 20% (Fig I-31). Therefore, he made a conclusion that the particle strength defined by crushing stress is approximately independent from particle size distribution.

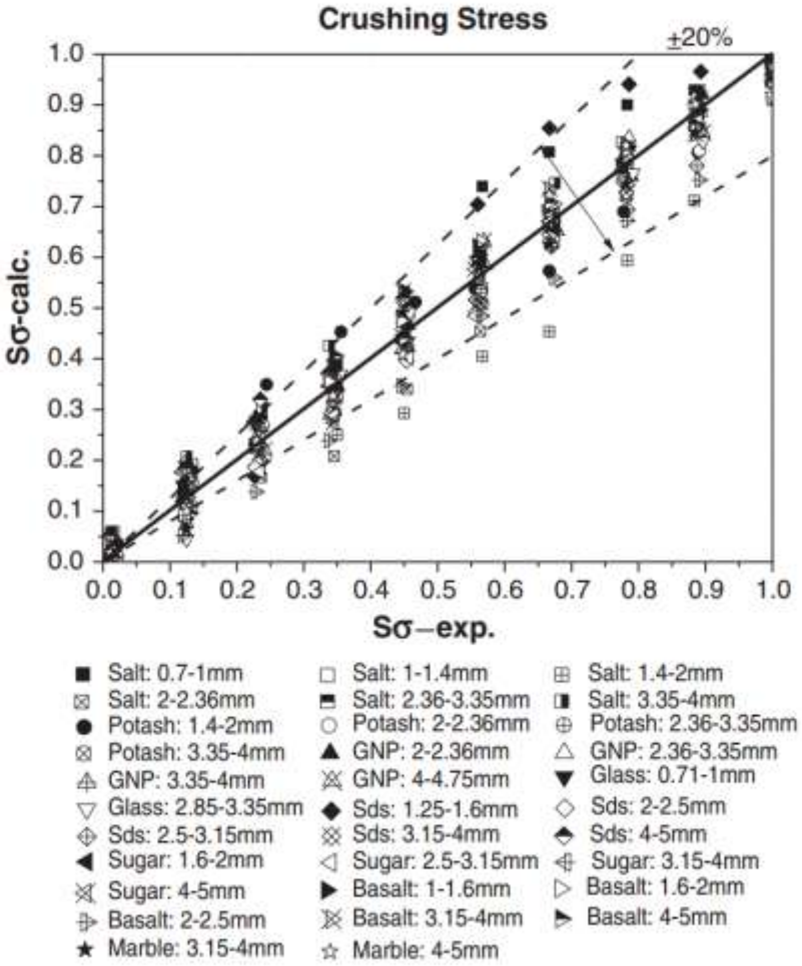

Fig I-31 Comparison of the particles diameters in terms of crushing stress of Rozenblat's work [111]

d.Loading conditions of the tests

The loading condition is another key factor of particle breakage. A comparison of cyclic and monotonic loading on ballast has been studied. They found that the frequency of cyclic loading could make a significant influence on the deformation and breakage of particles [112] [113]. Cheng et al [115] indicated that, the confining pressure could influence the particles crushing after imported microspheres bonded together to simulate crushable particles with DEM. Lackenby et al [114] conducted several high frequency cyclic triaxial tests on ballast. The obtained results demonstrated that for the same material, an optimized confining pressure could be found to minimize the particle breakage. Kou et al [116] investigated the influence of friction of the container walls on the particles breakage (Fig I-32). His results demonstrated that with friction on the boundary, the particles breakage starts earlier and they are more concentrated on the boundary. Moreover, without boundary friction, particles breakage occurred less on the top.

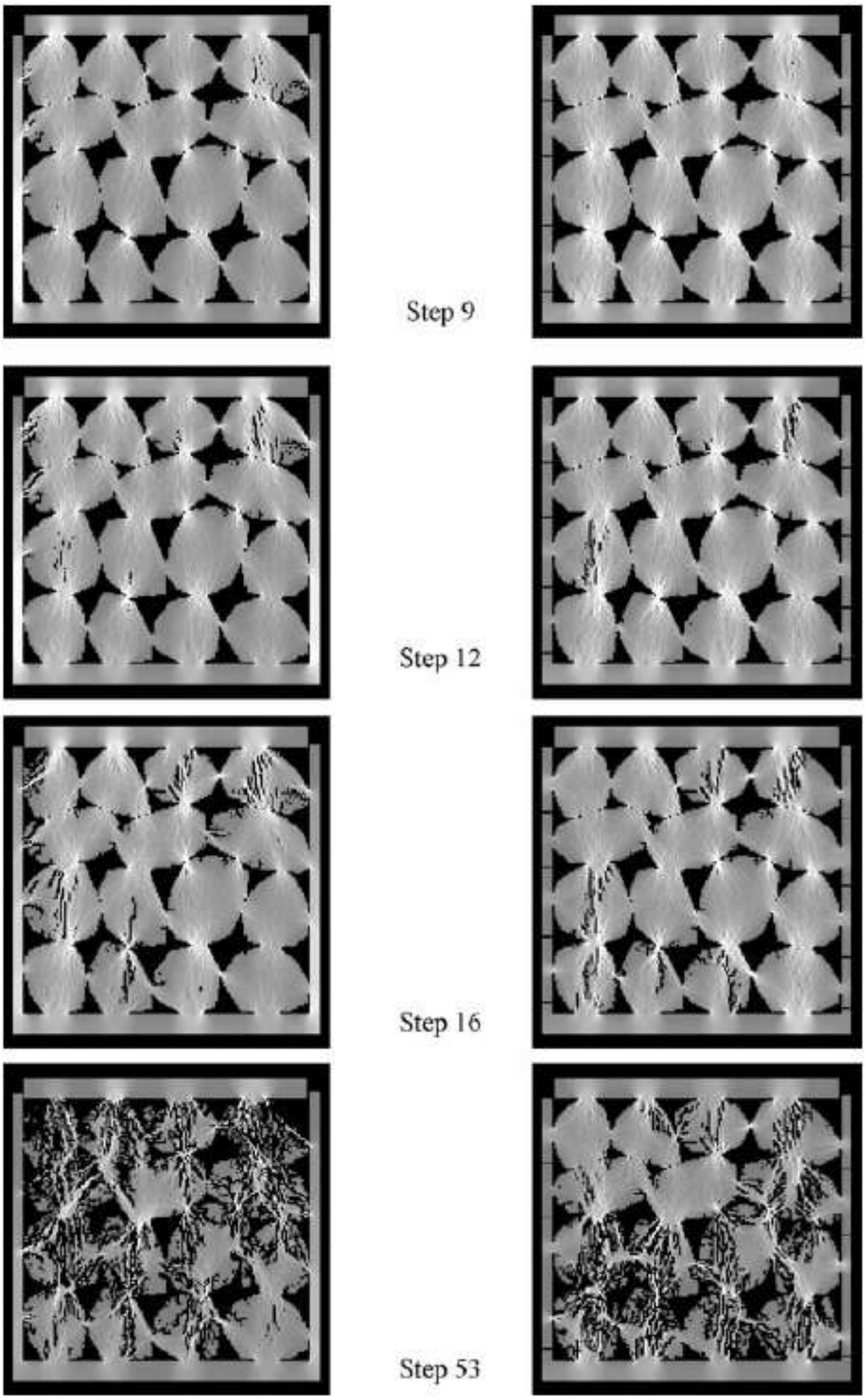

(a) (b)

Fig I-32 Comparison of the particles breakage characteristic of different boundary friction conditions of Kou's work. (a) boundary with friction (b) boundary without friction

I.4.3.The influence of particles crushing to the behavior of material

As mentioned before, the particles breakage could lead to significant change on the mechanical property of the granular and some changes are very obvious. For example, the mean size will be smaller. The shapes of particle are becoming less angular and surfaces of particles are becoming less rough for the reason that the angular corners and shape edges are easy to cause stress concentration and crush. Influenced by the above factors, some other properties which are under the influence are worthwhile of pursuing further. Thus, some scientist studied the evolution of some kind of mechanical index of granular material due to particles breakage.

a.GSD of the material

First of all, the particles breakage could inevitably cause a reduction of the mean size of particle and influence the GSD of the material. Fukunoto [117] [118]investigated various tests results of uniformly graded soil sample and gave an equation to calculate the percentage of particles remaining of each sieve to make a GSD lines. In addition, he also pointed out that judging crushing degree of the particles according to the amount of particles passing through the smallest sieve is inappropriate. As the sizes of particles are changed, the GSD curve of the granular material evolves. According to Einav [119] [120], the surface of GSD after tests is higher than the surface of GSD before the test and lower than the surface of GSD of an ultimate state. He named the distribution of the three stages including initial distribution, current distribution, and ultimate distribution. He defined a relative breakage index B_r equals to the quotient of the closed areas defined by the three GSD lines (Fig I-33). That is

$$B_r = \frac{B_t}{B_p} \tag{I-28}$$

Besides, Br is limited by

$$1 \geq B_r \geq 0 \tag{I-29}$$

Where $B_r=0$ means uncrushed particles and $B_r=1$ means a complete breakage of particles.

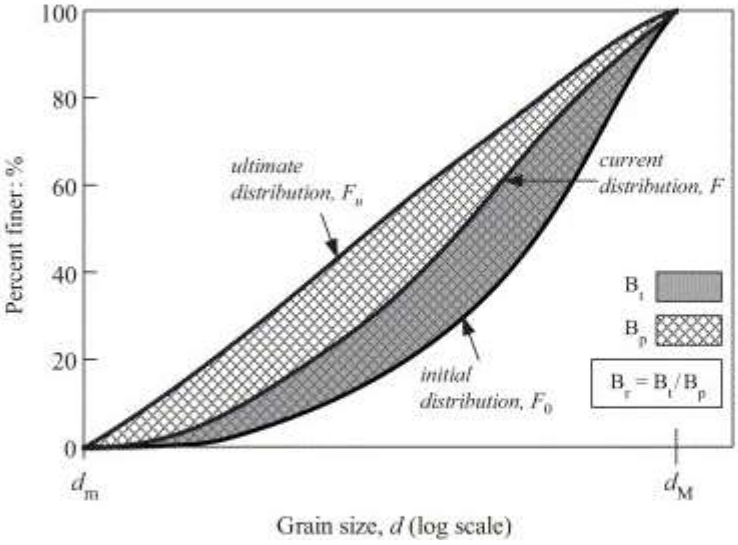

Fig I-33 The definition of B_r in Einav's work [119] [120]

b.Strength and deformation behavior the material

Particle crushing could affect the mechanical behavior of the granular material. If the pore water pressure is taken into consideration, particle crushing could lead to a change of drainage performance, and then affects its strength [121].

The conventional wisdom said when particle crushing occurs, the less angular aggregates could lead to a reduction of the friction angle and thus the shearing strength decreases [122]. A stress–dilatancy relationship for sand under a triaxial loading condition was built by Ueng et al [122] which could be used to study shear strength with the consideration of energy consumption due to particle breakage. Fulung sand, Tamsui River sand were tested and the results indicated that the rate of energy consumption by particle crushing could affect the rate of increment of surface area of particles. Besides, the shearing strength of the material could be affected by the ratio of energy consumption rate versus the surface area. In Salim and Indraratna's work [123], a model incorporating the deviator stress, dilatancy, friction angle and energy consumption considering particle breakage was built to study the effect of particle crushing to shear strength. Finally, he found that the rate of energy consumption has noteworthy relationship with the rate of particle crushing. Additionally, the friction angle increases with the rate of particle crushing, leading to a decrease of material's shearing strength.

I.4.4.Descriptions of mechanical behavior of granular material

Based on a lot of research, numerous scientists tried to describe the granular material from different perspectives with different methods.

The mechanical behavior of granular materials is dependent on the properties of the particles constituting the material. In order to build correlations between continuous medium and discontinuous medium, Hicher et al [124] presented a methodology for connecting parameters of classic models for continues media (elasticity, plasticity) and physical parameters of the particles (form, size, grain size distribution, etc.).

Some scientists built constitutive models of granular material considering particle breakage. Based on critical state and plasticity theory, Salim et al [125] developed an elastoplastic constitutive model for coarse aggregates during triaxial shearing, which could forecast the stress-strain relation and volume change of coarse aggregates. Russell et al [126] described the behavior of granular material considering particle crushing by building a constitute model with a three-segment critical state line within a boundary surface. Chavez et al [127] built a model for rockfill under triaxial stress tests. His model was based on hardening plasticity with the consideration of critical state concept and suction effect. Liu et al [128] developed a plasticity constitutive model for sand based on the concept of critical state soil mechanics and his model could be used to evaluate sands crushing under cyclic loading. Hu et al [129] introduced an elasto-plastic model whose feature contains the critical state line movement because of the particles breakages. A verification with some test results demonstrated that his model could accurately reflect the mechanical behavior of crushable granular material and predict the GSD evolution during the test. Under isotropic and trixial loading, Daouadji et al [130] developed an elasto-plastic constitutive model which could calculate the behavior of granular material. He described the position of critical state line according to the amount of energy sufficient for particle crushing and provided a curve on which the critical state line in the e-logp’ coordinate system dropped accompanied with the evolution of particle gradation. His model considered the local strength of particle and was validated with two kinds of material and the results reproduced a good accuracy of the granular material mechanical behavior. After night years, Daouadji et al [131] introduced an enhanced constitutive which considered the influence of amount of particle breakage. The model was calibrated with a comparison of tests on three different kinds of material and the simulations were close to tests results.

Chapter II. Experimental and Numerical Investigation of Breakage of Single Particle of Porous Material under Uniaxial Compression

II.1.Introduction

II.1.1.Research Background

The mechanical behavior of granular materials has been studied since the 19th Century. Among these studies, three different scales, i.e. macroscopic, mesoscopic and microscopic, can be emerged to analyze the behavior of this type of material. The most mature theories which could be applied on practical engineering problems stay on macro and mesoscopic scales such as Mohr-Coulomb elastic-ideally plastic model, hypoplastic or elastoplastic models and so on. All these models consider granular material as a continuous and homogenous media, which contains an infinite number of unbreakable and inseparable particles. Another type of model concerns assembly of grains interacting each other and are known as Discrete (or Distinct) Element Models. The grains are mainly considered as non-deformable and non-damaged.

However, the physical and mechanical characteristic of granular material under combined loads can be easily affected by the deformation and breakage of grains having low mechanical properties or under high effective stresses [10] [11] [12] and [13]. Grain breakage tends to increase the compressibility and lower shear strength of the assembly.

The study of granular material based on microscopic approach has been started since years by a large number of scientists. As early as 1967, Marsall [109] studied the plane strain compression of an ideal granular material. Later, numerous series of laboratory tests called Brazilian test have used 3D cylindrical specimens to simulate 2D circular particle breakage. However with this type of test, the stress field inside the cylindrical sample is different from the stress field inside a spherical one [133]. For numerical modelling of single particle breakage, a crucial difficulty is to model the real 3D geometry structure of a particle [133]

Particle fracture could be modelled using Discrete Element Method (DEM) in which particles are simulated as an agglomeration composed by several tightly-connected sub-particles [37]. Recently, a new method finite element-discrete element method (FDEM) has been proposed. In FDEM, discrete element could be meshed into finite elements in order to obtain deformable particle.

All the laboratory experiments above mentioned are based on the particle's external morphologies and obtain its external displacement and strain feature. Even for numerical simulation, although the internal structure could be built, the parameters for the internal geometry are estimated according to the traditional laboratory experiments results whose experimental focus are not on the internal appearance. Therefore, for some kinds of particles whose internal structure is complicated enough to influence its mechanical behavior, the internal microstructure during the crushing process is difficult to investigate. X-Ray micro-Computed Tomography Scan (μ-CT scan) could provide an effective instrument to understand the internal microstructure of a particle. A μ-CT scan uses X-ray projections taken at different angles to produce enough cross-sectional images of a sample, in order to reconstruct its real 3D appearance both externally and internally including internal flaws [45]. The first X-Ray micro-Computed Tomography Scan utilized in geotechnical field research was by J. Desrues[46] in 1996. He studied strain localization in triaxial tests on sand. Alshibli et al. [50] used μ-CT scan to study the evolution of silica particles breakage during uniaxial test. They imported the obtained 3D geometry into an XFEM model.

II.1.2.Aim and objectives

The aim of this chapter is to study the breakage behavior of single spherical particle made by porous heterogeneous material. Therefore, a series of experimental and numerical studies were performed. First, uniaxial compression tests on single particles were carried out. X-Ray Computed μ-Tomography Scan was also used to assess the internal and external morphology of the sample. This information was then used for numerical investigation of the loading process of single particles.

This chapter is organized with seven parts which addressing different contents. References among parts could guide the reader to focus on specific topics. In part 2, the experimental apparatus and methodologies will be described. In part 3, numerical models of 3D geometry obtained from CT test exported into ABAQUS® software will be introduced. Two sets of models were built to for further numerical simulations. In part 4, the experimental results are analyzed. In part 5, the results of numerical simulation of set 1 are analyzed. In part 6, the results of numerical simulation of set 2 are analyzed. In part 7, a conclusion summarizes the main results.

II.2.Experimental apparatus and methodologies

II.2.1.Sample properties

Porous particles made by light expanded clays were used in all laboratory tests. All the particles are approximating spherical with rugged outside surfaces. This material is a type of porous heterogeneous material, which has a very low density due to existing randomly distributed voids inside each particle. The particles have a relatively important big grain size compared to the particles of sands, thus it is easier to observe the tests process. Moreover, the material has a low brittle behavior, thus the particles are easy to fail. The mean density of particles is 1.241g/mm^3 which was obtained from tests on 12 randomly chosen individual particles (Fig II-1).

Fig II-1 Particles used in the tests

II.2.2.Uniaxial compression tests

Several particles were tested individually. Uniaxial unconfined compression tests were conducted on each single particle. During the uniaxial compression tests, a digital camera was used to record images at constant time interval. Then the Digital Image Correlation technique (DIC) was used to analyse the images. For all tests, the pixel size was 17 μm.

The loading system was an electro mechanic testing machine (EMTM). The EMTM was used to apply vertical load or displacement with a predetermined testing plan.

Camera and EMTM were controlled by computer. For the loading system, all data such as time, vertical displacements, vertical load, were measured by sensors and recorded. When the real-time load decreased by 40% of the already observed maximum load, the computer would surmise that the sample had lost its bearing capacity and the EMTM would stop the test automatically. If the particles are found losing capacity, the EMTM could also be commanded stop loading manually.

During tests, photos were taken by the camera and saved to computer at periodic intervals. Data from EMTM were also recorded by photo acquisition software in a same file with the photos number in order to synchronise time, force and displacement with each photo (

Fig II-2).

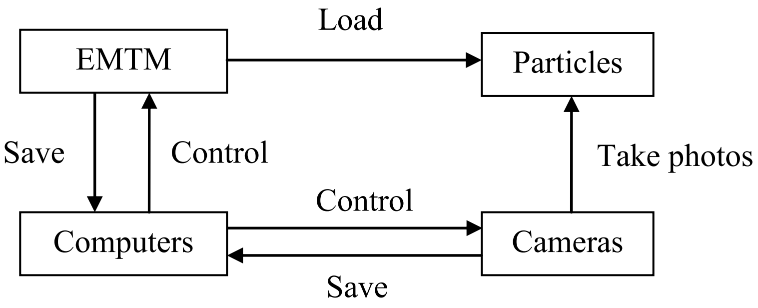

Fig II-2 Sketch of tests instruments

Before each test, a new particle was placed on the loading platform of the EMTM along with the camera. The load was then applied on the particle and camera starts working to record the whole particle deformation and breakage (Fig II-3). Material parameters and test conditions are presented in Table II-1.

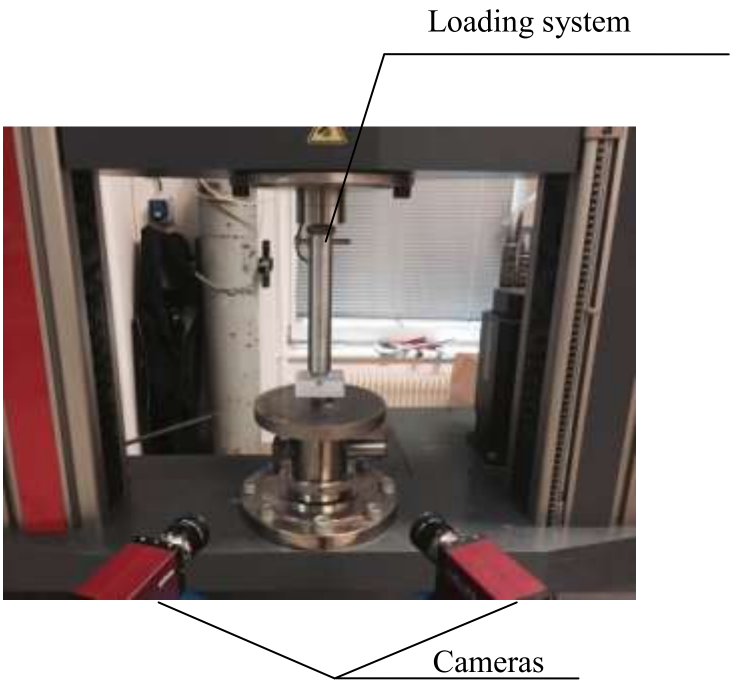

Fig II-3 Already assembled test equipment for simple particle tests

name	settings		
	diameter(mm)	mass(g)	loading speed (mm/min)
Test S_1	18.04	2.15	1
Test S_2	17.93	2.11	
Test S_3	18.00	2.13	
Test S_4	15.83	1.45	

Table II-1 Settings of single particle tests

II.2.3.X-Ray Computed Tomography scan

In order to study the real 3D structure of the particles, μ-X-Ray Computed Tomography (μ-CT) Scan was applied. A CT test was performed on the particle of test S_4 before the uniaxial test to acquire its geometry. Another CT test was conducted with a mini *in situ* compression setup to observe the inner failure morphology. The experimental system is produced by RX Solution Company and is composed by X-ray generator, a holder for specimen and a detector. The sample was placed on the holder, which was located between the X-ray generator and the detector. The holder is turntable whose rotation and translation could be control by computer (Fig II-4).

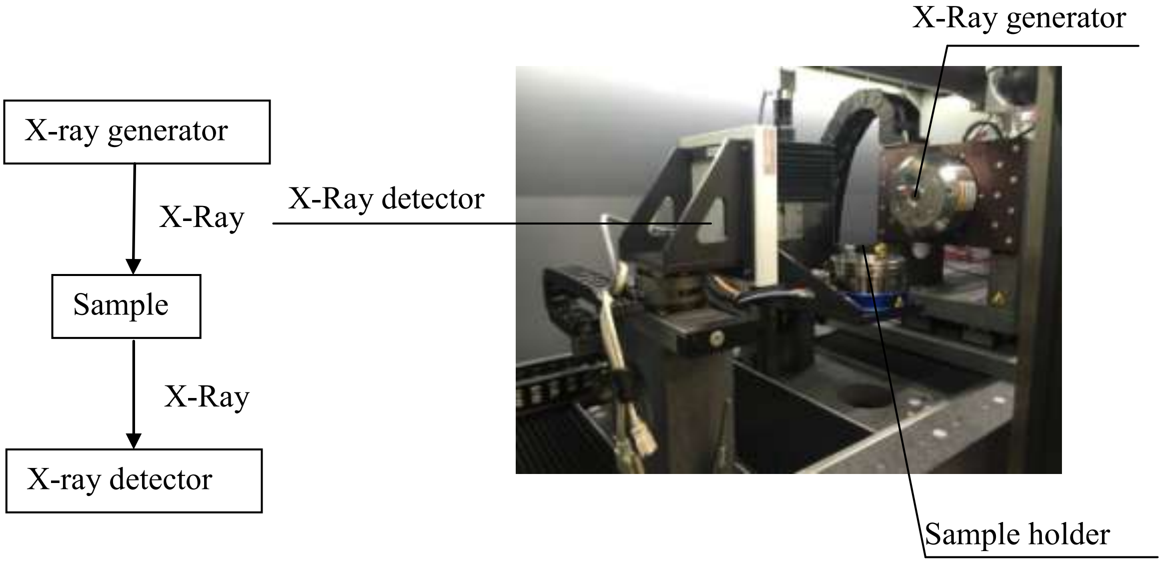

(a) sketch of instruments for CT tests (b) photo of instruments for CT tests

Fig II-4 Test equipment for CT tests

When X-rays travel through a sample, they are attenuated according to the geometry and material property of the scanned sample and the initial energy of the X-rays

$$I = I_0 exp\,(\sum_{i=1}^{N}(-\mu_i x_i)) \qquad \text{II-1}$$

where I_0 is the initial radiation, μ_i and x_i are the linear attenuation coefficient and the linear extents of the material for a total number of N materials.

The ratio I/I_0 could be obtained for each detector pixel for each projection. At any point this ratio is the sum of the absorption values along a single X-ray path. It is called the ray-integral and is defined by the following expression:

$$ln\frac{I}{I_0} = -\int_x \mu(x)dx \qquad \text{II-2}$$

Hence, the detector received X-rays of different signal intensity to produce greyscale projections of the sample. Before the test starts, according the geometry of the spacemen and the computational accuracy, the number of radiograph projections needed and the rotation angle between each projection is automatically calculated by the control system. When the test starts, the holder will rotate and at every specific rotation increment, one projection will be recorded. After the holder rotates 360 degrees, all the projections will be acquired and the CT scan will be complete. The projections would be saved with the corresponding rotation angles for further calculation. In our test, 895 projections were acquired

With the projections, reconstruction would be performed to acquire the cross sectional slices of specific areas of scanned objects. Reconstruction is the mathematical process of converting projections into two dimensional slices. The filtered back projection algorithm is the most commonly used [135]. Generally speaking, each projection is successively superimposed over a square grid at an angle corresponding to its acquisition angle. The superposition of the attenuation values will correspond to the features presented in the object. An increase in the number of angles could decrease the size of the square grid and thus increases the accuracy of the tomography image to represent the original object.

In our test, supporting computer software could finish the post-processing, allowing the user to observe the 3D inner morphology of the sample without destroying it. Finally, digital geometry processing was used to regenerate a three-dimensional model including the inside structure of the object from a large series of two-dimensional sectional slices. According to requirement on revision, mesh on the geometry could be performed after some measures to smooth the geometry. So far a numerical version of the sample's geometry had been provided and could be combined with material property, loading condition, interaction and so on to perform further analyse.

A mini *in situ* compression setup can be placed on the holder to perform uniaxial test. The CT Scan could be started as soon as the uniaxial test is being performed. This compression setup was specially made to be versatile and adaptable for mounting within X-ray CT system. It can apply loads ranging up to 3000N. Its wall is made of vitreous glassy carbon, which allows X-Ray to pass through without any distortion.

The mini *in situ* compression setup is composed by two parts, a base and a cover. The particle was put on the base and the cover was then fixed onto the base. Then the targeted displacement or load is applied. (Fig II-5).

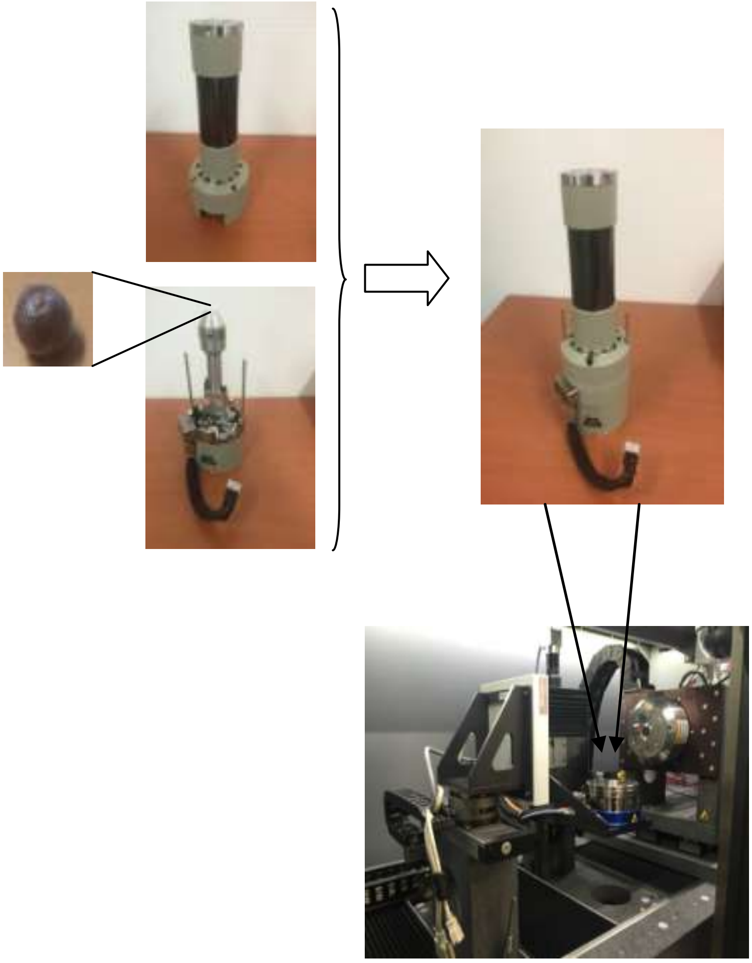

Fig II-5 Set of loading equipment for CT test

II.3.Numerical investigation

II.3.1.Overview of the material model

Numerical calculations were carried out to study the fracture mechanism of particle with the environment of ABAQUS/Explicit.

The concrete damaged plasticity model was used for all models. The concrete damaged plasticity is available both in Abaqus/Standard and Abaqus/Explicit. This model is designed for modelling concrete and other quasi-brittle material in all types of structures under monotonic, dynamic or/and cyclic loading. The model consists of the combination of non-associated multi-hardening plasticity and isotropic damaged elasticity to describe the irreversible damage that occurs during the fracturing process. It is assumed that the total strain is composed by an elastic part and a plastic part. Both of the two parts could exist isolate or separately. The elastic part of the strain can be computed from a linear elastic model.

The model assumes that the uniaxial behavior of material is characterized by damaged plasticity as shown in Fig II-6.

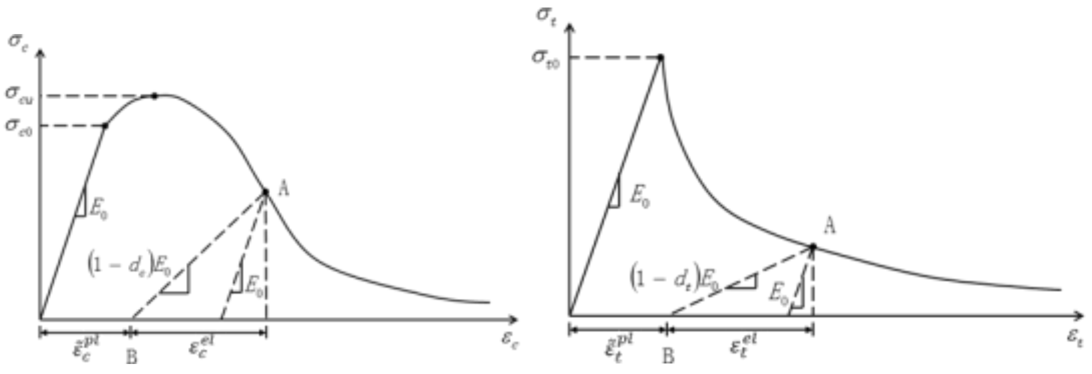

(a) Curve of uniaxial compression loading (b) Curve of uniaxial tension loading

Fig II-6 Strain-stress curve of material under uniaxial loading in Concrete Damaged Plasticity model

Under uniaxial tension loading, the strain-stress relationship follows a linear elastic model until the step of failure stress, σ_{t0} when cracks start to appear on the material. For uniaxial compression loading, the strain-stress response also follows a linear elastic relationship until initial yield stress, σ_{c0} when the stress hardening starts and the stress continue increases until the ultimate stress, σ_{cu}.

The factor *d* describes the degree of material damage and ranges from 0 to 1. In concrete damage plasticity model, *d* is defined by a separation of d_c in a compression zone and d_t in a tension zone. The two main failure mechanisms used in the model are cracking in tension and crushing in compression. The tensile and compressive equivalent plastic strains, are linked to failure mechanisms under tension and compression loading. The two variables used to define failure are $\tilde{\varepsilon}_t^{pl}$ and $\tilde{\varepsilon}_c^{pl}$ whose name are equivalent plastic tension strain and equivalent plastic compression strain If E_0 is set as the initial elastic modulus of the material, the strain-stress relations of the material under uniaxial tension or compression tests could be described as

$$\sigma_t = (1 - d_t)E_0(\varepsilon_t - \tilde{\varepsilon}_t^{pl}) \quad \text{II-3}$$

$$\sigma_c = (1 - d_c)E_0(\varepsilon_c - \tilde{\varepsilon}_c^{pl}) \quad \text{II-4}$$

Effective tensile and compressive stresses are defined as

$$\bar{\sigma}_t = {\sigma_t}/{(1-d_t)} = E_0(\varepsilon_t - \tilde{\varepsilon}_t^{pl}) \qquad \text{II-5}$$

$$\bar{\sigma}_c = {\sigma_c}/{(1-d_c)} = E_0(\varepsilon_c - \tilde{\varepsilon}_c^{pl}) \qquad \text{II-6}$$

When d equals to 0, there would be no damage and the effective stress $\bar{\sigma}$ equals to the stress σ.

The above relation could be expanded to multiaxial loading. As for the multiaxial behavior, the stress-strain relations for three-dimensional multiaxial condition are given by

$$\boldsymbol{\sigma} = (1-d)\boldsymbol{E}_0^{el}:(\boldsymbol{\varepsilon} - \boldsymbol{\varepsilon}^{pl}) \qquad \text{II-7}$$

$$\bar{\boldsymbol{\sigma}} = {\boldsymbol{\sigma}}/{(1-d)} = \boldsymbol{E}_0^{el}:(\boldsymbol{\varepsilon} - \boldsymbol{\varepsilon}^{pl}) \qquad \text{II-8}$$

in which $\boldsymbol{E}_0^{el}$ is the undamaged elasticity matrix, $\boldsymbol{\sigma}$ is the Cauchy stress tensor and $\bar{\boldsymbol{\sigma}}$ is the effective stress.

The model uses a yield function proposed by Lubliner [136]and [137]

$$F(\bar{\boldsymbol{\sigma}}, \tilde{\boldsymbol{\varepsilon}}^{pl}) = \frac{1}{1-\alpha}(\bar{q} - 3\alpha\bar{p} + \beta(\tilde{\boldsymbol{\varepsilon}}^{pl})\langle\hat{\bar{\sigma}}_{max}\rangle - \gamma\langle-\hat{\bar{\sigma}}_{max}\rangle) - \bar{\sigma}_c(\tilde{\varepsilon}_c^{pl}) = 0 \qquad \text{II-9}$$

Where $\bar{p}$ is the effective hydrostatic pressure and $\bar{q}$ is the Mises equivalent effective stress, $\hat{\bar{\sigma}}_{max}$ is the algebraically maximum eigenvalue of $\bar{\boldsymbol{\sigma}}$. The function $\beta(\tilde{\boldsymbol{\varepsilon}}^{pl})$ is given as

$$\beta(\tilde{\boldsymbol{\varepsilon}}^{pl}) = \frac{\bar{\sigma}_c(\tilde{\varepsilon}_c^{pl})}{\bar{\sigma}_t(\tilde{\varepsilon}_t^{pl})}(1-\alpha) - (1+\alpha) \qquad \text{II-10}$$

α and γ are two dimensionless material constants.

$$\alpha = \frac{\sigma_{b0} - \sigma_{c0}}{2\sigma_{b0} - \sigma_{c0}} \qquad \text{II-11}$$

where σ_{b0} and σ_{c0} means the initial equibiaxial and uniaxial compressive yield stress.

If K_c is equal to the ratio of the second stress invariant on the tensile meridian $\bar{q}(TM)$ over the second stress invariant on the compressive meridian $\bar{q}(CM)$, then

$$\gamma = \frac{3(1-K_c)}{2K_c-1} \qquad \text{II-12}$$

The yield surfaces in the deviatoric plane with different values of K_c are shown in Fig II-7 in which S_1 S_2 S_3 are projections of three axes of σ_1 σ_2 and σ_3 to the deviatoric plane.

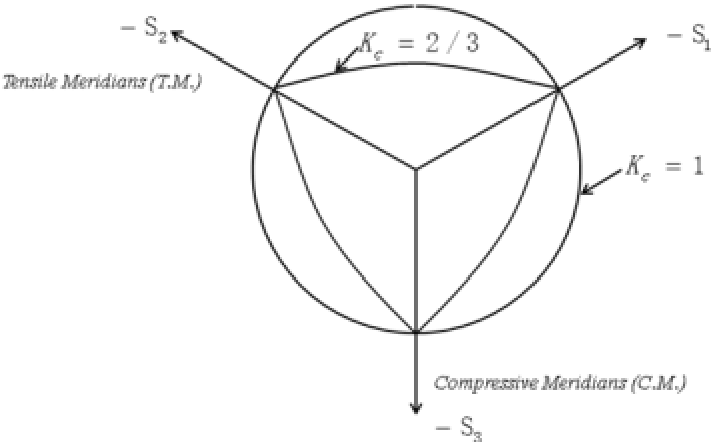

Fig II-7 Yield surfaces in the deviatoric with different value of K_c

As for the flow rule which describes the direction of plastic strain increment after yield, the flow potential G for the model is the Drucker-Prager hyperbolic function.

$$G = \sqrt{(\epsilon\sigma_{t0}tan\varphi)^2 + \bar{q}^2} - \bar{p}tan\varphi \qquad \text{II-13}$$

Where φ is the dilation angle at high confining pressure and ϵ is a parameter representing eccentricity.

II.3.2.Introduction of the geometry and physical model

Two sets of simulations were conducted to investigate single particle breakage behavior.

a.Set 1

In set 1, three models were built to simulate uniaxial compression tests and compare with the laboratory test.

The first two models, represents an ideal sphere undertaking uniaxial compression on vertical direction.

In Model 1-1, a 3D sphere with homogeneous material properties whose radius equals to 8mm was set to simulate the particle. Two analytical rigid plates were set on the top and bottom to simulate the loading platform of mechanical testing machine. To satisfy the quasi-static conditions, a downward velocity of 0.005mm/s was assigned to the top rigid plate while the bottom one was fixed. Two hard contacts without friction were set on the contact surfaces of sphere and rigid plates. The whole process was set to simulate the displacement controlled uniaxial compression test.

Since the concrete damage plasticity model is a mesh-dependent model, the damage results are influenced by the sizes and shapes of the mesh. In order to compare the influence of different elements types and to verify that the elements used were relevant, another kind of meshes was used. The results from the ideal sphere simulation (Model 1-1 and Model 1-2) and compared to results obtained in Model 1-3, which was the more realistic particle, the geometry of which was obtained from the CT scan. The first series of simulations (Model 1-1) were done with 90114 linear hexahedral elements of type C3D8R whereas 186421 quadratic tetrahedral elements of type C3D10M were generated for the second series of simulations (Model 1-2) (Fig II-8).

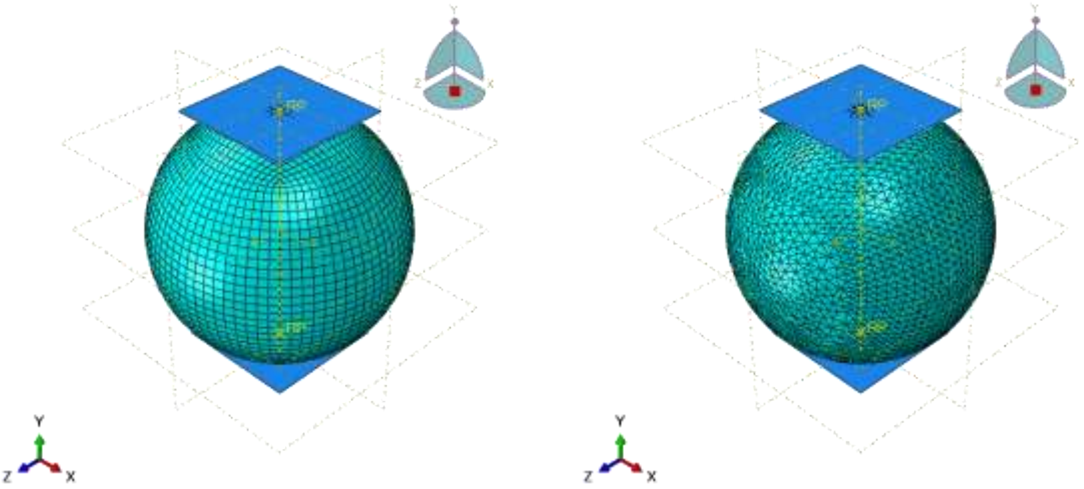

(a)Model 1-1 (b) Model 1-2

Fig II-8 Two models of the simulation

For Model 1-3, a mesh with 1152537 linear tetrahedral elements of type C3D4 were generated based on the real particle geometry from µ-CT scan. The loading conditions were similar to those imposed on Mode1 l-1 and Model 1-2. The generation process and the final shapes of the mesh will be specifically illustrated in II.4.2.

b.Set 2

For Set 2, four models were built to study the single particle’s breakage when baring loading from different directions. The different breakage orientations and locations under different tests conditions would be investigate. The 3D mesh of the particle is created based on the geometry results of CT scan. The meshes and material conditions of the particles in four models are the same with model 3 in Set 1. The only differences were the loading conditions. Several rigid plates around the particles were placed and hard contacts without friction were set to simulate the loading system. The numbers, locations and angles of the plates of the four models were different. The vertical direction is defined as y axis. For all the models, the initial contact points at the particle with the rigid plates are on the *x-o-y* plane. All the rigid plates were located on the tangent planes of their contacting points of the particle. For model 2-1, the two rigid plates were placed horizontally on the top and bottom of the particle. For the other 3 models, except for a pair of rigid plates were placed like Model 2-1, two more rigid plates were set at different location with different angle. For model 2-2, two rigid plates were placed on the left and right sides of the particle. For model 2-3, two rigid plates had an angel of 45^o between the horizontal planes and were set at the upper-left and upper-right of the particle. For model 2-4, two rigid plates had an angel of 45^o between the horizontal planes and were set at the upper-left and lower-right of the particle.

In every test, for the pair of rigid plates located on the top and bottom of the particles, the loading setting had a little difference with Model 1-3 of Set 1 but the loading effects were the same. In Model 1-3 of Set 1, the lower plate was fixed and a downward velocity of 0.005mm/s was applied on the upper one. The reason of setting so is to keep consistent with laboratory uniaxial test. However in Set 2, two velocities of 0.0025mm/s were applied on the rigid plates on top and bottom toward the centre of the particle. Since the low speeding load, the wholes tests could be treated as quasi-static conditions. The change would not make differences on the mechanical responses. However the advantage of setting so is to minimize the displacement of the centre of the particle and further ensure the loading direction of other rigid plates toward the centre (Fig II-9). But in the analysis process, in order to control variables and reflect differences, the bottom rigid plates would be set as a reference. In other word, in the part of analysis, all the displacements are the relative displacements to the lower rigid plates. The displacement and load on the vertical direction and other directions are given a name principle or secondary displacement and load, respectively.

For a single particle, the number of contacts is also called coordination number [21]. So in our tests, the coordination number of Model 2-1 is 2 and the coordination numbers of other models are 4.

The material parameters of concrete damaged plasticity model in both Set 1 and Set 2 are presented in Table II-2.

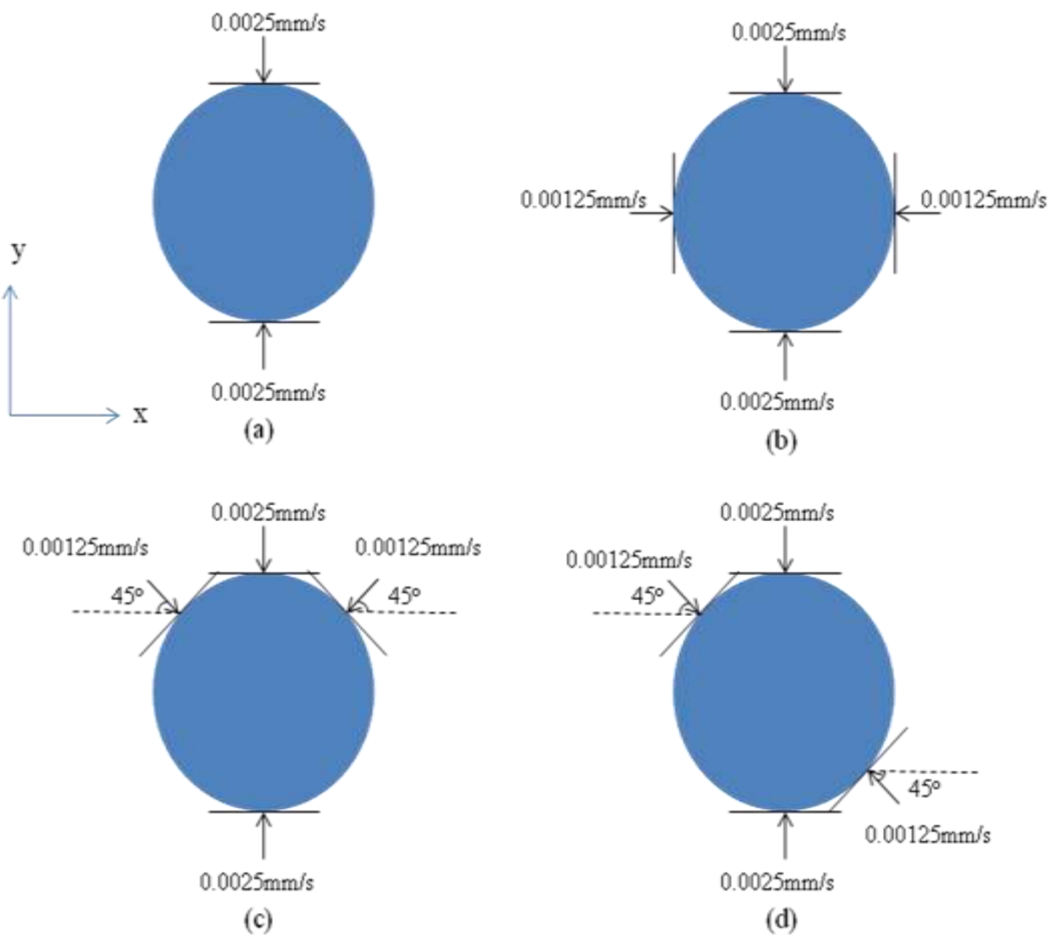

Fig II-9 The sketch of 4 models in Set two on *x-o-y* plane

(a)Model 2-1 (b) Model 2-2 (c) Model 2-3 (d) Model 2-4

Dilation angle(°)	Eccentricity	f_{b0}/f_{c0}	K_c
38	0.1	1,12	0,666
Viscosity Parameter	Density(g/mm^3)	Young's modulus(MPa)	Poisson's ratio
0	2,4	430	0,19
Compressive Behavior		Compression Damage	
yield stress(MPa)	inelastic strain	damage parameter	inelastic strain
10,056	0,000	0,000	0,000
13,408	0,002	0,000	0,002
20,112	0,002	0,000	0,002
26,816	0,004	0,000	0,004
33,520	0,018	0,000	0,018
26,816	0,061	0,195	0,061
13,408	0,136	0,596	0,136
3,352	0,282	0,895	0,282
Tensile Behavior		Tension Damage	
yield stress(MPa)	inelastic strain	damage parameter	inelastic strain
1,341	0,000	0,000	0,000

2,011	0,001	0,000	0,001
1,341	0,004	0,406	0,004
0,670	0,007	0,696	0,007
0,134	0,016	0,920	0,016
0,040	0,026	0,980	0,026

Table II-2 material parameters of concrete damaged plasticity model

II.4.Experimental results and discussions

II.4.1.Uniaxial tests

Load-displacement curves of four laboratory tests are shown in Fig II-10.

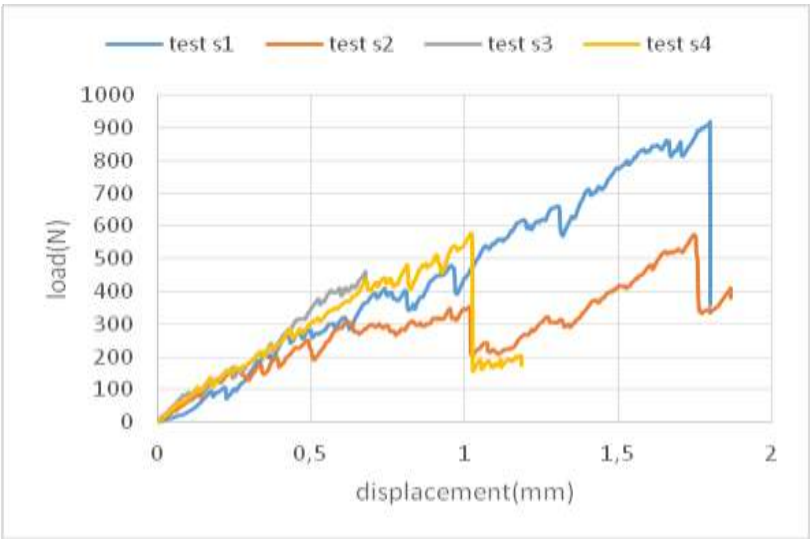

Fig II-10 Displacement-load information of single particle tests

Photos were taken at every stage of the tests. Some photos at certain time node are shown in Table II-3 with the corresponding load and displacement. According to the photos, two failure modes were observed during the tests. The first mode was located on contacting zones at the top and bottom of the particle and was initiated from the beginning to the end of loading. When the test began, the top and bottom parts of the particle started to be crushed and thus two circular plates were generated. As the test continued, the areas of the circular plates grew throughout the test. This mode of failure would lead to a volume decrease of the particle but the particle still had baring capacity. The second mode was a global failure initiated from a crack which appeared after the test started for a while. This kind of failure would separate the particle to several parts and make the particle lose baring compressive capacity. The detailed location of the cracks could not be predicted but the crack must be a vertical one whose path could path through the top, the centre, and the bottom of the particle. Before the vertical crack appearing, the force-displacement curve increases linearly then a sudden force drop is observed when the crack appeared. During curve increasing, some small fluctuations are observed. This phenomenon indicates that some local failure occurred before the final global failure. The vertical crack can thus be regarded as a brittle crack. For some of the particles, one vertical crack appeared during the test such as test S_1, S_3, S_4 while for S_2, two vertical cracks appeared.

It could be observed that the appearances of the global failure of the four tests differed a lot. It is because the distribution and number of voids could make a hue influence to the global behavior. Moreover, the local failure because of the imperfect geometry could also lead to a development of the micro-structure and finally influence the global behavior. Thus, μ-CT tests were performed to investigate the inner geometry of the particles.

S_1	Photo				
	Load(N)	1.255	149.5	316.7	918.7
	Displacement(mm)	0.005	0.300	0.600	1.081
S_2	Photo	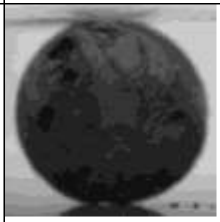	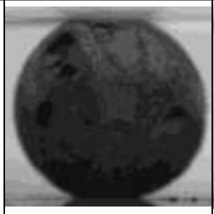	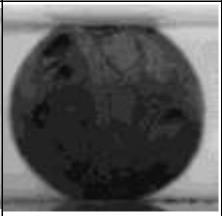	
	Load(N)	1.929	222.8	396.2	573.2
	Displacement(mm)	0.002	0.500	1.019	1.743
S_3	Photo				
	Load(N)	3.064	125.6	253.78	450.7
	Displacement(mm)	0.003	0.201	0.401	0.677
S_4	Photo	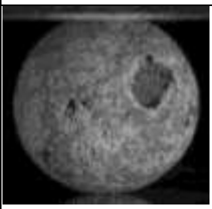	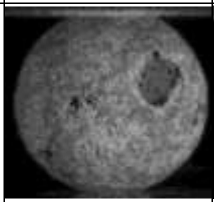	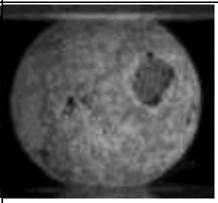	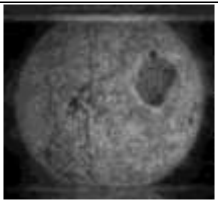
	Load(N)	1.283	183.1	360.1	583.5
	Displacement(mm)	0.002	0.302	0.601	1.032

Table II-3 Breakage information of each single particle test

II.4.2.CT scan analysis

One of the goals of the post-scan processing stage was to create a 3D tetrahedron mesh representing the real 3D geometry of the particle. At a first step, 895 projections of different angles were imported into X-ACT®, the bundled software associated with the CT apparatus. 1022 images representing 2D tomography slices of particle with a resolution of 14.9944*14.9944 μm^2 were produced and imported into Avizo®, a 3D visualization and analysis software. Afterwards, a filter was applied to make a primary smoothing. Since the particle material and voids have different greyscales, segmentation was conducted to distinguish the material and voids of each particle. Then, the particle geometry needs to be simplified to decrease the computational cost of the numerical simulation. A lot of small isolate points called island were removed and several tiny holes were filled. The boundaries of the particle were then smoothed. Surface of the particle and the mesh were then generated. Post-scan process of CT test is shown in Fig II-11. A comparison between a radiograph projection and a tomography slice is shown in Fig II-12. A section of the particle is recorded to show the differences after each step of post-scan (Fig II-13). Finally, a 3D mesh with 1152537 linear tetrahedral elements of C3D4 type is generated and imported in Abaqus® for further simulation (Fig II-14). A μ-CT slice of the particle after failure is presented in Fig II-15.

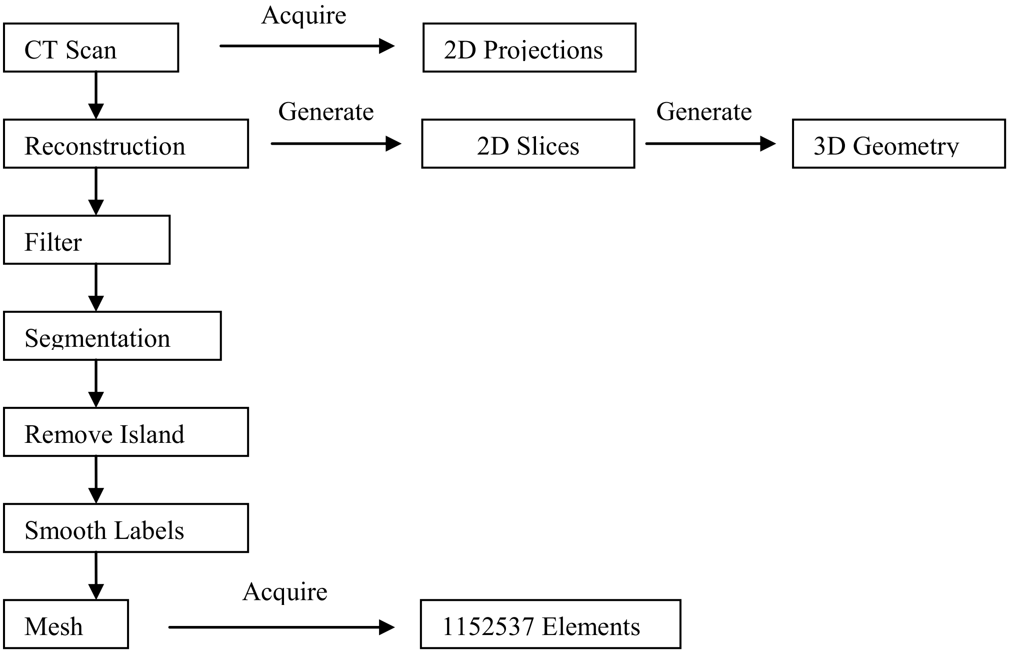

Fig II-11 Post-scan process of CT test

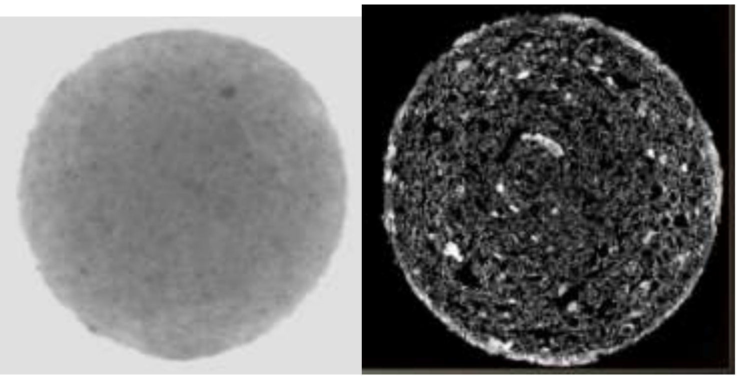

(a) a radiograph projection (b) a tomography slice

Fig II-12 Images of a radiograph projection and a tomography slice

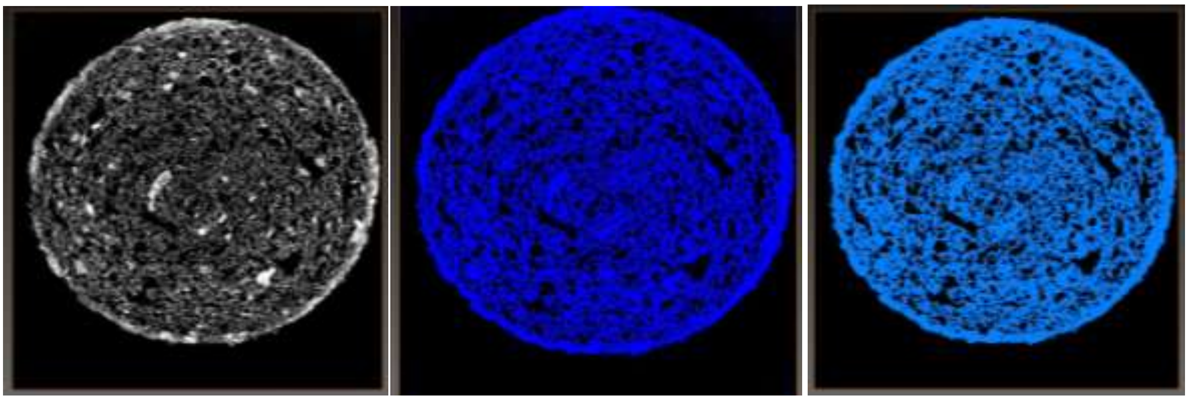

(a) after filter (b) after segmentation (c)after Remove Island

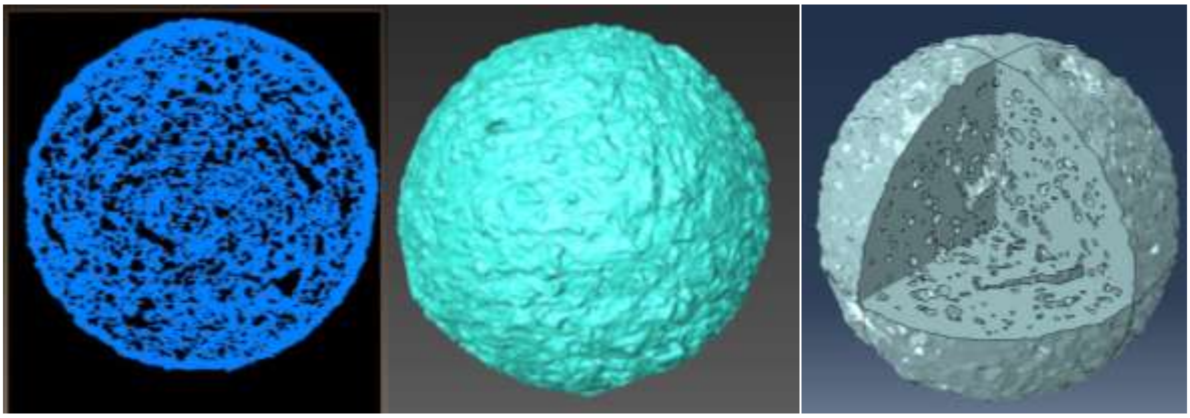

(d)after "Smooth Labels" (e) surface of the particle (f) voids of the particle

Fig II-13 Post-scan processing of computed tomography test.

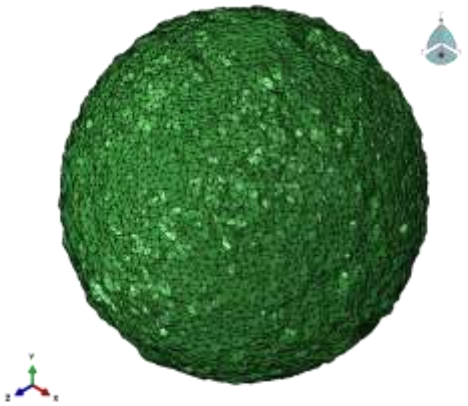

Fig II-14 3D tetrahedron mesh of the particle

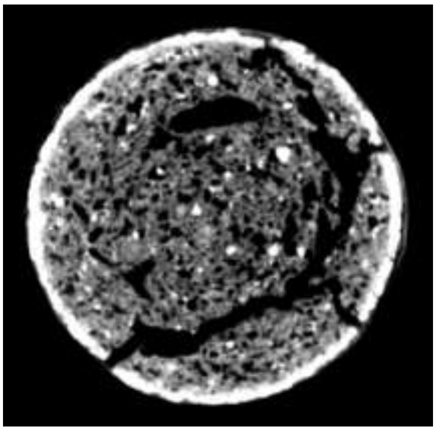

Fig II-15 One slice of the particle after failed

II.5.Numerical results and discussions of Set 1

In this part, a comparison of the results of laboratory tests and simulations would be made and the generation process and the location of the different kinds of failures will be investigated.

II.5.1.Load-displacement curve

The calculated global displacement-load curve presented in Fig II-16 is compared to the experimental results.

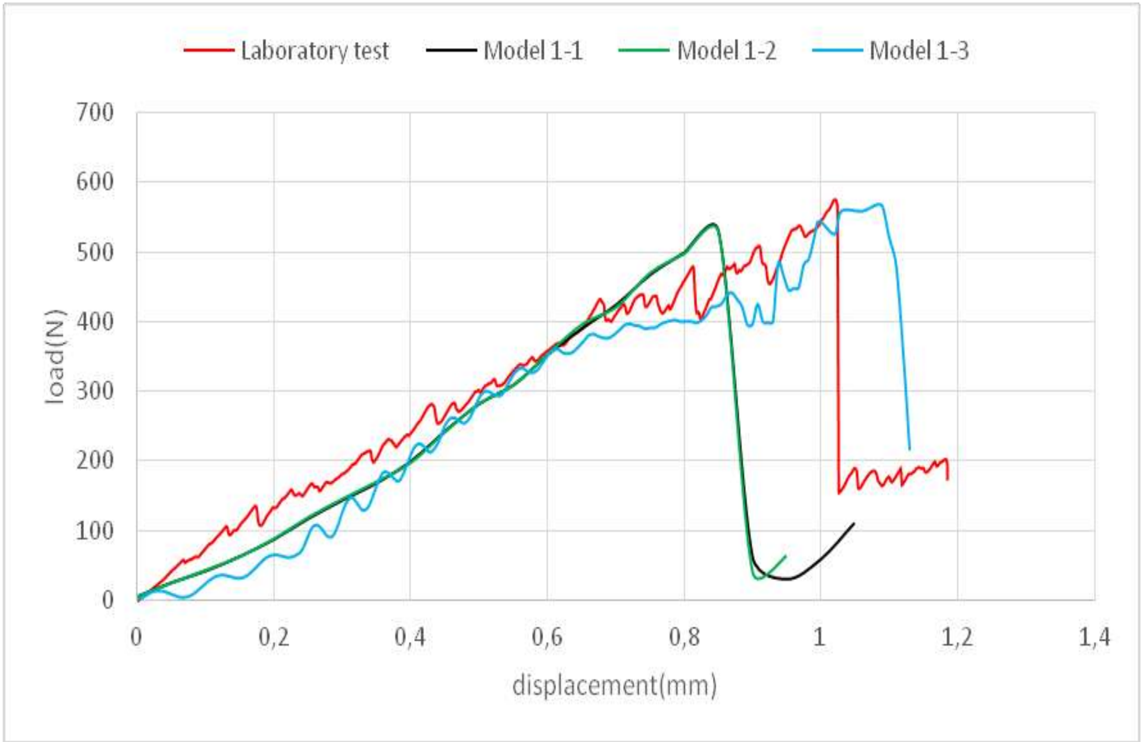

Fig II-16 Displacement-Load curve of the simulation compared with Laboratory Test

The curves obtained with Model 1-1 and Model 1-2 are almost the same. The comparison between the numerical and experimental results appears two differences. Fluctuations were more pronounced in Model 3, while in Model 1 and Model 2, the curves are almost smooth. The occurrence of failure was slightly different in simulation compared to experiments. These differences can be explained by the fact that the geometry of the particle of Model 1-3 contains a lot of voids. However, the simulated sample used in Model 1-1 and Model 1-2 is a perfect sphere without any void. The material parameters in Model 1-1 and Model 1-2 could be considered as a mean value of real material property of Laboratory test sample. The force drops observed in experimental and Model 1-3 results could be explained by the local failure of pore inside the particle.

Particle has experienced elastic and plastic deformation before failure. The Mises stress distributions during loading of Model 1-1, Model 1-2 and Model 1-3 are shown in Fig II-17, Fig II-18 and Fig II-19, respectively. In order to present results clearly, the rigid plates which exist on the top and bottom of the sphere are not displayed and cross sections are shown to show the insides behavior (similarly hereinafter and will not be explained).

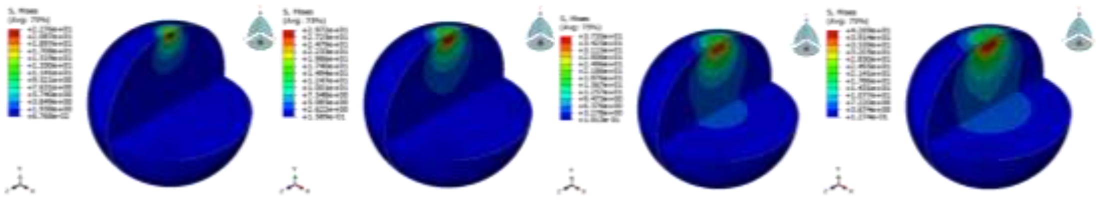

(a)Disp=0.2mm (b)Disp=0.4mm (c)Disp=0.6mm (d)Disp=0.8mm

Fig II-17 Mises stress distribution in Model 1-1 at increasing displacement

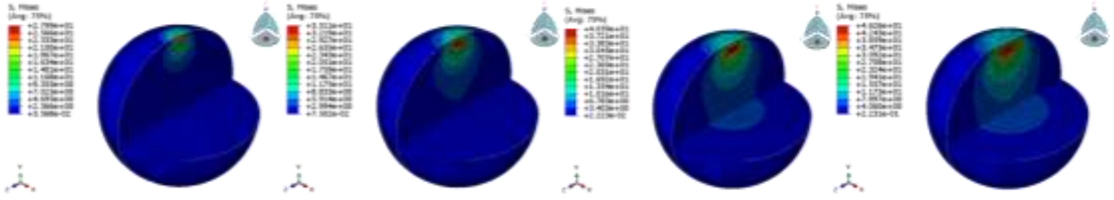

(a)Disp=0.2mm (b)Disp=0.4mm (c)Disp=0.6mm (d)Disp=0.8mm

Fig II-18 Mises stress distribution in Model 1-2 at increasing displacement

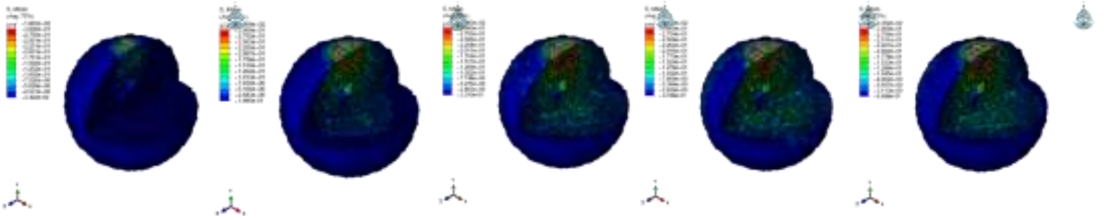

(a)Disp=0.2mm (b)Disp=0.4mm (c)Disp=0.6mm (d)Disp=0.8mm (e)Disp=1mm

Fig II-19 Mises stress distribution in Model 1-3 at increasing displacement

It is clear that the distributions of the Mises stress of the three models are almost the same. The most stressed areas are the surfaces in contact with the rigid plates. It can be observed that at every step, the maxim value of Mises stress of Model 1-2 is higher than Model 1-1. However the global forces of the two models at every step are similar. The reason is that the volumes of elements in Model 1-2 are smaller than Model 1-1. However regarding the whole sphere, the forces, which are the integration of the stresses, are still the same. For Model 1-3, the shape of the curve is not as regular as the others. This can be explained by the geometry of the outer surface of the real particle, which is not smooth and there are a lot of valleys and crests. Under loading, the top and bottom portion of the particle were compressed to a circular plate. So these valleys and crests developed stress concentration. In addition, lot of void exists inside the particle, which may cause local failures.

II.5.2.Location of the global failure

The failure patterns obtained with Model 1-1 and Model 1-2 are presented in Fig II-20 where the location of the failure can be observed. The tensile-induced damage propagated from the centre of the particle. The tensile damage expands with the loading, which in turn leads to global failure. Several vertical cracks appeared suddenly separating the particle in several pieces. The global failure of the sphere was induced by the occurrence of cracks and exhibits a brittle failure response as shown in Fig II-16.

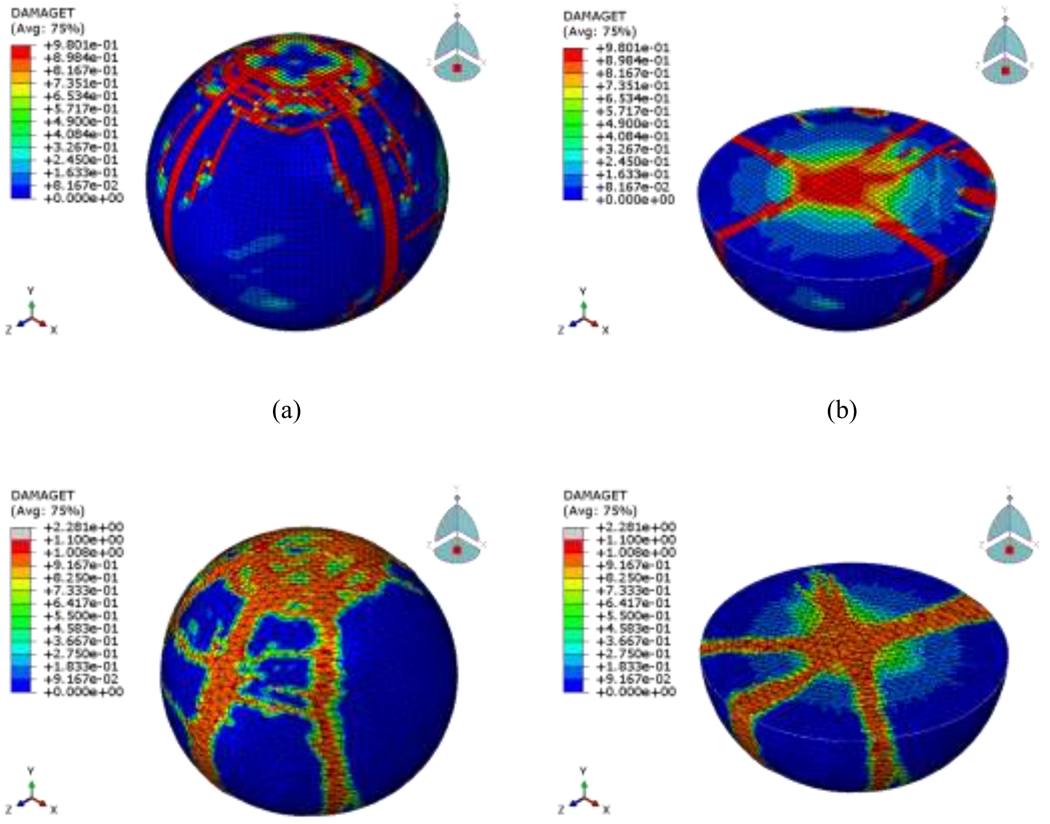

(a) (b)

(c) (d)

(a)(b) Failure state of Model 1-1. (c)(d) Failure state of Model 1-2

Fig II-20 Failure state of simulation

Due to the geometry and loading symmetry of particle in Model 1-1 and Model 1-2, four cracks located on plane containing the centre were observed. As stated above, the particles in Model 1-1 and Model 1-2 were perfect spheres whose shapes and loading conditions have symmetry around its vertical central axis (y-axis). However, the mesh elements plane had some extremely small differences leading to the position of the cracks. So crack formation is meshing dependent.

In Model 1-2, one more crack appeared and the shape and direction of cracks were not as regular as in Model 1. This result was due to the Free meshing technique adopted, which gave rise to a different element generation than with Structured meshing technique. In other words, it was more possible to have some randomly located irregular meshing property in Model 1-2. In Model 1-2, the failure location and pattern was more similar to Model 1-3 (shown in Fig II-21) than Model 1-1.

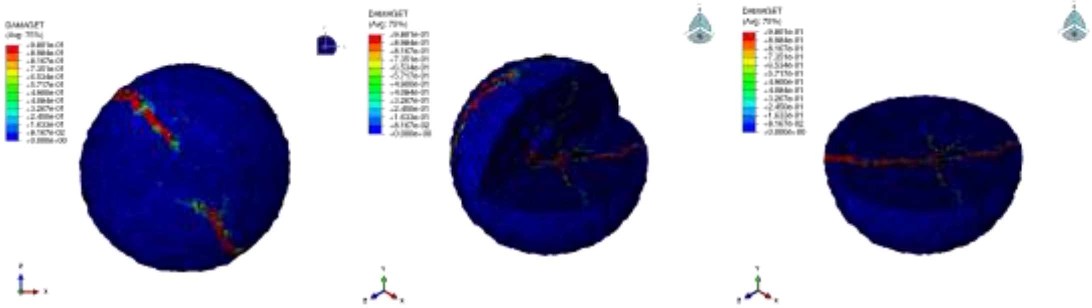

Fig II-21 Failure state of Model 1-3 from different angle of view

In Model 3, the directions of the cracks are almost vertical. This pattern was found to be closest to experimental observations. Moreover, the inner structure with randomly distributed voids controls the locations and development of cracks. Like in Model 1, four main cracks appeared but two of them were not well developed. This is also because of its imperfect structure.

II.5.3.Formation of the failure

Two types of failures could be observed during the test i.e. compression damage caused failure and tensile damage caused failure having different characteristics. The compression damage caused failure was local failure and could not cause global failure. It located on top and bottom and grew as the test was going on but stayed local failure to the end of the test. The tensile damage caused failure was a local failure initially. However, it started from the centre and developed in several vertical cracks which caused a global failure.

The evolution of the compression damage is controlled by compressive equivalent plastic strains (PEEQ in Abaqus). In order to highlight the formation of compression damage, the evolution of PEEQ has to be analysed. The results of an ideal particle and a real particle were obtained from Model 1-1 and Model 1-3, respectively.

Results obtained on the ideal sphere can be seen in Fig II-22 and Fig II-23. At the beginning of the test, the maximum value of PEEQ was located on the top and bottom of the particle. As the test went on, the value of PEEQ grew and the maximum point moved towards the centre. When the displacement was 0.2mm and 0.4mm, the PEEQ was not high enough to cause compressive failure. Finally, the zone located at about ¼th of the radiuses below the contact surface start to fail.

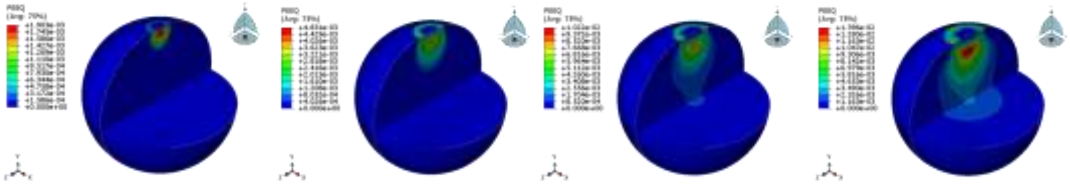
(a)Disp=0.2mm (b)Disp=0.4mm (c)Disp=0.6mm (d)Disp=0.8mm

Fig II-22 PEEQ of ideal particle at increasing displacement

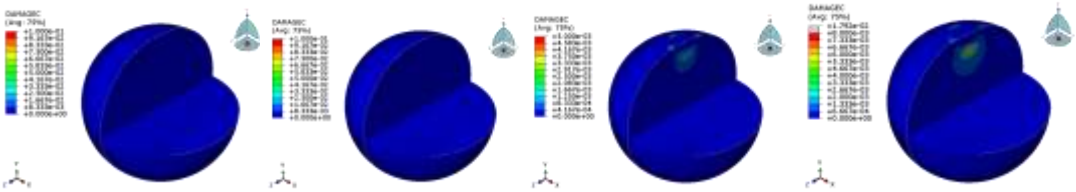
(a)Disp=0.2mm (b)Disp=0.4mm (c)Disp=0.6mm (d)Disp=0.8mm

Fig II-23 Compressive damage of ideal particle at increasing displacement

The same results can be seen in Fig II-24 and Fig II-24 concerning Model 1-3 (real particle scanned with X-Ray micro CT). Compared to ideal particle (sphere), the elements located on the surface of the particle in contact with rigid plates reached failure earlier and failed at the beginning of the test. This is due to the rough surface of the real particle. Severe stress concentration on the top and bottom surfaces had reached the limit point soon after the beginning of loading. When these crests disappeared, the same pattern was observed with an ideal particle except that the highest stress level is always close to voids.

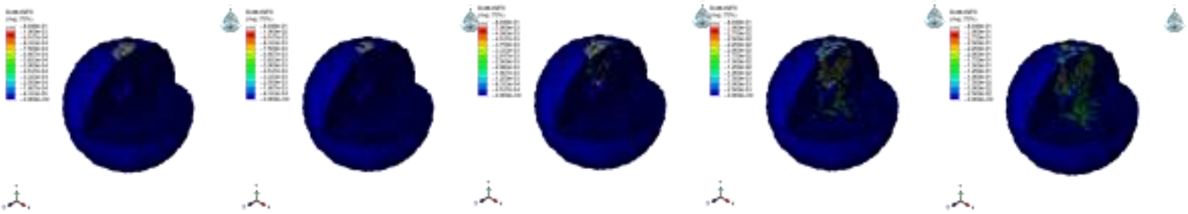
(a)Disp=0.2mm (b)Disp=0.4mm (c)Disp=0.6mm (d)Disp=0.8mm (e)Disp=1mm

Fig II-24 PEEQ of real particle at increasing displacement

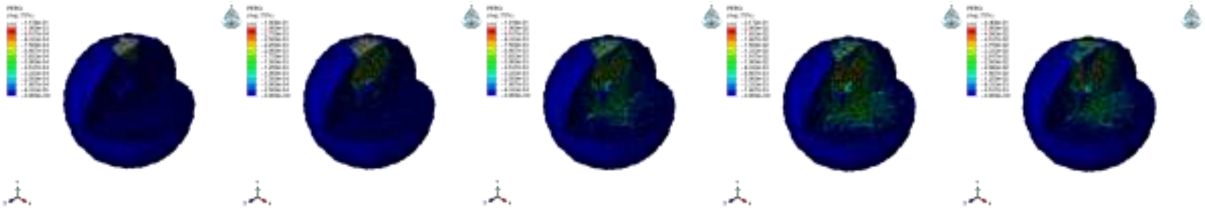
(a)Disp=0.2mm (b)Disp=0.4mm (c)Disp=0.6mm (d)Disp=0.8mm (e)Disp=1mm

Fig II-25 Compressive damage of real particle at increasing displacement

The evolution of the tensile damage is controlled by the tensile equivalent plastic strains (PEEQT in Abaqus). For the ideal particle, results are shown in Fig II-26, Fig II-27, Fig II-28 and Fig II-29

When the test had just started, it can be seen that the vertical load is diffused in two disc surface, on the top and bottom of the particle. This area grew larger as the loading progressed. At the boundary of these two surfaces, PEEQT firstly reached limit value leading to first tensile damage. The damaged zone formed a circle whose radius was growing as the tests progressed. However, at this stage, the failures caused by tensile damage did not develop to lead to a global failure.

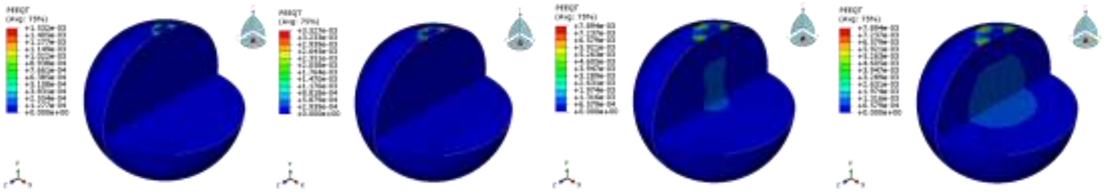
(a)Disp=0.2mm (b)Disp=0.4mm (c)Disp=0.6mm (d)Disp=0.8mm

Fig II-26 PEEQT of ideal particle at increasing displacement

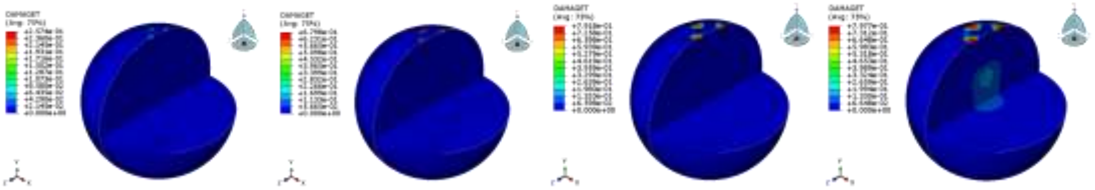
(a)Disp=0.2mm (b)Disp=0.4mm (c)Disp=0.6mm (d)Disp=0.8mm

Fig II-27 Tensile damage of ideal particle at increasing displacement

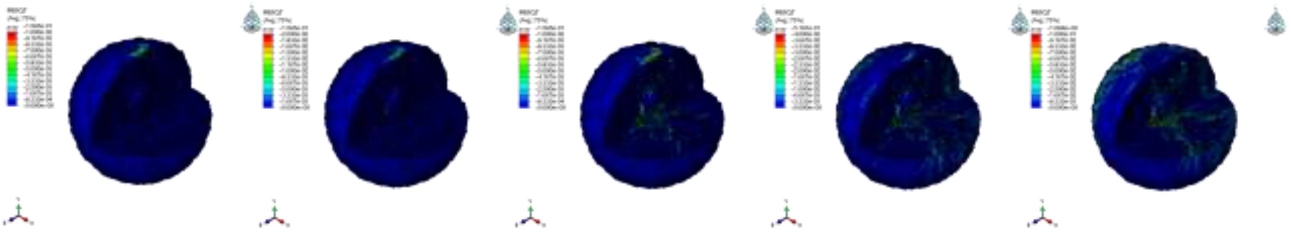

(a)Disp=0.2mm (b)Disp=0.4mm (c)Disp=0.6mm (d)Disp=0.8mm (e)Disp=1mm

Fig II-28 PEEQT of real particle at increasing displacement

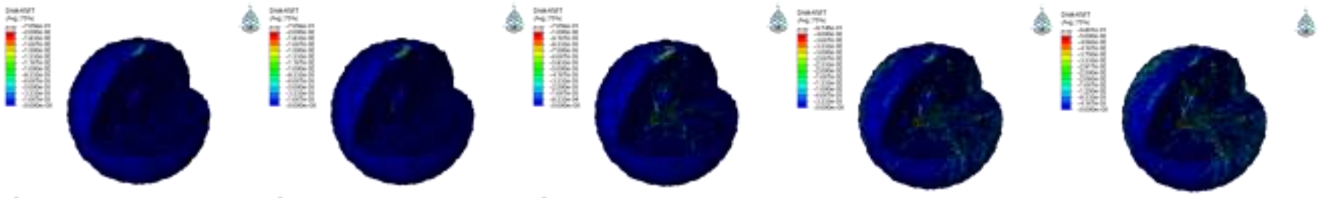

(a)Disp=0.2mm (b)Disp=0.4mm (c)Disp=0.6mm (d)Disp=0.8mm (e)Disp=1mm

Fig II-29 Tensile damage of real particle at increasing displacement

As the test went on, the PEEQT at the centre of the particle reached a value corresponding to tensile damage limit. For ideal particle, as the test continued, the damaged area became increasingly wider. Compared to Fig II-20, it can be seen that cracks appeared suddenly at any location. For real particle, the situation is different because of the internal voids results in more diffuse damage observed within the particle. Thus, when the damaged zone grew, some defect points had higher stresses because of stress concentration. Then, the PEEQT values obtained around these points increased rapidly. Finally several cracks appeared and the particle was unable to carry any load. Compared to Fig II-21 it can be found that before the cracks developed entirely, some points at the route of cracks had already failed.

In general, the failure from top and bottom of the particle appeared firstly and keep developing until the end of the test. This type of failure could cause two spherical zones beneath the contact surfaces between the particle and rigid plates. Nevertheless, these two zones could not develop to global failure. On the other hand, crack propagation, which started at the centre of the particle developed into a global failure. The failure initiated from the centre of the particle was not visible until the occurrence of global failure, which was confirmed by experiments.

II.6.Numerical results and discussion of Set 2

In II.5, the generation process and characteristic of failures are studied. In this part, the emphasis will be the difference failure behavior of particle with different coordination numbers. The failure behavior of particle under load of different directions would be also studied.

II.6.1.Load-displacement curve

The calculated principle displacement-load curve is presented in Fig II-30. The first dramatic drops in each curve are marked by circles which correspond to the occurrence of the vertical diametric cracks. This kind of cracks is global failure which appeared from the centre of the particle and is controlled by the tensile equivalent plastic strains (PEEQT in Abaqus). The forming process is similar to simulations in Set 1 so no more details would be described in this part. The vertical crack could be seen in Fig II-31.

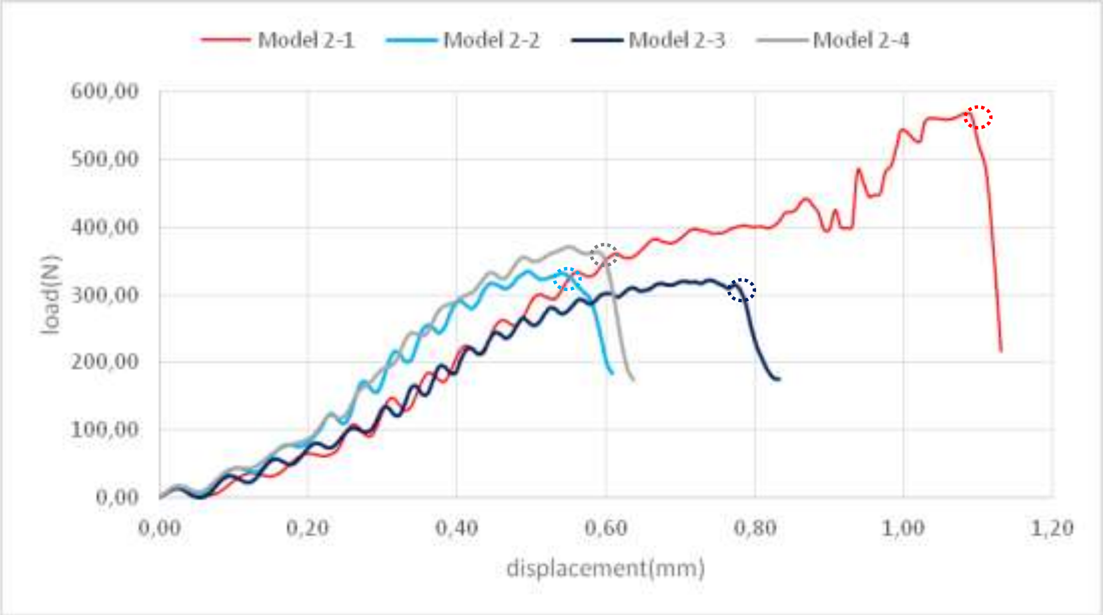

Fig II-30 Principle load-displacement curve of 4 models

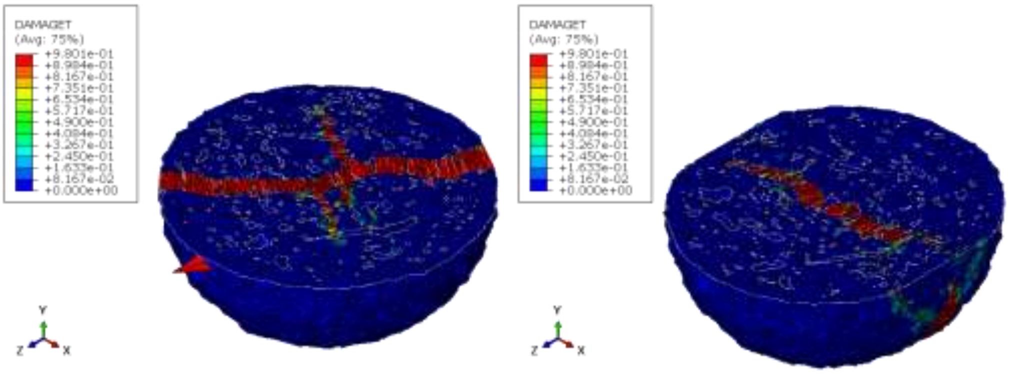

(a) Model 2-1 (b) Model 2-2

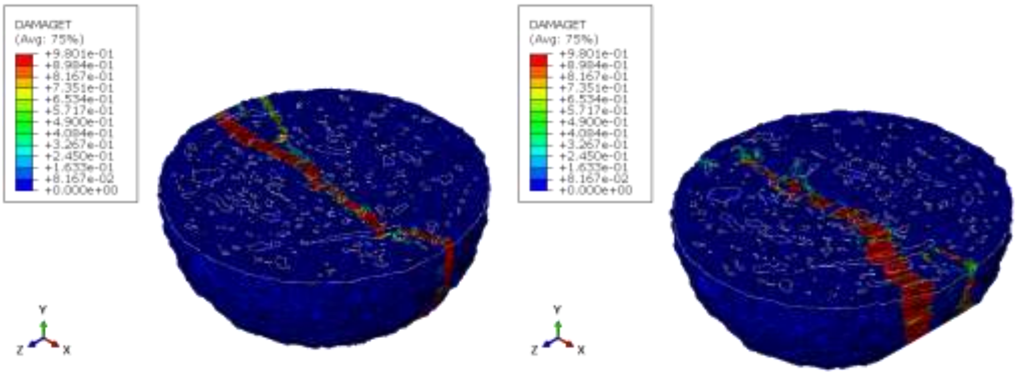

(c) Model 2-3 (d) Model 2-4

Fig II-31 The cracks of the four models

It could be observed that, the global failure on the particle with lower coordination number (Model 2-1) appeared later than the others. The PEEQT of the four models when the load-displacement curve starts dropping (marked by circles) is shown in Fig II-32. The principle loads are on the y direction. The secondary loads are on the different location of *x-o-y* plane.

It could be observed that, with different principle displacement, the PEEQT of the four tests at the centre of the particle had increased to the level which could lead to a crack. The reason is that for the particles with multiple directions of loads, the tensile equivalent plastic strains increase quickly because of the combined effect of the loads. So the global failure appears faster than the others.

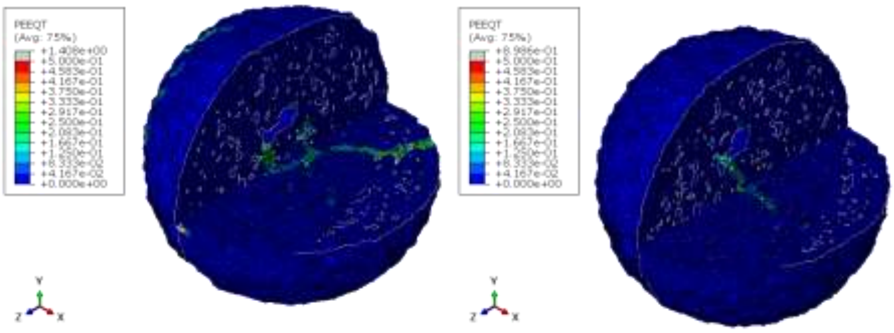

(a) Model 2-1 (b) Model 2-2

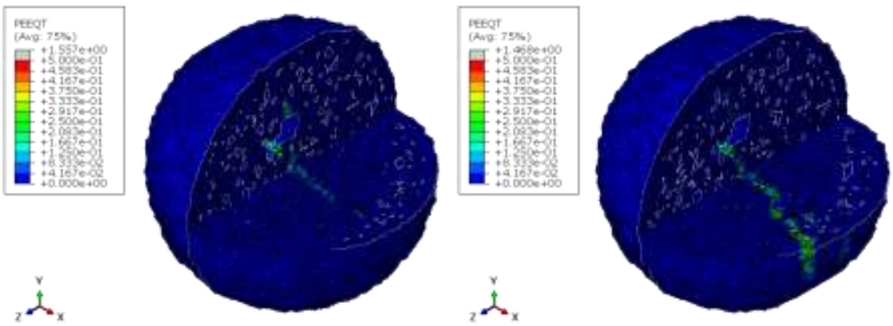

(c) Model 2-3 (d) Model 2-4

Fig II-32 The PEEQT of the four models just before cracks appeared

II.6.2.Location and numbers of the cracks in global failure

As analyzed in simulations of Set 1, when the global failure of a particle appears, several vertical cracks appeared and separated the particle into several parts. However, the number and location of cracks could not be foreseen only with the information of loading condition and external geometry. Because theoretically speaking, if the void inside the particle is spreading completely evenly, on any *z-o-x* plane, the stress and strain are central symmetrical respect to the centre. However in model 2-2, model 2-3, and model 2-4, only one crack through the certer separates each particle into two parts. Moreover, the crack developed along the *x-o-y* plane approximately. The reason is that baring loads from multiple directions on *x-o-y* plane, on any *z-o-x* plane, the maximum tensile stress located on *x* axis approximately.

For a spherical particle of compression load, some elements may carry tensile stress which could determine the appearance of the crack. The location where elements have biggest tensile strain could determine the location of the crack and the direction of the tensile stress on such elements could determine the direction of the crack. The logarithmic max principle strain on the *z-o-x* plane before the crack appeared could be seen on Fig II-33. It could be observed that, in model 1, the max value is on the centre of the particle and spread to the surface almost evenly. But for model 2-2, model 2-3 and model 2-4, the max value is also on the centre of the particle but the spreading trace composed a distinct band along the x-axis which separates the particle to two parts.

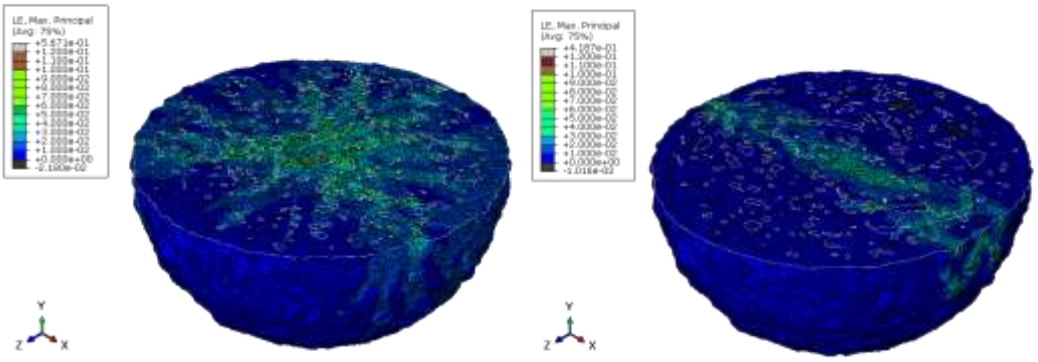

(a) Model 2-1 (b) Model 2-2

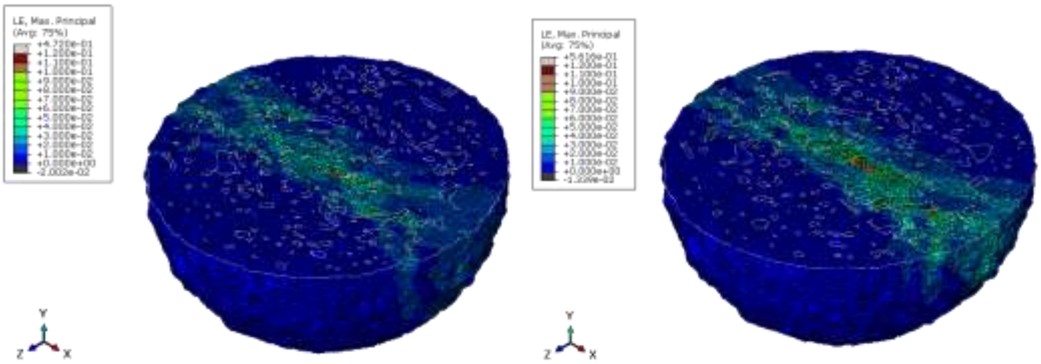

(c) Model 2-3 (d) Model 2-4

Fig II-33 The logarithmic max principle strain on the *z-o-x* plane before the crack appeared

The direction of tensile stress on such elements is perpendicular to the direction of the compression stress. When under uniaxial load on vertical direction, the normal stress states of elements are shown in Fig II-34(a). Except for compression stress on y direction, it has tensile stress on x and z direction. Thus, when the load reaches a critical value, the crack planes must be parallel to y axis and its detailed location is determined by the detailed material stiffness on the elements. However for model 2-2, model 2-3 and model 2-4, the particles were compressed on *x-o-y* plane. The normal stress state of elements is shown in Fig II-34(b). Therefore, the crack planes for these three models must be parallel to y axis and x axis. So the crack plane is approximately following the *x-o-y* plane and there would be a slight deviation because of incompletely even geometry of the particle.

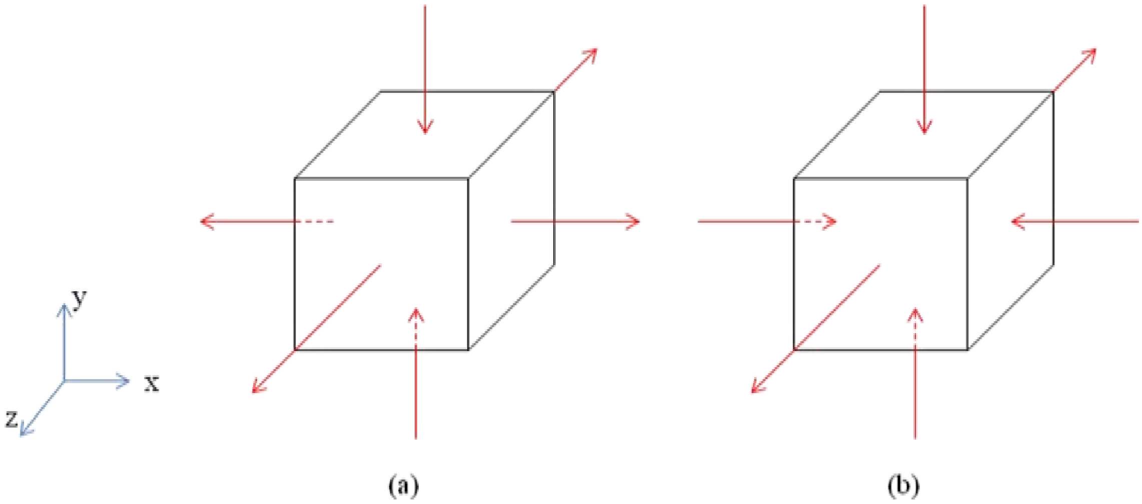

Fig II-34 The normal stress state of elements

(a): Model 2-1 (b): Model 2-2 Model 2-3 and Model 2-4

II.7.Summary

Some uniaxial compression tests on single particles have been developed. X-ray Computed Tomography technology was used to capture the inner structure of a particle. The reconstructed 3D geometry of particle was imported into Abaqus to build a 3D model of a real particle. The results from the real particle are compared to the results from it an ideal particle.

The observed failures patterns of a spherical particle could be divided into two categories according where the crack first developed namely failure from top and bottom and failure from the centre.

When the particle failed from at top and bottom, it appeared from the beginning of the test. This type of failure could lead to the generation of two circular planes and is caused by tensile damage and compression damage. The tensile damage locates on the boundary of the circular plane from the beginning of the test. However, the appearance time and location of compression damage is according to whether the particle is an ideal sphere or not. The compression damage appears when and where the compression equivalent plastic strain (PEEQ) reaches a certain value. If the particle is an ideal sphere, it appears at about ¼th of the radiuses below the contact surface with the loading machine. Nevertheless, if the particle is not an ideal sphere, stress concentration caused by some defects may cause the PEEQ reaches the limit value in advance. Even, if there are some sharp protuberances at the surface of the particle, the compression damage may appear at the beginning of the test.

For the second type of the failure, cracks develop right at the centre if the particle is a perfect sphere and close to the centre if it is not. This type of failure is caused by tensile damage. When the tensile equivalent plastic strain reaches the limit value, the failure appears and then it grew larger gradually with the deformation of the particle. This process could not be observed from outside of the particle until when the zone of the tensile damage reaches a certain volume when some vertical cracks appear suddenly and separate the particle to several parts.

For the failure from the top and bottom, it is a local failure from the beginning to the end. However for the failure from the centre, it is a local failure when it appears and develops gradually but finally it could lead to a global failure.

If the particle has bigger coordination number, the global failure occurs more quickly because the complex loading environment could make the PEEQT at the centre of the particle increasing faster.

The crack plane which caused a global failure must bypass the centre of the particle and must be parallel to the direction of loading. Thus for the particle only bare load from vertical direction, it is impossible to foresee the direction of the crack plane only with the testing condition. It is also possible that there are several crack planes to separate the particle to several parts. But for the particle baring load from more than one direction like Model 2-2, Model 2-3, Model 2-4 in Set 2, the direction of the crack plane could be curtained and there would be only one crack plane.

Chapter III. Packing of Spherical Particles under Continuous Biaxial Loading

III.1.Introduction

III.1.1.Research background

It is well known that the mechanical behaviour of granular material is strongly affected by the relative arrangement of voids and particles. The study of packing of granular material has started in 1929 by Furnas [8]. Fabric of granular material could be used to identify the arrangement of particles and voids [13] [53]. Precisely, with a statistical study, Oda [55] introduced a method to measure the fabric of a random assembly of spherical granular such as density of contacts, average branch length, second-order symmetric tensor and so on. Coordination number, radial distribution function and packing density are the most commonly used and fundamental parameters to characterize a structure of a granular material in Discrete Element Modelling [57] [58]. The coordination number was first used in chemistry in 1893 by Alfred Werner. The coordination number of a central atom in a molecule or crystal is the number of its near neighbours [57]. For granular material, the coordination number means the average number of particles in contact with a given one. The detailed calculating methods of the coordination number were introduced by Jouannot-Chesney[58]. The packing density means the volume fraction of the space dominated by particles. Lochmann et al [61] who studied the relationship between packing density and radial distribution function.

Since 1971, some researchers started to study the mechanical properties of granular material composed by more than one material using mathematical method [138]. Wang [139] performed numerical simulation of two set of spherical particles to study the impact energy decay inside the composite granular arrangement.

For some authors, the particle shape is one of the most important variables in the packing process. They focused on some shapes of particles, e.g., spheres [61], ellipsoids [68] and regular convex polyhedral [69] to study packing characteristic and performed experimental tests. As is known to all, operating laboratory tests are expensive and difficult. Moreover, more microscopic information could be obtained with numerical simulation, which provides more data to analyze for a better understanding. Thus, several available numerical methods were adopted such as Monte Carlo simulation [75], the Lubachevsky-Stillinger algorithm [140], molecular dynamics [141], and the discrete element method (DEM)[141].

The influence of the diameter of particles was also studied. It is found that, for monosized and polysized particles, the mechanical behaviour of granular material showed major differences [74] [76]. Some scientists were interested in the angular distribution of the contact directions [80]. The concept of anisotropy was studied and the method for description of granular texture with anisotropy was used [61]. Some authors used the concept of critical state to study the evolution of packing density and coordination number. They believed that critical coordination number and critical anisotropy should be a combination that describes critical state. [87] [90].

From all the literatures above, it could be found that numerous research works have been done to study the static packing of granular material. However the study on the packing of granular material when influenced by loading is still lacking. In this chapter, biaxial compression tests on granular material of monosized and polysized particles were performed. During the tests, photos were taken to record the morphology at every stages of the tests. Packing of the granular material through the process of the test was therefore been analyzed.

III.1.2.Aim and objectives

The aim of this chapter is to study the fabric of packing of multiple spherical particles made by porous heterogeneous material when disturbed by vertical load. Therefore, a series of experimental biaxial compression tests have been performed. With the photos which recorded every state (2 photos per second) of the tests, software written by MATLAB code is used to analyse the results.

This chapter is organized with five parts which addressing different contents. References among parts could guide the reader to focus on specific topics. In part 2, the experimental apparatus and methodologies are described. The analytical method is introduced. In part 3, the experimental setting is displayed. In part 4, the experimental results are analyzed. In part 5, a conclusion summarizes the main results.

III.2.Experimental apparatus and analyze methodologies

III.2.1.Sample properties

Particles made by light expanded clays which were used in laboratory tests of Chapter 2 were used in the biaxial compression apparatus. All the particles are approximating spherical whose outside surfaces are rugged. This material can be defined as porous and heterogeneous with a very low density due to existing randomly distributed voids within each particle. The mean density of particles which was obtained from measure on 12 randomly chosen individual particles is 1.241. The original grain size distribution (GSD) of the sample is shown in Fig III-1. During the tests, samples of different particle sizes were studied. In Fig III-1, it could be easily seen that there are some small components which could be regarded as dust. These components could not make any contribution to the mechanical behavior the assembly and may make the experimental apparatus unclean which has great disadvantage on observation of the tests. In order to prevent this potential problem, the samples were cleaned before all tests with compressed air to eliminate the above-mentioned tiny elements.

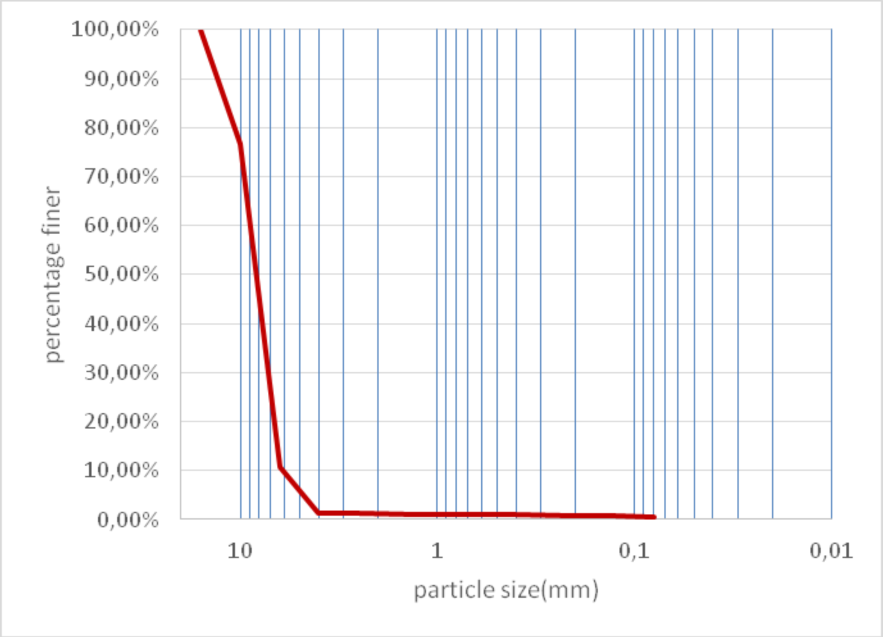

Fig III-1 Original GSD line of the samples

III.2.2.Experimental apparatus

During the tests, particles are placed in a container before baring compression. Thus a Plane Strain Chamber (PSC) which is composed by several Polymethyl Methacrylate (PMMA) sheets and fixed by several bolts is set up. The front surface, the back surface and the bottom surface of the PSC are considered as completely fixed and rigid. On the left and right surfaces of the PSC, PMMA sheets are set like the front and back ones but water bags are introduced and linked to pressure controllers to apply lateral pressure. The theoretical maximum capacity of the chamber is about 130mm*64mm*150mm (Length*Width*Height). The theoretical length and height are fixed but the width can be changed following the tests. During the tests, the actual length of the sample evolves because of the volume modification of the water bags which provide lateral pressure. In this case, a constant lateral pressure is laterally applied. It should be noticed that rigid covers can be introduced to apply a constant vertical displacement. The top of the PSC is composed of three PMMA elements. The side ones are sealed with the walls of the chamber. However the mid one, called cover of the PSC, is vertically movable and is contacted to the loading system. When the loading system starts to apply load, the cover moves downward to transmit the load to the assembly of particles. In order to provide different loading conditions, covers with different sizes are produced. Correspondingly, the topsides PMMA sheets of different sizes are also produced to match with the sizes of the cover. The lengths of the small cover and the large one are 70mm and 150mm, respectively. All the components and combinations of the two kinds of PSC are shown in Fig III-2. The detailed measures of the PSC could be seen in the three views of the two type of PSC which are displayed in Fig III-3 and Fig III-4. In order to make the main body of the PSC clear, in Fig III-2, Fig III-3 and Fig III-4, all the bolts are not displayed.

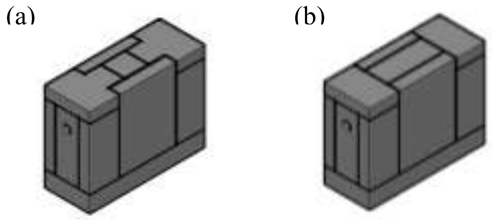

Fig III-2 3D image of all components and combinations of the two kinds of PSC

(a) Assembled chamber with a small cover (b) Assembled chamber with a big cover

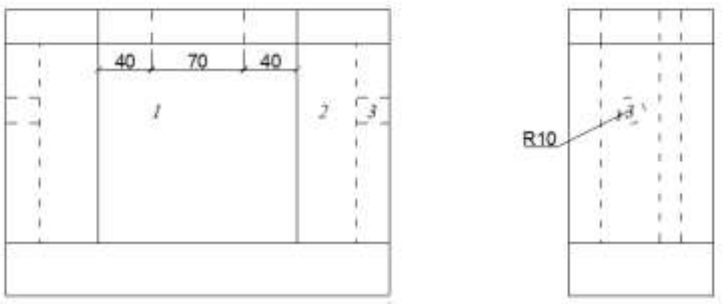

(a) Front view (b) Side view

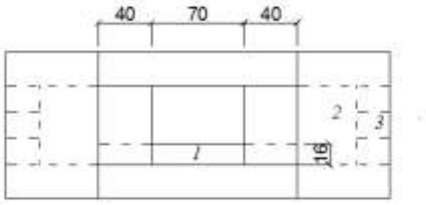

Comment:
Unit:mm
1:chamber for particles
2:chamber for rubber bags
3:water pipe for rubber bags

(c) Top view

Fig III-3 Three views of PSC with a small cover

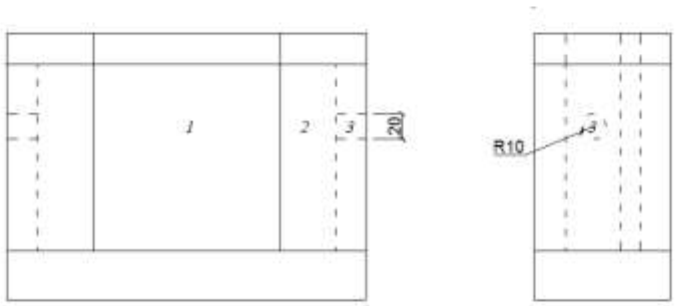

(a) Front view (b) Side view

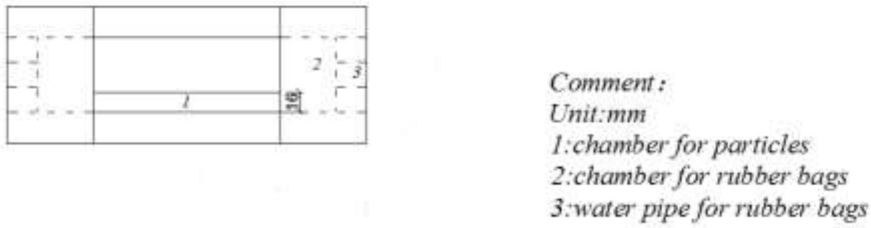

(c) Top view

Fig III-4 Three views of PSC with a big cover

In all the biaxial compression tests, the width of the PSC was controlled to contain one layer of particles. Several batches of particles with different testing conditions were set in the PSC. Biaxial compression tests were conducted on each batch of particles. Two rubber bags filled with water connect with two pressure controls respectively were set at the two sides of the PSC to apply lateral confining stress. Except for the rubber bags, all the contact surfaces of the PSC with particles are PMMA sheets which could be considered as frictionless boundary conditions. During the biaxial compression tests, digital cameras were used to record images at constant time interval. Then the Digital Image Correlation technique (DIC) was used to analyse the images. For all tests, the pixel size was 17 μm. When the PSC was being filled, about 20 particles were put in the PSC every time until the PSC was full. During this process, the PSC was vibrated to make particles as many as possible filled in the PSC. After filling, the confining pressure would be applied and the PSC was placed on the platform of the loading system. A displacement controlled downward load would be applied on the cover and further influence the particles inside. Since the test started, the confining pressure remained unchanged until the test was terminated.

The loading system was an electro mechanic testing machine (EMTM) which could apply vertical load or displacement with a predetermined program.

Camera and EMTM were controlled by computer. For the loading system, all data such as time, vertical displacements, vertical load, were measured by sensors and were recorded. When the real-time load decreased by 40% of the already observed maximum load, the computer would surmise that the sample had lost its bearing capacity and the EMTM would stop the test automatically. If the samples were found losing capacity, the EMTM could also be commanded stop loading manually.

During test, data from EMTM and the two pressure controllers were saved to computer. Photos were taken by the camera and saved to another computer. Data from EMTM were also recorded by photo acquisition software in a same file with the photos number in order to synchronise time, force and displacement with each photo (Fig III-5).

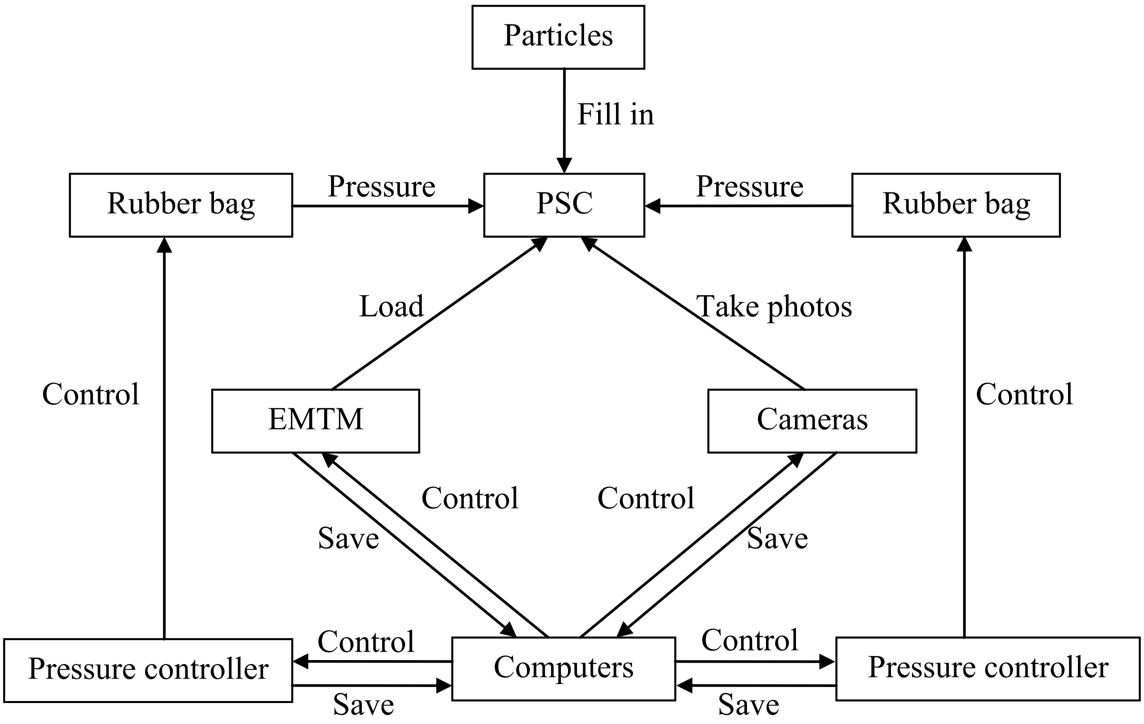

Fig III-5 Sketch of tests instruments

Before each test, a new batch of particles was selected according to the purposed testing condition. The PSC which had been cleaned and assembled would contain the particles and be placed on the loading platform of the EMTM and cameras were set up to record the whole process of the particles displacement and breakage. After setting up the PSC, confining pressure and the cameras, load was applied on the cover of the PSC and camera starts working (Fig III-6).

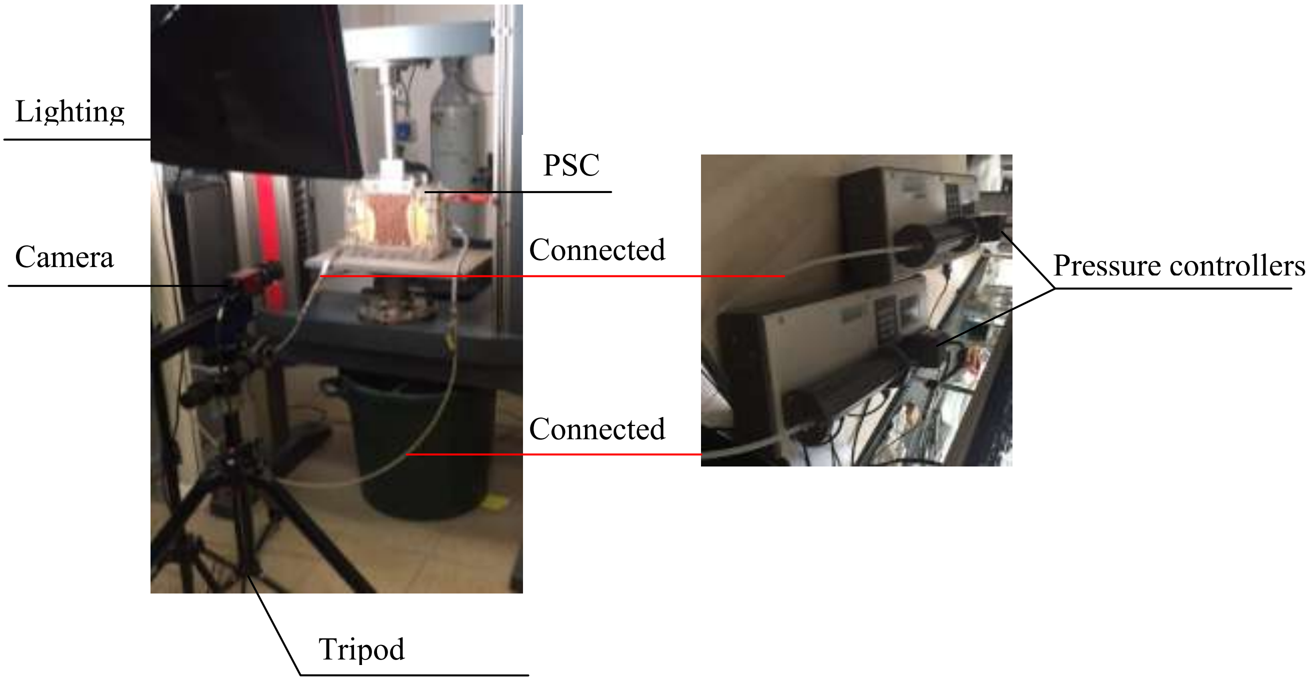

Fig III-6 Assembled test equipments

III.2.3.Analysis methodology

Software written with MATLAB code is used as a tool to analyse the photos. Using this code, the particles can be distinguished from the photos for further analysis. Three modules are used respectively Image Processing Module (IPM), Particle Identification Module (PIM), Data Calculation Module (DCM). The working process is shown in Fig III-7.

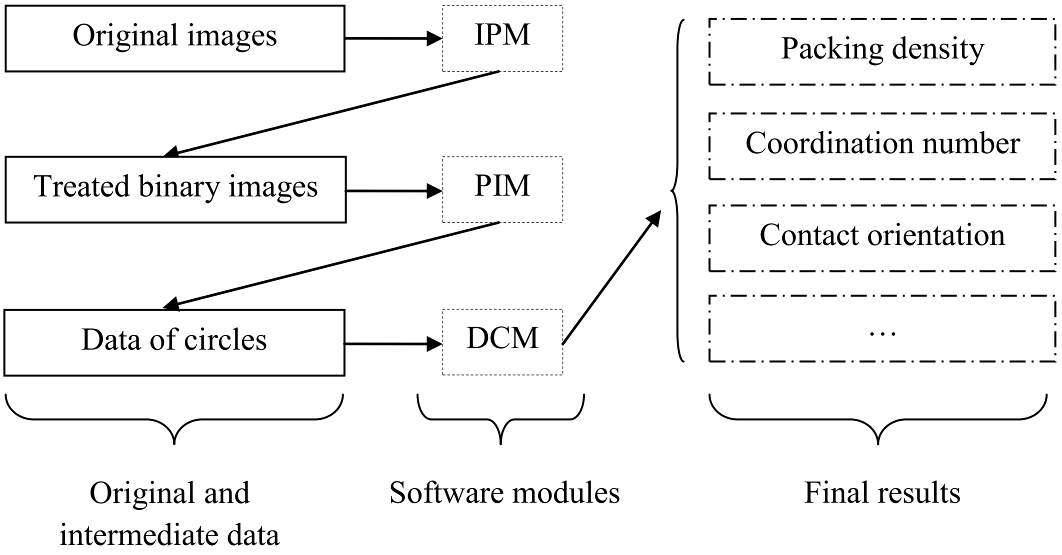

Fig III-7 Working process of the software

In the IPM, images would be imported into the software. After a series of Morphological calculation such as erosion, reconstruction, dilation, and so on, two effects would be accomplished. Firstly, the original images would be transformed from colourful images to greyscale images and finally to binary images. Secondly, noise reduction would be carried out to remove small objects from the original images. The original image and the treated image are shown in Fig III-8.

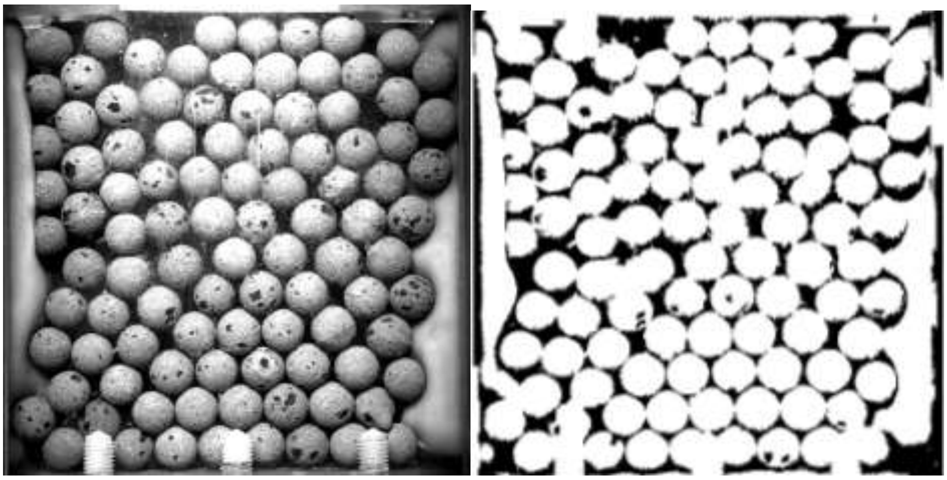

Fig III-8 A comparison between original and treated image

In PIM, the most fundamental data would be extracted from the treated image. Circles could be recognized using circular Hough transformation [142] thus the radius and the coordinate of the centre of the circle could be saved. The obtained radius and coordinate of the centre represent the location and the volume of particles and would be considered as the data for further calculation and analyze. The circles found could be shown in Fig III-9

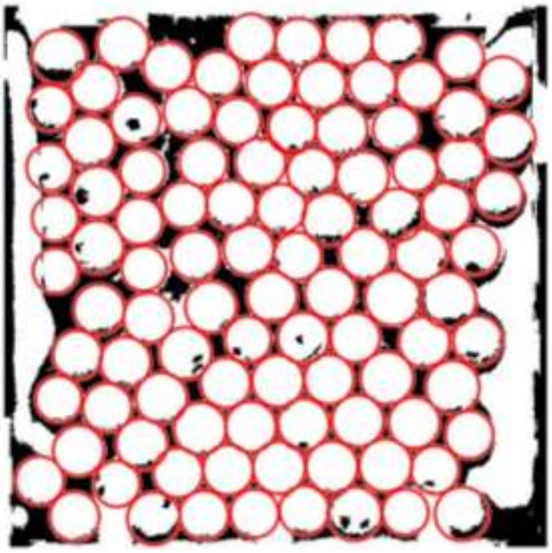

Fig III-9 Circles found in binary image

In the DCM, based on the coordinate of the centre of the particle and its radius further calculations could be carried out. Firstly, void ratio and grain size distribution in any select region could be calculated.

Secondly, by comparing the distance of centres of two particles and the sum of their radius, it could be judged that whether these two particles are in contact. After confirming whether there are contacts between any two particles, the coordinate of all contact and the angles between the contact surfaces and the horizontal plane could be calculated.

Consider a finite population of particles, N_p is the number of particles. A particle number i may be in contact with a particle number j. Each contact between particles i and j is given labelled $c_{i\text{-}j}$. N_c is the total number of contacts.

$$N_c = \sum c_{i-j} \tag{III-1}$$

N_{co} is the coordination of the material. Specifically, it is the average number of neighbours per particle.

$$N_{co} = \frac{N_c}{N_p} \tag{III-2}$$

It should be mentioned that, each contact plane is composed by two contacts which belong to two particles. In other words, $c_{i\text{-}j}$ and $c_{j\text{-}i}$ refer to two contacts in the same contact plane. $\theta_{i\text{-}j}$ is used to express the orientation of the contact $c_{i\text{-}j}$. Specifically, $\theta_{i\text{-}j}$ means the angles of the normal of the contact surface with horizontal plane. With $\theta_{i\text{-}j}$, the contacts orientation of each image is shown with rose diagrams. It is easily shown that the difference *of* $\theta_{i\text{-}j}$ and $\theta_{j\text{-}i}$ is π.

a is used to express the second-order fabric anisotropy. The anisotropy of the contacts is computed with the matrix $\theta_{i\text{-}j}$ [61].

$$a = \frac{2}{N_c} \left| \sum \sin^2\theta_{i-j} - \sum \cos^2\theta_{i-j} \right| \tag{III-3}$$

III.3.Experimental settings

Five tests were performed to study the packing characteristic of granular material under biaxial loading. During these tests, different testing conditions were applied to study the effect of different factors. Among all the test conditions, three mainly considered variables are diameter condition (monosized or polysized), size of top cover and confining pressure. In Test III-1, Test III-2 and Test III-4, the diameters of particles were between 14-16 mm which was considered as monosized particles. The second different setting condition is the type of top cover. For Test III-1, Test III-2 and Test III-3, the small top cover was utilised whose length is 70 mm however for Test III-4 and Test III-5, the larger top cover with a length of 150mm was used. Thirdly, the confining pressure was also different. The confining pressure for Test III-1 was 10 kPa. The confining pressure for Test III-2 and Test III-3 was 40 kPa. The confining pressure for the last two tests was 20 kPa. In Test III-3 and Test III-5 polysized particles were tested. Material parameters and test conditions are presented in Table III-1

Name	Test III-1	Test III-2	Test III-3	Test III-4	Test III-5
Diameter condition	monosized	monosized	polysized	monosized	polysized
Resolution (mm)	0.078	0.079	0.078	0.078	0.079
Loading speed (mm/min)	1				
Mass (g)	118	120	134.5	112	118
L*W*H ($mm^{3)}$	130*16*150				
Type of cover	small			large	
Confining pressure (kPa)	10	40		20	

Table III-1 Setting of the 5 tests

The GSD line of the particles before five tests is presented in Fig III-10. The initial states of the five tests are presented in Fig III-11. Another state of the 5 tests when the displacement of the cover is 16.67 mm is shown in Fig III-12.

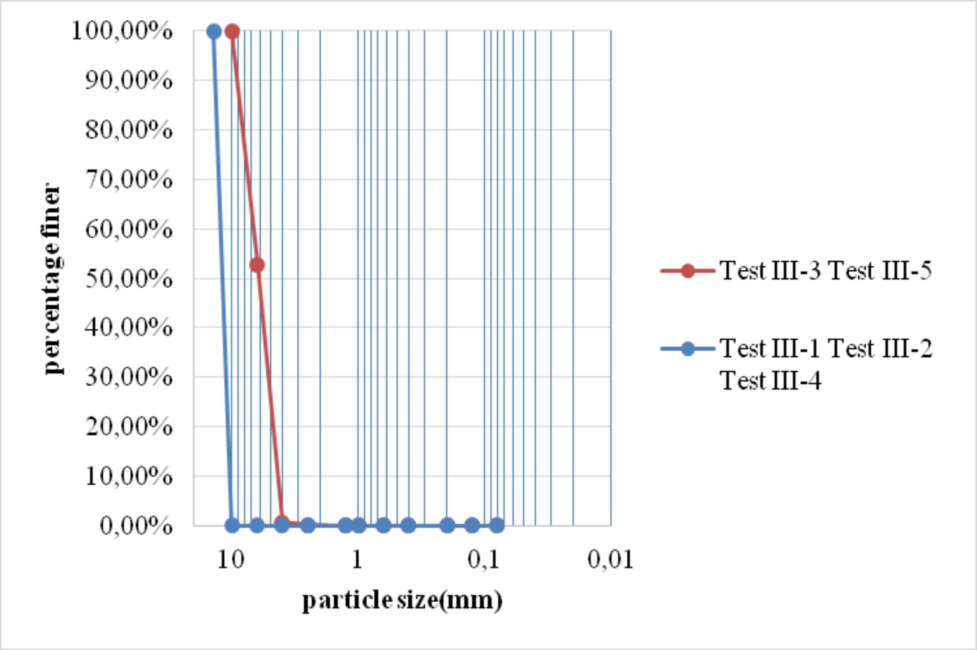

Fig III-10 Grain size distribution curves of 5 tests.


(a) (b) (c) (d) (e)

Fig III-11 Starting states of the 5 tests

(a): Test III-1 (b): Test III-2 (c): Test III-3 (d): Test III-4 (e): Test III-5


(a) (b) (c) (d) (e)

Fig III-12 Image 100 of the 5 tests

(a): Test III-1 (b): Test III-2 (c): Test III-3 (d): Test III-4 (e): Test III-5

III.4.Experimental results and discussion

III.4.1.Packing density

The packing density of granular material could be defined as the fraction of the summation of volumes of all single particles by the total space filled by particles. This ratio is also defined as packing fraction by some other scientists. In contrast, porosity or void fraction describes the ratio of the volume of void to the total packing volume. Normally, φ and n are used to express packing density and porosity, respectively. The two quantities are linked by,

$$\varphi + n = 1 \qquad \text{III-4}$$

Based on the computed results obtained by post-processing the photos, the evolution of the packing density is shown in Fig III-13.

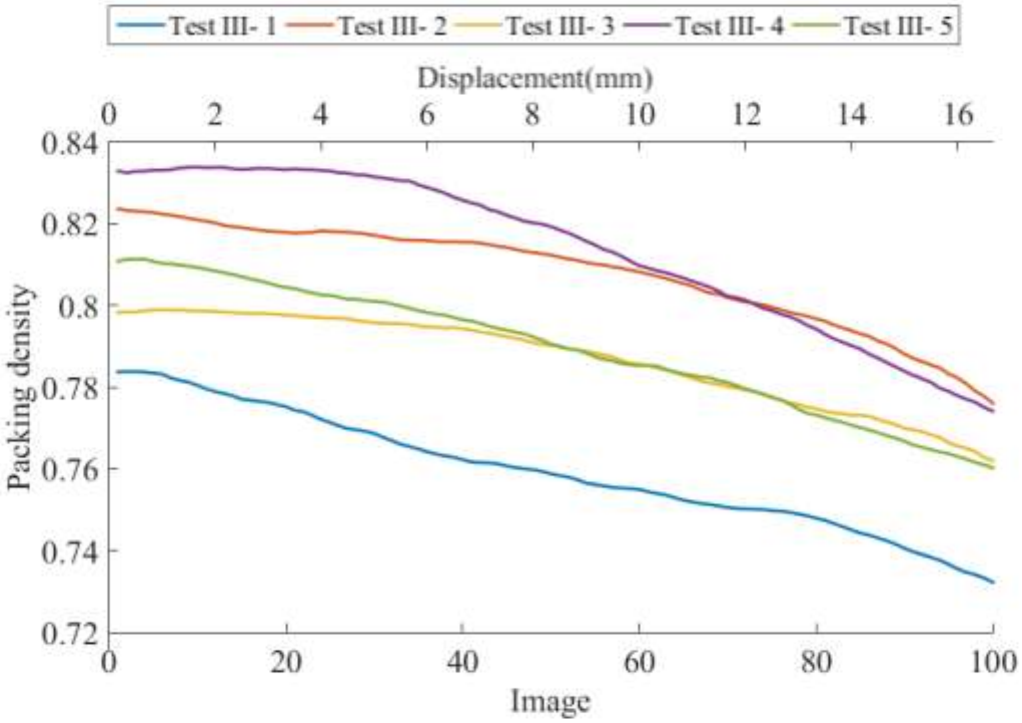

Fig III-13 Evolution of packing density of tests

At the initial state, the packing densities of specimens were similar and varied from 0.78 to 0.83. The packing density of Test III-4 is the higher than the packing density of Test III-5 tests and decreased from Test III-2, Test III-5, and Test III-3 to Test III-1.

Casagrande et al [88] revealed that, for granular material with dense packing taking load, the packing density would decrease as a result of dilation. However the packing density of the material of loose packing increased under the action of contraction. For all the tests, the packing densities decreased from the beginning to the end of loading thus the final value of the packing densities were smaller than the initial. This phenomenon proved that, when the tests started, the samples were dense packing. Under the action of vertical load and horizontal confining pressure, some particles breakage appeared (Fig III-14) but the packing densities could not rise. Instead, the almost tight arrangement structure was disturbing continually by the downward displacement of the cover. At the process, some voids appeared and the packing densities decreased.

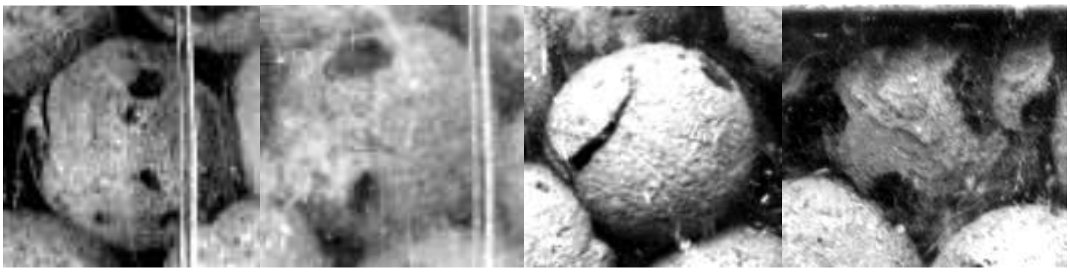

Fig III-14 First breakage of each test

(a): Test III-2 (b): Test III-3 (c): Test III-4 (d): Test III-5

From the beginning to the end, the packing density of Test III-1 was smallest and had no cross with other curves. The reason is its smallest confinement pressure.

For Test III-2 and Test III-4, it could be seen that at the beginning, the packing density of Test III-4 is bigger than Test III-2. However, the packing density of Test III-2 surpassed Test III-4 after image 65 and finally the gap between them became constant. The important difference between the two tests was the type of top cover and confining pressure. The larger top cover could lead to a larger packing density because of its better impermeability. However as the test continued, the influences of the covers decreased. Compare with Test III-1, it could be concluded that the confining pressure could cause an increase of the intensity of the arrangement. But this kind of influence diminished as the growing of the confining pressure. When the confining pressure was increased to a certain value, the packing density of particles would reach a peak value and since then, the continuing increasing confining pressure would not affect the intensity of the arrangement. The comparison of the curves of Test III-3 and Test III-5 could prove this point again.

Comparing Test III-4 and Test III-5, the packing density of Test III-4 was greater than Test III-5 throughout the test. The only difference of Test III-4 and Test III-5 is the condition of diameter. It could indicate that monosized particles could lead to a bigger packing density than polysized particles. Comparing with Test III-2 and Test III-3, a similar conclusion could be drawn.

The comparison of packing density of different spherical or approximate-spherical particles diameter conditions has been made by Wong [80]. He explained that, if some certain condition could be met, the packing density of polysized particles is bigger than the packing density of monosized particles because the particles of decreasing sizes could always fill up the gaps between the bigger ones. If process of filling up could be extended infinitely by increasingly smaller particles, the whole space could be completely filled up and the packing density could be close to 1. The process above was called filling effect. Nevertheless in reality, the above process is very difficult to achieve because of a lot of restrictions. For example, it is easy to imagine that the big particles and smaller particles which filled in the gaps between the big ones have to maintain a certain proportion on diameter. For example, the diameter proportion of the biggest particles and the second biggest should agree with $1:(\sqrt{2}-1)$. In contrast, if the fine particles are not small enough to fill up the gaps between larger ones, the larger particles would be pushed apart which leads to an increase in void volume and decrease in packing density and this process was called loosening effect (Fig III-15) [82]. In other word, for an assembly of polysized particles, the changes of packing density from monosized ones are determined by proportion of diameters of different particles.

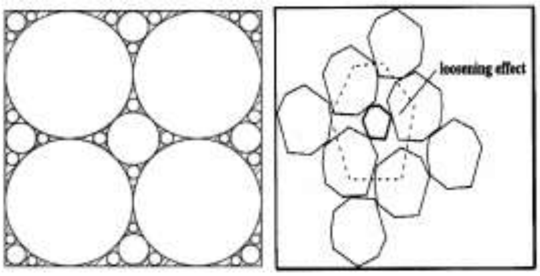

(a) (b)

Fig III-15 Packing of polysized particles from Larrard's work

(a): Filling effect. (b): Loosening effect

For the polysized particles of our tests, it could be observed from Fig III-10 that the gaps between particles of different diameters are not enough thus the smaller particles could not fit them into the void between the bigger ones. Therefore, the loosening effect played a decisive role and the packing densities of the polysized particles are smaller than the monosized ones.

III.4.2.Coordination number

The coordination number of granular material describes the mean number of particles which are in contact with a certain one. The contact particles are also called neighbours. It could be related to the microstructure evolution of the material. It is commonly accepted that for the granular material of same composition, a bigger coordination number means a denser arrangement. The evolutions of coordination number of the five tests are shown in Fig III-16.

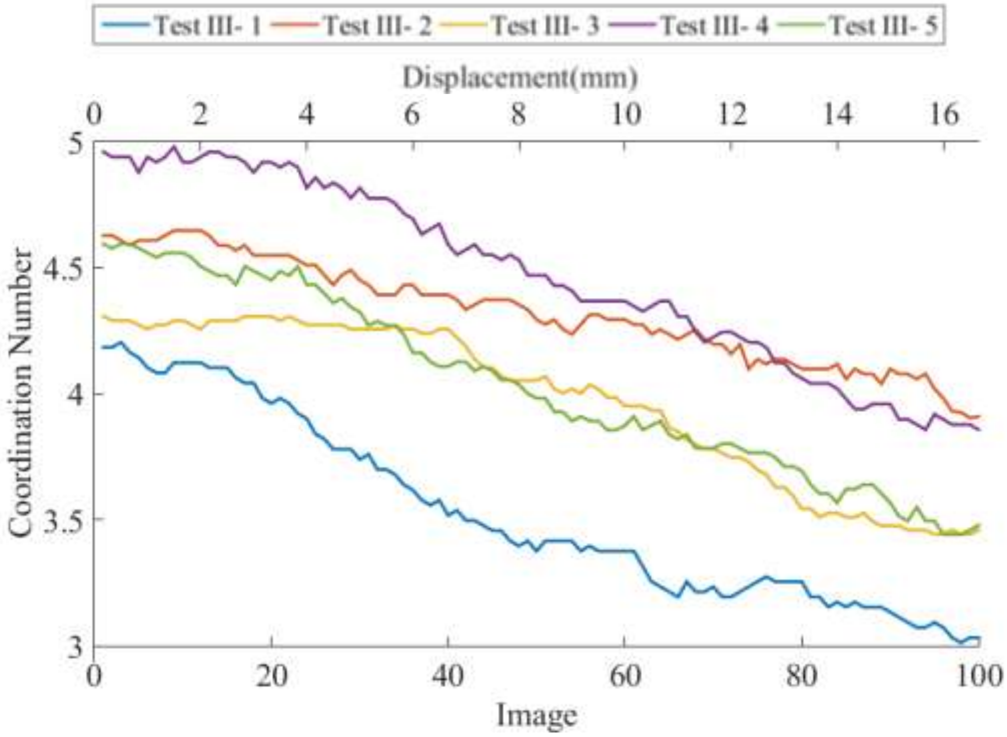

Fig III-16 Evolution of coordination number of the tests

Comparing to Fig III-13, it could be found that the relative positions of the curves are approximately the same. To be specific, comparing Test III-1 Test III-2 and Test III-4 whose particles were monosized, the conclusions are similar to the curve of evolution of packing density. The curve of Test III-1 decreased from the beginning to the end and located at the bottom among all of the five curves. The reason is that in Test III-1, the confinement pressure is only 10kPa so its restraining action to the particles is relatively small. The curve of Test III-4 and Test III-2 had a downward trend throughout the tests. However at the beginning, the coordination number of Test III-4 had a greater value but at the end the coordination number of Test III-2 was bigger. This indicated that when the tests began, particles of Test III-4 were denser than particles of Test III-2 but when the tests finished, this relation was inversed. This is because the larger cover of Test III-4 could lead to a denser environment at the beginning however its influence to the allocation of particles decreased as the tests went on. As the process of the tests, the influence of confining pressure is that particles of Test III-2 with greater confining pressure became denser finally. However, the influence of confining pressure was generally weak when its value was beyond 20kPa. Because arriving at this value, the void in the particles packing had been nearly compressed to minimum. In other words, when the confining pressure reaches a certain value, there would be little space for an increasing confining pressure taking effect. This is also the reason that when the curve of Test III-2 surpassed the curve of Test III-4, the gap between them showed no sign of rising. This conclusion acted more clearly with Test III-3 and Test III-5. When the curve of Test III-3 caught up with Test III-5, the two curves went with intersections.

III.4.3.Contact orientation

Packing properties of a granular material could be related to the distribution of particles contact direction. This concept is called contact orientations. For a given contact surface on the frontier of a particle, the contact orientation is the included angle of the normal of the contact surface and a datum line. In this work, the datum line was the horizontal line. In this section, the distribution of contact orientations of the five tests is shown on Table III-2. Generally, the studies of contact orientation of monosized particles samples are more meaningful however the contact orientation of polysized particles samples is usually less significant. The reason is the arrangement of particles with different diameters has a strong randomness. Therefore, for the polysized particles, the results of contact orientation and other relative data will be displayed but the focus of analysis will be stayed on monosized particles.

It is easy to imagine a Perfect Model for monosized particles that they are set in a chamber absolutely orderly and tightly (Fig III-17). Each particle will have 6 contact surfaces with the same included angle of 60^o and all particles clusters contain 3 particles. For different particles, the relative positions of the contacts are the same. Under this condition, the rose curve of contact orientation would be contained by six bins which have the same length and same included angle between each other (Fig III-18). In the laboratory test, there are some differences on the particles sizes filling in the chamber. The assemble particles would have confinement pressure and vertical load. Under the influence of such conditions, the arrangement of the particles would not be as perfect as the Perfect Model. Thus, the rose curve would contain much more than 6 bins. However it could be expect that there are 6 bins which should be still much longer than others and we can call them Main Bins. Visually, the arrangement of particles are denser, the rose curves are more close to the Perfect Model. In specific, the Main bins would be more outstanding in the length and the included angle would be closer to 60^o.

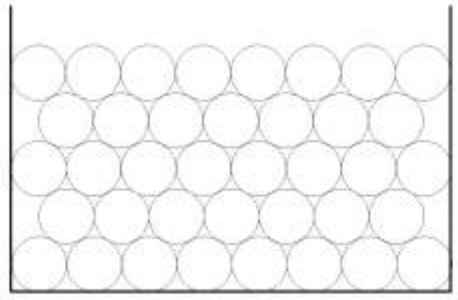

Fig III-17 The Perfect Model of monosized particles packing

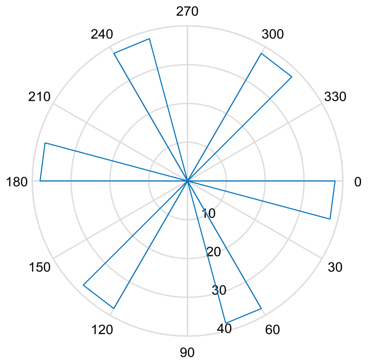

Fig III-18 Rose curve of contact orientation of Perfect Model

Every 10 image or every 10/6 mm of the displacement of the top cover, the rose curves of contact orientations would be drown and displaced in Table III-2. Each curve describes a statistic of orientation of contacts of each image. Every curve is central symmetry because each contact surfaces is shared by two contacts with exactly opposite direction on the frontier of two particles as explained in III.2.3.

Image	Displacement(mm)	Test III-1	Test III-2	Test III-3	Test III-4	Test III-5
1	1/6	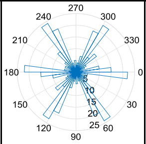	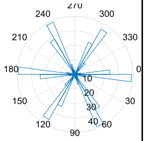	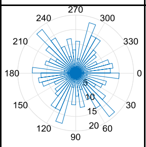	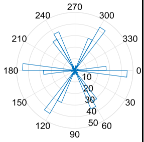	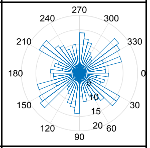
10	10/6	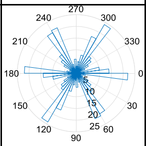	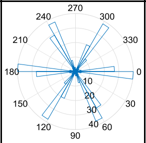	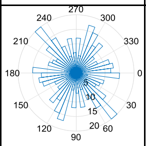	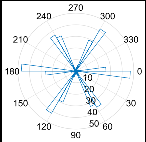	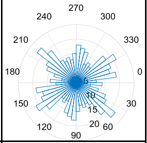
20	20/6	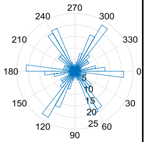	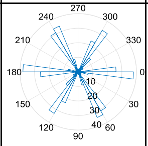	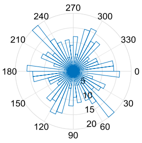	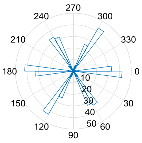	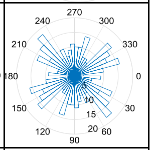
30	30/6	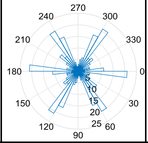	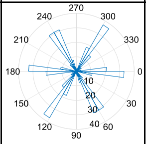	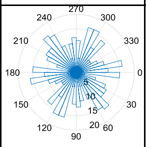	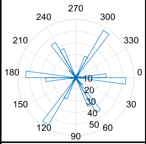	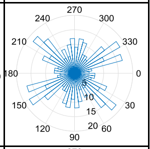
40	40/6	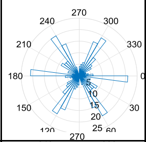	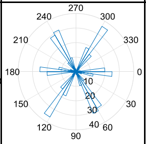	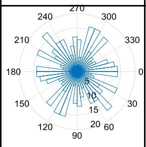	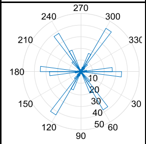	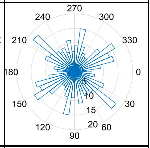
50	50/6	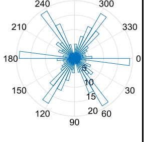	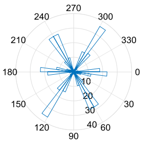	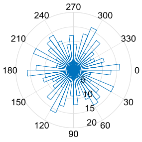	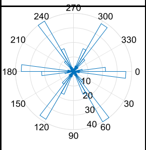	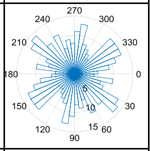
60	60/6	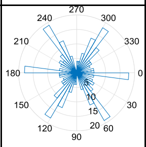	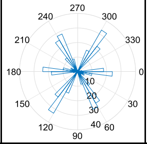	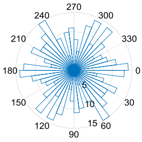	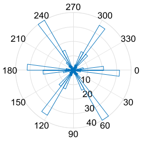	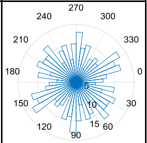

70	70/6	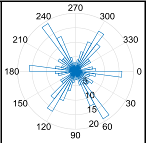	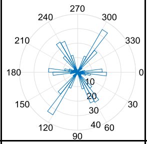	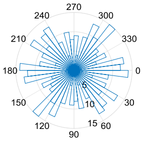	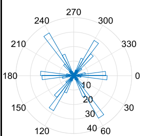	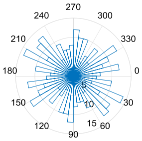
80	80/6	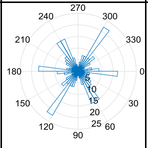	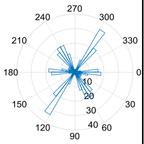	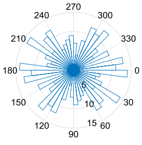	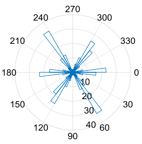	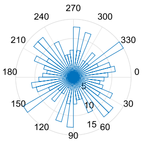
90	90/6	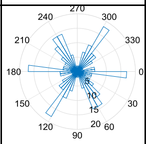	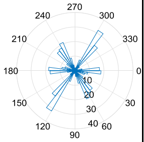	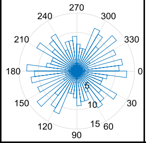	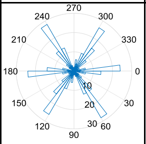	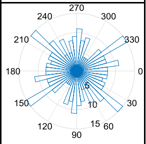
100	100/6	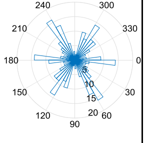	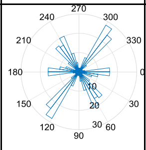	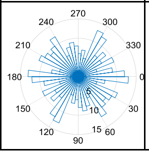	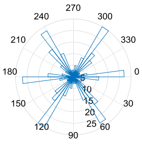	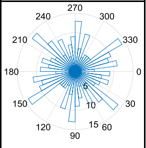

Table III-2 Rose curves of contact orientation of laboratory tests

It could be observed that the rose curves of Test III-1, Test III-2 and Test III-4 show obvious similarity with the rose curve of the Perfect Model. The length and location of the longest bins which reflect the main feature of the contact orientation are almost the same. The included angles between each main bin also keep 60°. This phenomenon could show that the particles arranged densely and orderly. For Test III-3 and Test III-5, the distribution of the bins appeared without obvious regulation which reveals the distribution of contact orientation is random.

Comparing results of Test III-1, Test III-2 and Test III-4, the rose curves of Test III-4 more look like the rose curve of the Perfect Model whereas the rose curves of Test III-1 show relative larger difference. In order to analysis the rose curves of orientation quantitatively, a factor with a name *orientation factor* describing the sum of gaps of all bins from the Main Bins which could reflect the differences between the Perfect Model is introduced.

$$G_a = \frac{1}{N_{co}} \sum (\theta_{i-j} - \theta)^2 \qquad \text{III-5}$$

In which

$$\theta = \begin{cases} 0 & 0 \le \theta_{i-j} < {}^{\pi}/_{6} \\ {}^{\pi}/_{3} & {}^{\pi}/_{6} \le \theta_{i-j} < {}^{\pi}/_{2} \\ {}^{2\pi}/_{3} & {}^{\pi}/_{2} \le \theta_{i-j} < {}^{5\pi}/_{6} \\ \pi & {}^{5\pi}/_{6} \le \theta_{i-j} < {}^{7\pi}/_{6} \\ {}^{4\pi}/_{3} & {}^{7\pi}/_{6} \le \theta_{i-j} < {}^{3\pi}/_{2} \\ {}^{5\pi}/_{3} & {}^{3\pi}/_{2} \le \theta_{i-j} < {}^{11\pi}/_{6} \\ 2\pi & {}^{11\pi}/_{6} \le \theta_{i-j} < 2\pi \end{cases} \qquad \text{III-6}$$

For the Perfect Model, G_a equals to 0 since all bins are on the certain directions. For the packing which is arranged loosely or with polysized particle, the characteristic of distribution of bins of the orientation rose curve will be less stark. When the bins of the rose curve are spread completely evenly, the G_a will be 0.1493. When the G_a is more close to zero, the particles would be denser packed. Curve describing the evolution of the G_a of the 5 tests is shown in Fig III-19.

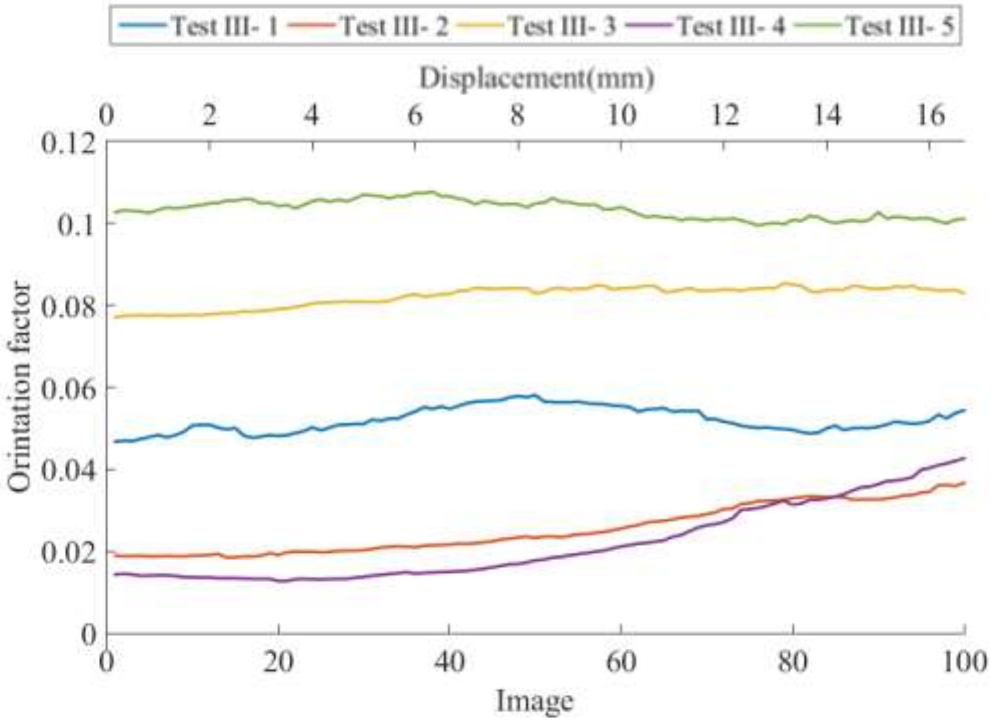

Fig III-19 Orientation factors of laborotary tests

It could be observed that, among monosized particles, the G_a of Test III-1, Test III-2, and Test III-4 increased with fluctuations. The G_a of Test III-1 was bigger than the G_a of other two tests. The G_a of Test III-2 was bigger than the G_a of Test III-4 but as the tests went on, it was finally crossed by G_a of Test III-4 after image 80. The entire above phenomenon basically match the results of packing densities and coordination numbers above-mentioned. It could be proved that the G_a could be a parameter which describes the packing situation of monosized particles. The particles pack better when the parameter is closer to 0.

III.4.4.Comparison of upper part and lower part

In Fig III-11 and Fig III-12, it could be observed that, if the assembly of particles are divided into two parts according to the location from top to bottom, the void volumes appear obvious distinction. Particles in Test III-4 would be set as an example and divided into two parts: upper part and lower part (Fig III-20).

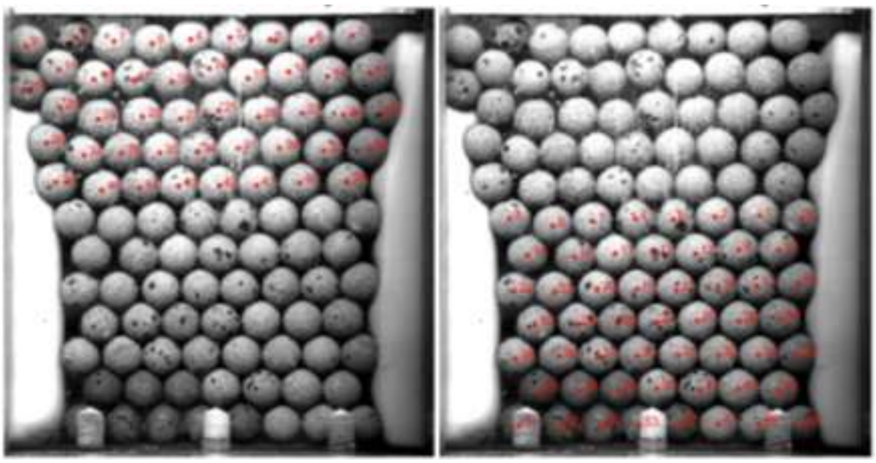

Fig III-20 Analyzing zone of upper part and lower part of Test III-4

Packing density and orientation factors of the different parts are calculated respectively and shown in Fig III-21 and Fig III-22. Contact orientation is displaced with a same interval of III.4.3 in Table III-3.

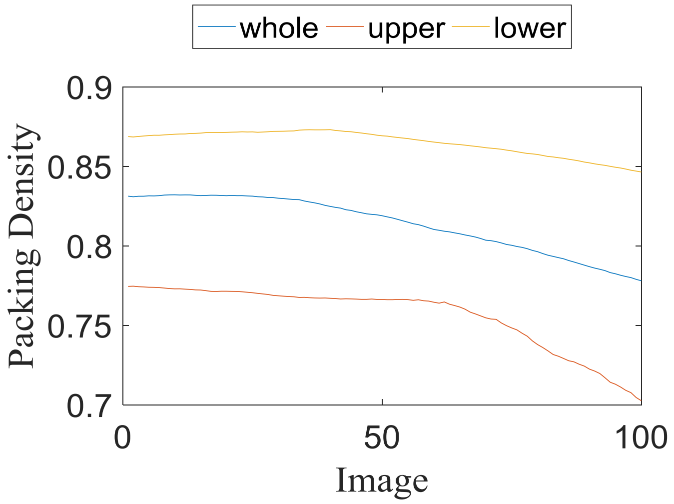

Fig III-21 Packing densities of different parts of Test III-4

image	Displacement(mm)	Whole	Upper	Lower
1	1/6	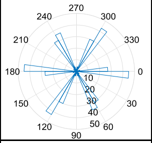	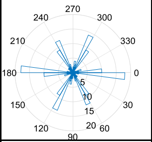	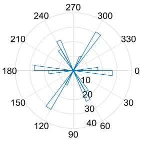
10	10/6	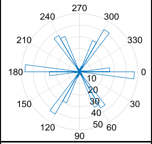	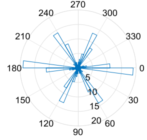	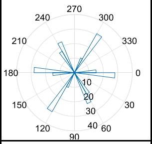
20	20/6	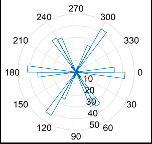	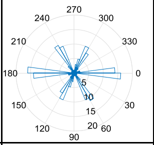	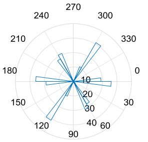
30	30/6	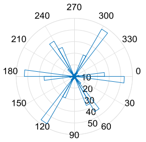	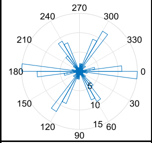	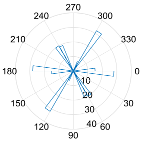
40	40/6	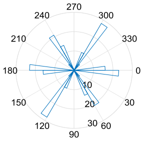	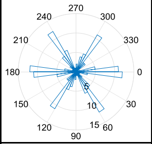	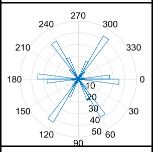
50	50/6	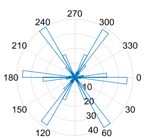	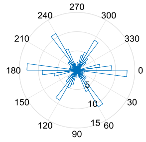	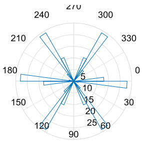
60	60/6	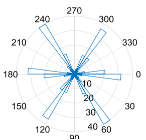	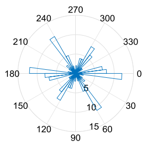	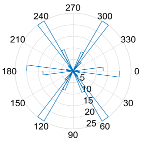
70	70/6	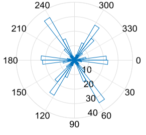	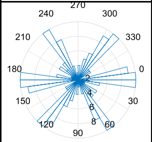	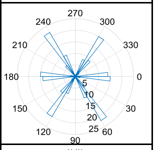
80	80/6	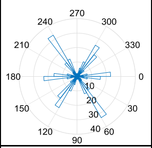	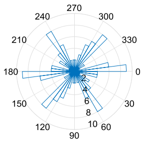	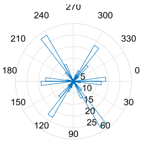
90	90/6	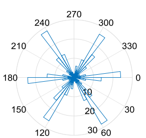	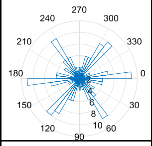	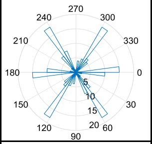
100	100/6	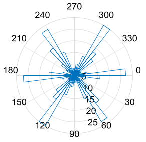	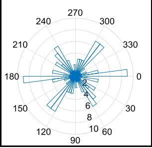	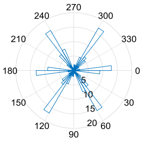

Table III-3 Roses curves of different parts of Test III-4

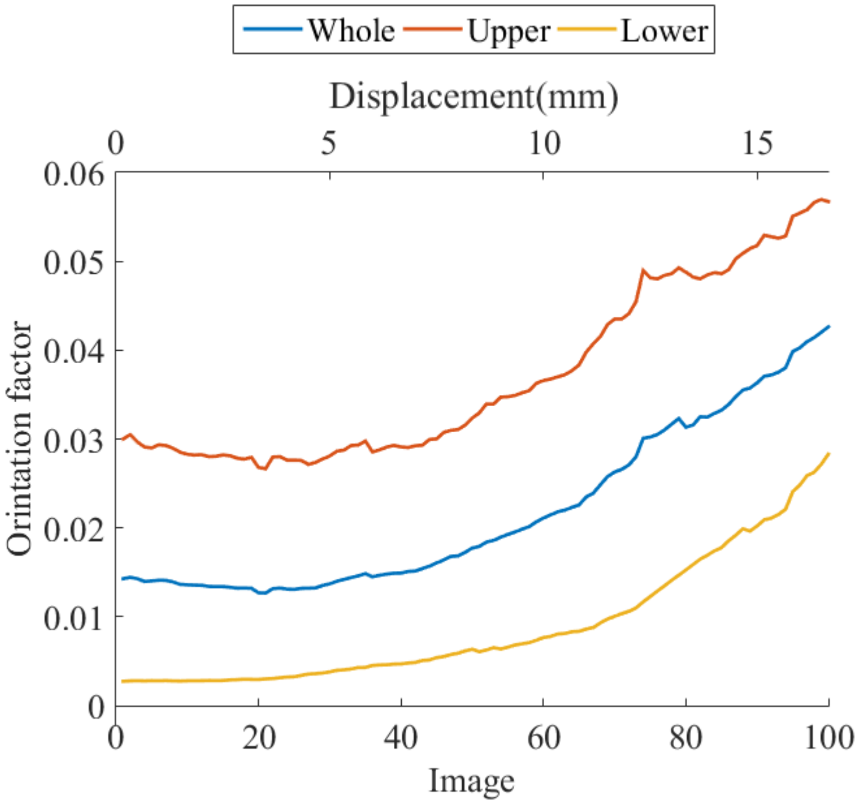

Fig III-22 Orientation factors of different parts of Test III-4

From the rose curves of contact orientation, it is easy to observe that at the lower part, the rose curves are similar to the rose curve of the Perfect Model. The length and location of the longest bins which reflect the main feature of the contact orientation are almost the same. The angles between main bins also keep 60°. Moreover, the change on the rose curves on the bottom as the tests went on was relatively small. In contrast, particles on the upper part show great differences. At the beginning, the difference is still not very obvious. But the distribution of bins shows increasingly difference as the tests went on. The sharp contrast between the upper part and lower part of particles is due to two reasons. At first of all, as mentioned before, particles were put inside the chamber slowly and with uninterrupted vibration. The aim is to make the packing denser. So the particles at lower part suffer longer vibration and vertical loads of the particles at upper part. Therefore at the beginning the packing density of particles at lower part is bigger than that of particles at upper part. Secondly, during the test, the structure of assembled particles, especially on the upper part, was influenced by the perturbation of the cover. Thus, the particles at upper parts also had a higher decreasing rate of packing density. This conclusion could also be verified by the curve of packing densities and orientation factors at different parts.

III.5.Summary

The objective of this chapter is to illustrate the impact of various factors on the packing characteristic. In order to achieve this goal, a Plane Strain Chamber (PSC) is assembled for the tests. Five biaxial compression tests were performed on approximately spherical particles and photos were taken to record the experimental procedure. Software written with MATLAB code was applied to analyze the photos and to calculate various parameters. A parameter called Orientation Factor is introduced to analyze the contact orientations. Finally, some conclusions could be drawn.

First of all, after a vibrated filling process, the particles in our tests could almost reach each optimal packing status. The loading actions after this could not make the packing further denser. Instead, the perturbation of the cover could make the packing become looser.

Secondly, because of the rubber bags on the left and right sides, the using of small cover could cause the junctions of the cover and the rubber bags were not close enough which could further lead to a looser packing density of the particles. But this effect disappeared gradually as the tests went on.

Thirdly, when the confining pressure is not very big, the increase of confining pressure could lead to a denser packing of particles. But with the growing of confining pressure, the same pressure difference would result in smaller and smaller packing density difference.

Fourthly, in our tests, the packing densities of polysized particles are smaller than that of monosized particles. Because the diameter gaps between particles in different size are not big enough. The smaller particle could not fill the void between the larger ones. Instead, they would push apart the larger ones and give rise to a lower packing density.

Finally, the packing on the upper parts and lower parts also have some differences. Briefly, the packing density on the upper part is smaller than that of lower part because of different vibration effect when filling the PSC and different perturbation effect of the cover during loading.

Chapter IV. Mechanical and Kinematical Characteristic of Multiple Particles when Baring Load Considering Particle Breakage

IV.1.Introduction

IV.1.1.Research background

The mechanical behaviour of granular material is different from continues material, and is strongly affected by the relative arrangement of voids and particles. Some classical theories based on continues material were born with a focus on this field such as the Mohr–Coulomb theory which is named in honour of Charles-Augustin de Coulomb and Christian Otto Mohr to describe the shear strength of soil [91]. Karl von Terzaghi revealed filtration theory of consolidation and principal of effective stress which act as basic principles of soil mechanics [92][92]. The crushing of particles which is a component of granular behavior may have a huge impact on the mechanical property of granular material. A changed grain size distribution may lead to an upheaval of the micro structure. Therefore, the mechanical behavior of granular material considering particles crushing has attached considerable attention in recent years.

Yamamuro et al [105][91] performed drained triaxial compression tests on dense Cambria sands and found that the most basic factor affecting crushing degree are the inherent strength and the effective stress state. Particle shape is another dominant factors affecting particle breakage behavior. Santamarina et al [107] summarized three principle scales to describe particle shape: sphericity, angularity and roughness which influence soil behavior. His results showed that, sphericity could increase the stiffness and residual friction angle. The increase of angularity and roughness could cause a decrease in small-strain stiffness and a growth in high-strain strength. According to Cheng [115], the confining pressure could influence the particles crushing following the results of tests with imported microspheres bonded together simulating crushable particles with DEM. Kou [116] studied the influence of friction of the container walls on the particles breakage. His results demonstrated that with friction on the boundary, the particles breakage starts earlier and more concentrated to the boundary. Moreover, without boundary friction, particles breakage occurred less on the top. In Indraratna's work [123], a model incorporating the deviator stress, dilatancy, friction angle and energy consumption considering particle breakage was built to investigate the effect of particle crushing on shear strength. Finally, he found that the rate of energy consumption shows noteworthy relationship with the rate of particle crushing. In addition, the friction angle increases with the rate of particle crushing which lead to a decrease of material's shearing strength

In several works, constitutive models of granular material with the consideration of particle breakage were developed. Wadud [126] developed an elastoplastic constitutive model for coarse aggregates during triaxial shearing based on critical state and plasticity theory which could calculate the stress-strain relation and volume change of coarse aggregates. Using a three-segment critical state line within a boundary surface, Russell [127] described the behavior of granular material considering particle crushing by building a constitute model. Based on the concept of critical state soil mechanics, Huabei [128] developed a plasticity constitutive model for sand. In addition, his model could be used to evaluate sands crushing under cyclic loading. Hu [129] introduced an elasto-plastic model whose feature contains the critical state line movement because of the particles breakages. A verification with some test results demonstrated that his model could accurately reflect the mechanical behavior of crushable granular material and predict the GSD evolution during the test. Daouadji developed an elasto-plastic constitutive model which could calculate the behavior of granular material under isotropic and trixial loading. He described the position of critical state line according to the amount of energy sufficient for particle crushing. In addition, he also provided a curve on which the critical state line in the *e-logp'* coordinate system dropped accompanied with the evolution of particle gradation. His model considered the local strength of particle and was validated with two kinds of material. Besides, the results reproduced a good accuracy of the granular material mechanical behavior [130]. After night years, Daouadji introduced an enhanced constitutive considering the influence of amount of particle breakage. The model was calibrated with a comparison of tests on three different kinds of material and the simulations were close to tests results [131].

IV.1.2.Aim and objectives

This chapter aims to study the mechanical and kinematical characteristic of multiple spherical particles made by porous heterogeneous material when applying vertical load from the top. Therefore, a series of experimental biaxial compression tests have been performed. To analyse the photos which recorded every state (2 photos per second) during the tests, software written with MATLAB code is used to analysis the results.

This chapter is organized with four parts which address different contents. References among part 1 could guide the reader to focus on specific topics. In part 2, the experimental apparatus and methodologies are described and the analytisis method is introduced. In addition, the test settings are also illustrated in this part. In part 3, the experimental results are analysed. Part 4 concludes the main results.

IV.2.Experimental apparatus and methodologies

IV.2.1.Tests setting and experimental apparatus

Nearly spherical particles made by light expanded clays were used to perform the biaxial compression tests. The material property is the same as biaxial tests of Chapter

III and is introduced in III.2.1. Groups of particles were put in a chamber called PSC and were influenced by displacement-controlled load from its top. Lateral confining stress was controlled by two rubber bags located on the left and right sides of the PSC. The detailed experimental mythology and apparatus is introduced in III.2.2.

In this chapter, six tests were analyzed to study the mechanical and kinematical characteristic of granular material under biaxial loading. Some tests are the same ones of biaxial compression tests of Chapter III. Since the study is not duration of Chapter III, all the tests are renamed with a new order. During these tests, different testing conditions were applied to study the effect of different parameters. Among all the test conditions, three parameters are investigated: diameter of particles, the size f the zone under compression and confining pressure. In Test IV-1, Test IV-2, Test IV-3, and Test IV-5, the diameters of particles are between 14-16mm which could be considered as monosized particles. In Test IV-4 and Test IV-6, polysized particles were tested. Before conducting the tests, particles were cleaned by high pressure air to prevent the influence of the tiny sub-particles which make little contribution to the mechanical behavior and could increase the difficulty of observing the experiments. The GSD lines of the particles before tests are presented in Fig IV-1. Different top cover was used with the PSC in order to change the area of the compression zone. In Test IV-1, Test IV-2, Test IV-3, and Test IV-4, the small top cover with 70 mm length was used. However, for Test IV-5 and Test IV-6, larger top cover with the length of 150mm was used. The PSC could be observed in Fig III-2, Fig III-3, and Fig III-4. The confining pressure was also different and the confining pressure for Test IV-1 is 10kPa. The confining pressure for Test IV-2 was 20kpa. The confining pressure of Test IV-3 and Test IV-4 was 40kPa. The confining pressure for the last two tests was 20kPa. All tests settings could be seen in Table IV-1.

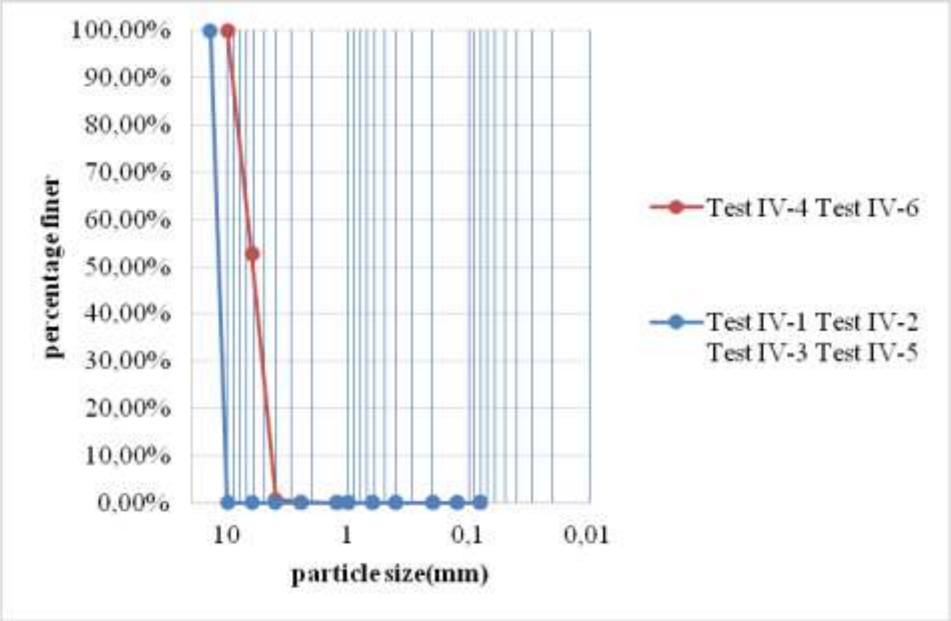

Fig IV-1 The GSD curve of 6 tests

Name	Test IV-1	Test IV-2	Test IV-3	Test IV-4	Test IV-5	Test IV-6
Diameter condition	monosized	monosized	monosized	polysized	monosized	polysized
Resolution(mm)	0.078	0.078	0.079	0.078	0.078	0.079
Loading speed	1mm/min					
Mass(g)	118	122	120	134.5	112	118
L*W*H(mm^3)	130*16*150mm^3					
Type of top cover	small				large	
Confining pressure(kPa)	10	20	40		20	

Table IV-1 Setting of the 6 tests

IV.2.2.Analysis methodology

A script written with MATLAB is used as a tool to analyse the photos. Using this code, the particles can be distinguished from the photos for further analysis. The three modules, Image processing module, Data acquisition module, Data calculation module, which have been introduced in III.2.3 also need to be used in this chapter. In these previous three modules, pictures were analyzed to select the particles. The coordinates and diameter of all the particles could be acquired. However, in the previous three modules, photos are analysed one by one and no connections with the same particles on neighbour pictures could be built. Nevertheless, in this chapter, displacement characteristic of particles are analysed. Therefore, the software needs to distinguish the same particle in different photo and follow it. Furthermore, the software could calculate the displacement trace of all the particles and a further analysis of the displacements vectors of particles could be performed.

Therefore, the forth module, Image Comparison Module (ICM) was developed. First of all, what needs to know is the plotting scale between the pixel on a photo and real distance. Consequently, before performing the laboratory tests, a ruler with scales was put tightly cloth to the PSC and a photo was taken whose name was Scale Image. Before analysing the images, the Scale Image is open firstly and two points on the ruler would be selected and the distance in mm between these points could be read on the ruler and put in the software manually. In the same time, the MATLAB code measured the distance in pixel and made a comparison of actual distance. Then it could be acquired that how many millimetres does one pixel on the photos equal to (Fig IV-2). If the plotting scale is k, the real distance whose unit is mm of the two selected points is d_{mm} and the corresponding pixel detected by the MATLAB is d_{pi}

$$k = {}^{d_{mm}}\!/_{d_{pi}} \tag{IV-1}$$

Since the distance between the camera and the PSC kept the same during each test, k remained unchanged during each test.

Between any two successive images, the coordinate of the centre point of each particle would be compared with the coordinate of centre of all particles in the other image. When the difference of two coordinate is less than a fixed limit, these two coordinates would be judged as the coordinates of the same particle in second photo. The displacement vector is calculated as the difference of its coordinates in the photos. When this method is applied to all particles of the first photo, all particles could achieve one-to-one correspondences to the successive photo. Then this method could be repeated with the next photo. Through following this method, when analyses of all photos are finished, the software could trace the motion of all the particles. Finally, the displacement vectors for each particle at any time step could be calculated and statistic results of the displacement characteristic of all particles could also be calculated.

For an arbitrary particle j, the vector of displacement is described by two independent variables, displacement direction and displacement magnitude. d_{mj} is used to describe the displacement magnitude of particle j in pixel and d_{dj} is used to describe the angle between the displacement direction of particle j and vertical down direction. To express the displacement vector simpler and easier for further calculation, the vector of the displacement of particle j could be described as

$$V_j = d_{mj} * exp\left(i * \pi * d_{dj}\right) * k \qquad \text{IV-2}$$

where i is imaginary unit.

By calculation, it can be found that V_j could be expressed to the following form

$$V_j = x_j i + y_j \qquad \text{IV-3}$$

where x_j is the horizontal component of the displacement vector of particle j and y_j is the vertical component of the displacement vector of particle j.

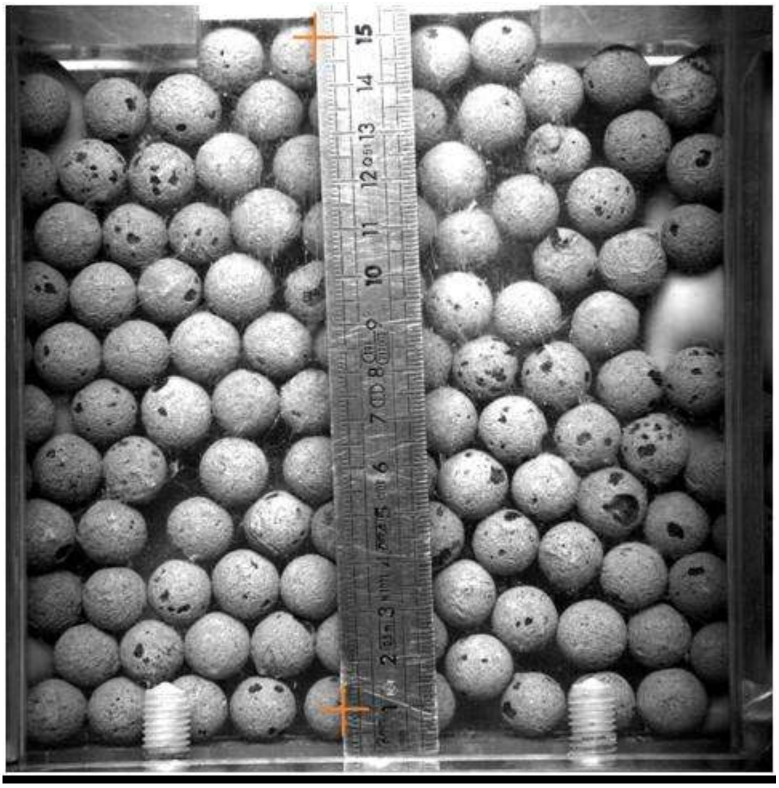

Fig IV-2 Scale Image of one of the tests

IV.3.Experimental results and discussion

IV.3.1.Load-displacement situation

According to the results obtained with the EMTM, curves describing the load-displacement change are plotted in Fig IV-3. It shows that at the beginning of tests, the load increases at a decreasing speed with the increase of the displacement. However there is a limit value for the load for each test according to different tests setting. After some fluctuations, the load will reach the maximum value and stop increasing although the displacement is still growing. At this time, the tests would be terminated manually. All the curves are not smooth because during the tests, individually, each particle shows a random character. When undertaking load, some particle might break which could lead to a sudden decline of the curve. Additionally, when the tests started, the original compact packing environments of the particles started to be interrupted and new environments were being generated. During this process, the movement of particles might be gradual. However, the particles also might translate or rotate suddenly which could result in fluctuation of the curves.

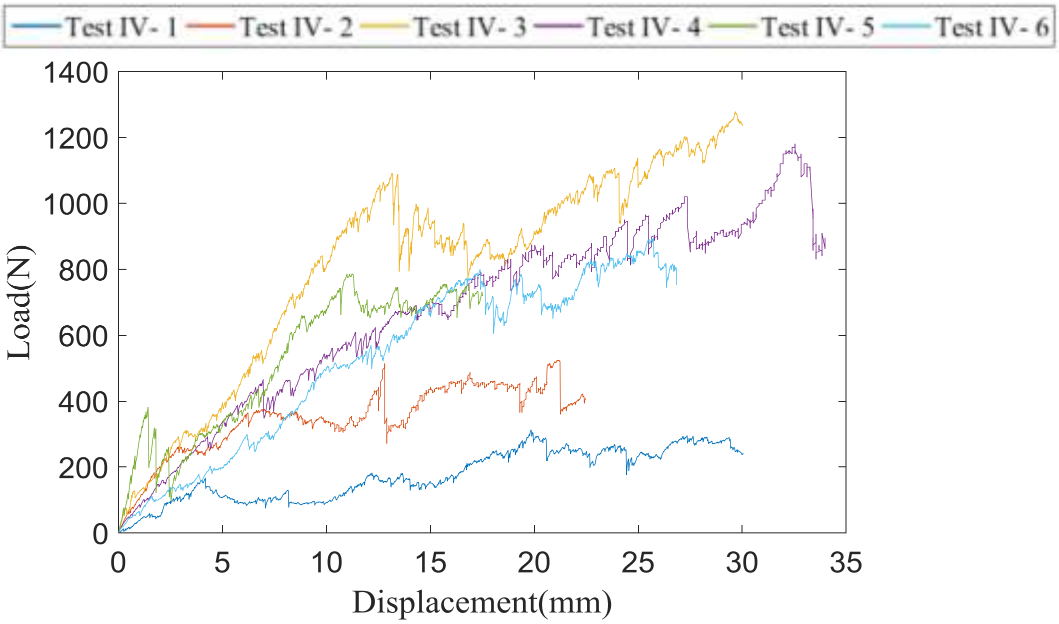

Fig IV-3 The load-displacement curve of the 6 tests

To make the load-displacement curve intuitive, all the curves are fitted to quadratic function passing through the origin.

$$f(x) = a_1 x^2 + a_2 x \tag{IV-4}$$

where a_1 and a_2 are two modulus. R^2, the coefficient of determination, is a statistic that describes the goodness of a fit curve to the real data. If y_i is the dependent variable of the original curve and is associated with a predicted value f_i on the fitted curve, defining the $\bar{y}$ as the mean value to the original data:

$$\bar{y} = \frac{1}{n}\sum_{i=1}^{n} y_i \tag{IV-5}$$

If *SST* is the sum of squares for total, *SSReg* is the sum of squares for regression, and *SSE* is the sum of squares for error,

$$SST = \sum_{i=1}^{n} (y_i - \bar{y})^2 \tag{IV-6}$$

$$SSReg = \sum_{i=1}^{n} (f_i - \bar{y})^2 \tag{IV-7}$$

$$SSE = \sum_{i=1}^{n} (y_i - f_i)^2 \tag{IV-8}$$

$$R^2 = 1 - \frac{SSE}{SST} = 1 - \sum_{i=1}^{n} (y_i - f_i)^2 \Big/ \sum_{i=1}^{n} (y_i - \bar{y})^2 \tag{IV-9}$$

Value of R^2 ranges from 0 to 1 and a value R^2 which equals 1 indicate that the regression line perfectly fits the data [144].

The a_1 a_2 and R^2 of the 6 fitted curves are shown in Table IV-2, Fig IV-5. The comparison of fitted curves and original curves are shown in Fig IV-5.

	Test IV-1	Test IV-2	Test IV-3	Test IV-4	Test IV-5	Test IV-6
a_1	-0.2286	-1.6862	-1.7135	-0.9082	-2.8520	-0.9108
a_2	15.9779	54.9532	87.4163	59.7518	91.2929	55.6048
R^2	0.8441	0.8630	0.9003	0.9675	0.9087	0.9720

Table IV-2 Parameters of the fitted curves

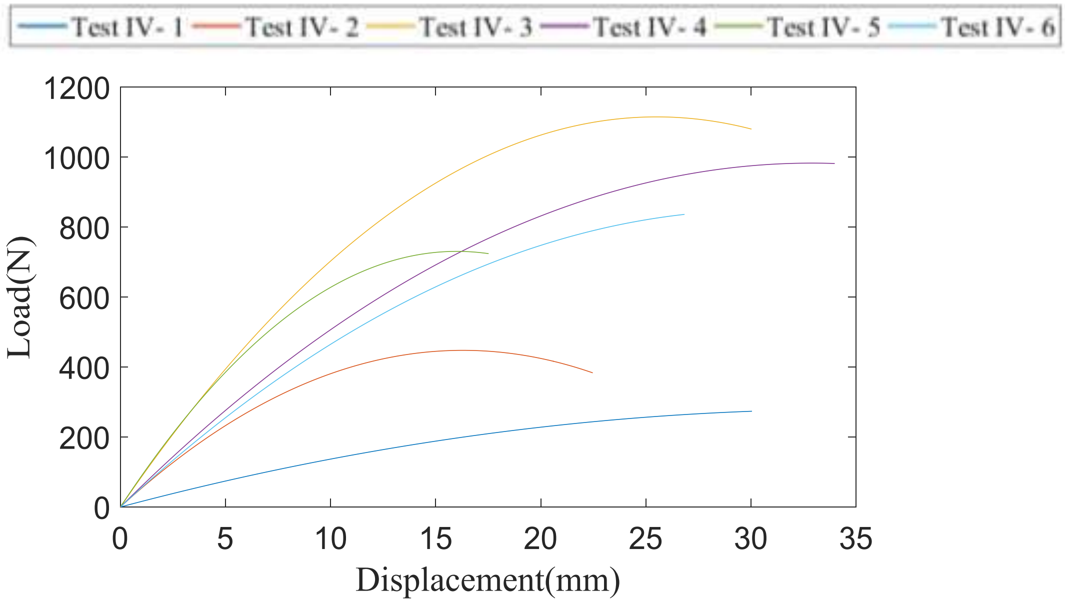

Fig IV-4 Fitted curves of load-displacement relationship

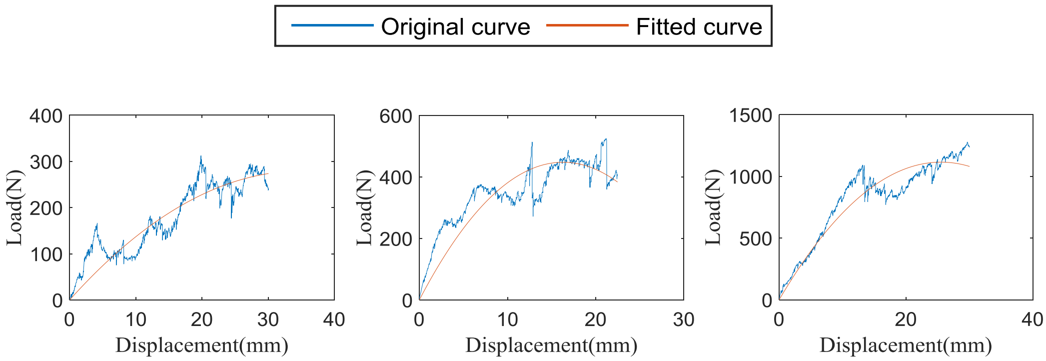

Test IV-1

Test IV-2

Test IV-3

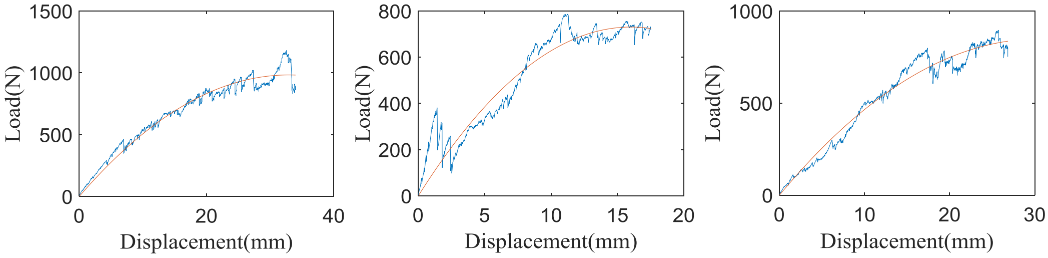

Test IV-4

Test IV-5

Test IV-6

Fig IV-5 Comparisons of fitted curves of and original curves

With the six tests, some kinds of comparison could be made to study the influence of four different test conditions to the results. Firstly, the influence of confining stress would be studied. Based on the results of Test IV-1 Test IV-2 and Test IV-3, the maximum values of load are 266.85N, 498.06N and 996.42N which basically met the relationship of 1:2:4. The above phenomenon could illustrate two points. Firstly, during the process of loading, the load could increase to a peak with the increase of displacement. Secondly, this creak load varies only depend on the confining pressure.

The load on the cover is resulted from the stress of the particles when compressed. Before the start of the tests, the stress is caused by the confining pressure, baring reaction and the weight of the particles. Since the particles are cohensionless and have a low fluidity due to frictions between particles, the confining stress and weight of particles and the supporting force from the container could keep balance of force. Besides, it would also lead to an initial stress of the particles. As the tests began, this balance would be broken, so particles will start to move and the cover would carry reactive force from the particles. Obviously, the reactive force on the cover and the stress of the particles are positively related. As the increase of displacement, the stress would increase, so the load increases. However, when the stress reached a certain limit, continued displacement would not lead to a further increase of the stress. Instead, the rubber bags which provided confining stress would shrink and keep a relative stability of the volume of the chamber and the stress. Therefore, through observing all the tests, the odd ratios of the ceiling of the loads could basically meet the ratios of confining stress. The only exceptions are Test IV-5 and Test IV-6. The reason is the cover of the chamber had been changed to big a one. Thus, with the same stress, the reactive forces are bigger than Test IV-3 and Test IV-4 which are with the some test conditions, correspond.

Another interesting point is the value of displacements which correspond to the maximum points of the loads. A comparison could be made between Test IV-3 and Test IV-4. It could be observed that, compared with monosized particles, polysized particles are later to reach the maximum points. The reason is that the polysized particles have a bigger void ratio than the monosized ones. Since the particles of all the tests are produced simultaneously, it could be believed that the mechanical behavior of each single particle is basically the same. As a result, the global Young's modulus of a cluster of particles depends on its void ratio. Therefore, for the polysized particles, the arrival at the maximum point of load needs a bigger displacement of the cover.

To conclude, the process of the phenomenon would be explained below. Before the application of vertical load, the cluster of particles was in force balance of gravity, confining pressure and reaction forces of the container. When applying vertical load, the reaction force of the cover would keep increasing with the increasing of the stress of particles and the volume of the chamber started to decrease. In the meanwhile, the rubber bags filled with water started to shrink. As the tests progress, the rate of the load decreased and the shrink rate of the rubber bags increase. Finally, continuing load would not result in a change of the volume of the chamber and would not cause an increase of stress. Meanwhile, the load on the cover reached a maximum value. During this process, some particles might fail which could also influence the results of the tests. The occurrences of distributions of particles failure will be introduced in the next part.

In Fig IV-3, it could be observed that, the load-displacement curve increased with a lot of fluctuations. In other words, the load increased with a lot drops. To study this, two moments in Test IV-3 would be examples for further investigations (Fig IV-6). The reason of selecting these two points is because the drops at these two moments are more obvious than the others.

Photos before and after the two moments could be seen in Fig IV-7 and Fig IV-8. Areas of changes are zoomed in to show the differences.

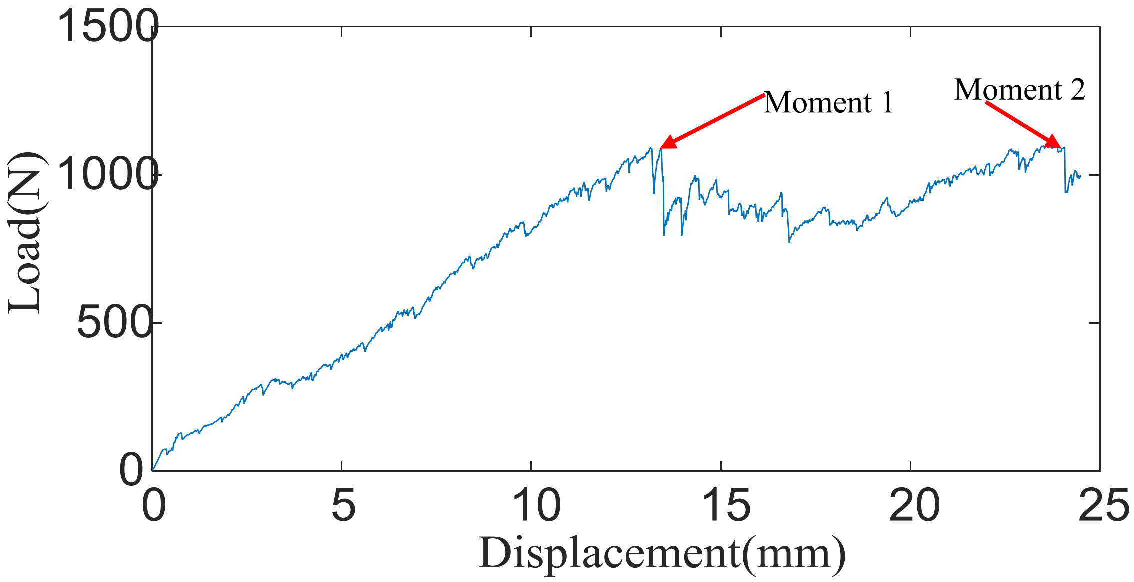

Fig IV-6 Tow moments of Test IV-3

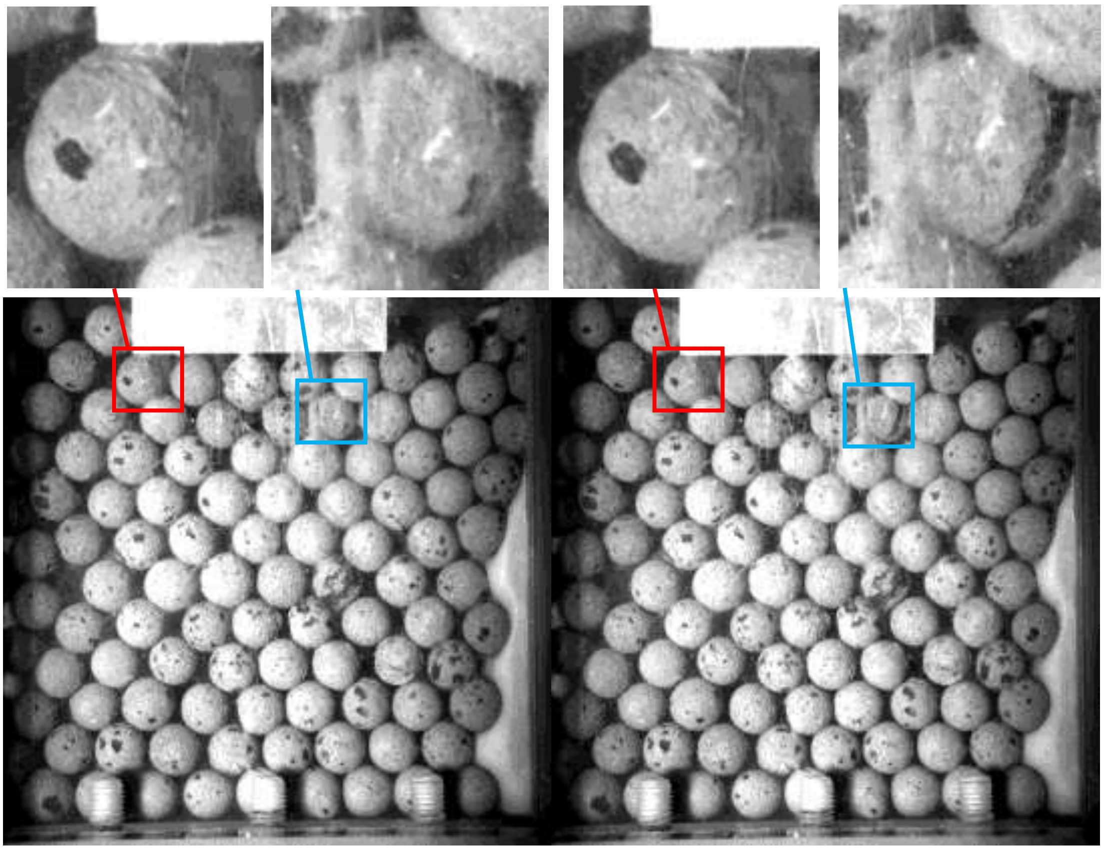

Before Moment 1

After Moment 1

Fig IV-7 Photos of TestIV-4 before and after Moment 1

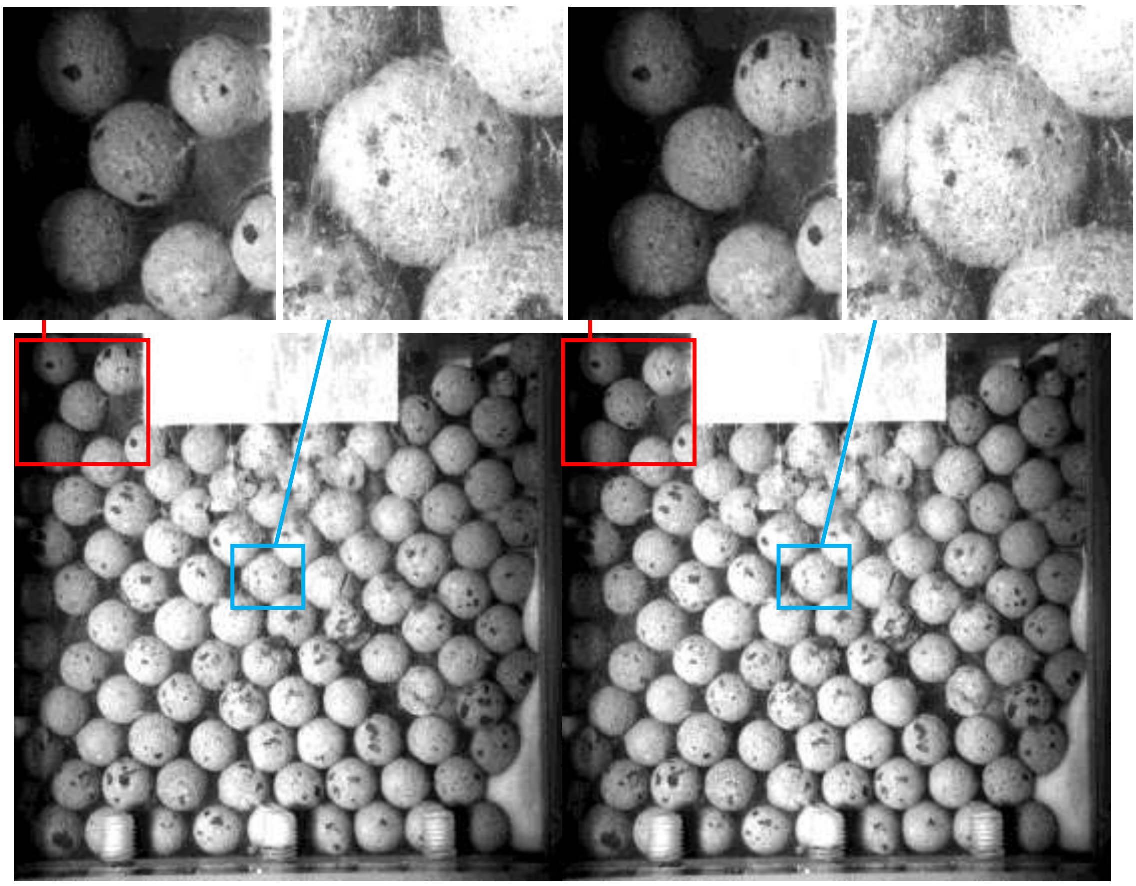

Before Moment 2 After Moment 2

Fig IV-8 Photos of TestIV-4 before and after Moment 2

In Fig IV-7, it could be observed that, for moment 1, two particles are mainly analyzed. At this moment, the two particles broke and the curve dropped a lot.

In Fig IV-8, it could be observed that for moment 2, a group of particles and a particle are mainly investigated. It could be seen that, at this moment, there is a movement and rotation of the group of particles in red rectangle. And for the particle in blue rectangle, a crack appeared.

Therefore, among all the particles, if one particle breaks or moves or rotates, the load would drop. If several particles break or have sudden displacement, the drop of the curve would be more dramatic.

IV.3.2.Particles breakage occurrences and distributions

Except for Test IV-1, it is observed that during the tests, some particles were fail. The orders and positions of particles failures are shown in Fig IV-9 and corresponding loads and displacements were presented in Table IV-3.

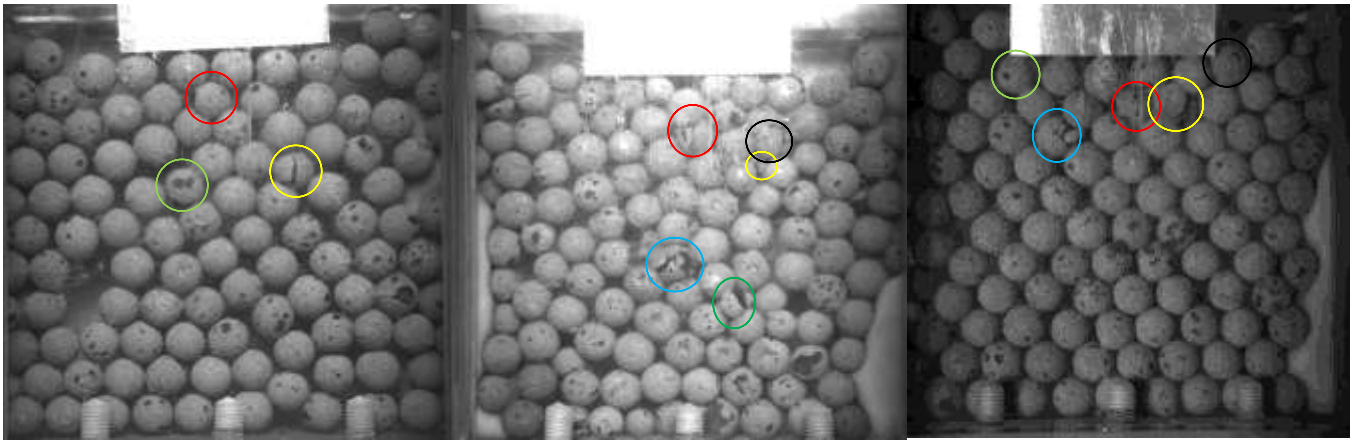

Test IV-2 Test IV-3 Test IV-4

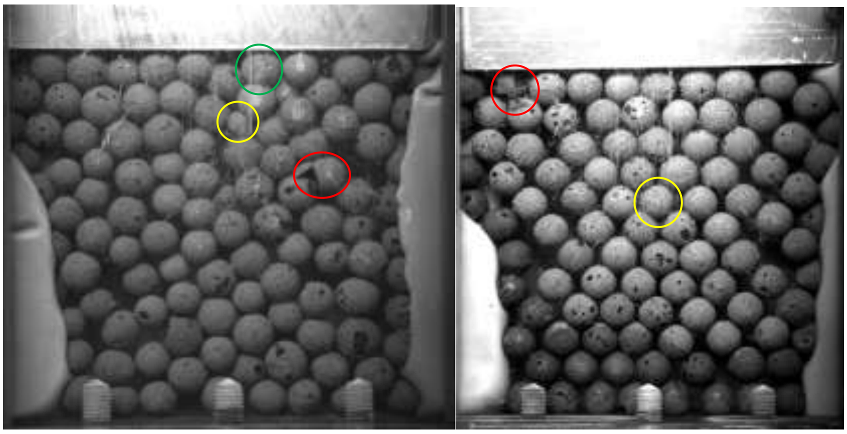

Test IV-5 Test IV-6

Order of failure:○ :First failure.○ :Second failure. ○:Third failure. ○Forth failure.

○ :Fifth failure

Fig IV-9 The order and position of particles failure

Breakage order		1	2	3	4	5
Test IV-2	L(N)	441.05	513.22	524.75		
	D(mm)	12.7	13.11	21.36		
Test IV-3	L(N)	725.14	1088.07	925.27	902.28	888.8
	D(mm)	8.58	8.75	13.14	14.67	16.11
Test IV-4	L(N)	732.98	685.94	844.57	849.68	942.53
	D(mm)	13.8	15.5	21.4	21.5	25.62
Test IV-5	L(N)	392.54	682.85			
	D(mm)	2.5	13.8			
Test IV-6	L(N)	522.56	646.58	785.59		
	D(mm)	12.2	18.3	23.4		

Table IV-3 Corresponding load and displacements of particle failure

D: Displacement; L: Load

Since in Test IV-1 no particle breakages appeared, the information of Test IV-1 is not mentioned in Fig IV-9 and Table IV-3. In Table IV-3, if there were more than five failures before the end of the tests, only the former five ones were counted. If the amount of failure was less than five, all failures were counted.

According to Test IV-1, no particle failure occurred. In Test IV-2, Test IV-5 and Test IV-6, two or three particles failed. In Test IV-3 and Test IV-4, as the tests process continued, a lot of particles failure occurred. The reason of this kind of difference is that the confining pressure. As explained in IV.3.1, the limit value of the stress of the particles has a positive relation with the confining pressure. When the stress of the particles reached the limit value, the continued vertical load would not cause an increase of the stress but the volume compression of the rubber bags. In other words, if a space occupied by particles could be imagined, at this stage, the height of the space would decrease and the length of this space could increase. Therefore, in the environment of bigger stress, the particles have larger probability to fail.

Moreover, another rule which can be observed is the locations of the failed particles. All the failed particles located on the middle upper parts of the chamber, indicating that particles which are close to the bottom of the chamber and the rubber bags would not fail. This is because with downward load from the cover, the triangular domain under the cover confronts the biggest compression.

From the macro point of view, the global mechanical behavior all particles could be treated as a kind of Morh-Coulomb material whose cohesion is very small.

The Mohr-Coulomb criterion is used to define shear strength of soil or rock at different effective stress. It assumes that yield occurs when the shear stress on any point in a material reaches a value which depends linearly on the normal stress in the same plane.

$$\tau = -\sigma \tan \phi + c \qquad \text{IV-10}$$

where τ is the shear strength, σ is the normal stress and negative in compression in the environment of Abaqus, *c* is the intercept of the failure envelope with the τ axis and is called cohesion, and *tan(ϕ)* is the slope of the failure envelope. ϕ is called the friction angle.

The Mohr-Coulomb model is based on plotting Mohr's circle for states of stress at yield in the plane of the maximum and minimum principal stresses. The yield line is the best straight line that touches these Mohr's circles (Fig IV-10).

From the Mohr’s circle,

$$\tau = s \cos \phi \qquad \text{IV-11}$$

$$\sigma = \sigma_m + s \sin \phi \tag{IV-12}$$

where

$$s = \frac{1}{2}(\sigma_1 - \sigma_3) \tag{IV-13}$$

$$\sigma_m = \frac{1}{2}(\sigma_1 + \sigma_3) \tag{IV-14}$$

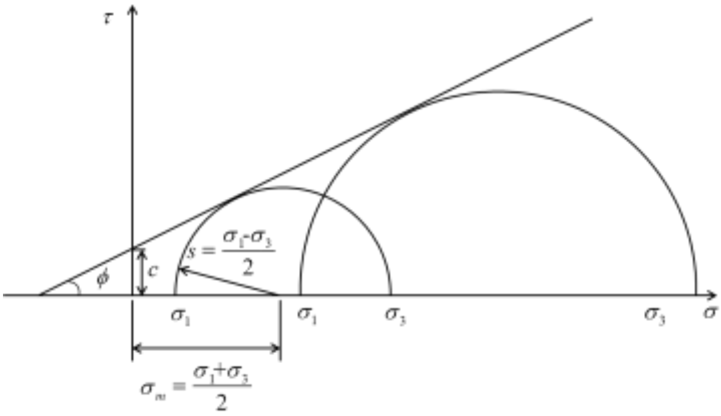

Fig IV-10 Mohr’s circle describing Mohr-Coulomb yield model

Two numerical models were built to show the stress distribution of the assembly of particles when influenced by vertical load. The two models were used to simulate the laboratory tests and the differences of the two models are the loading conditions. In model 1, the confining compression is 40kPa and the cover is the small cover. By contrast, in model 2, the confining compression is 20kPa and the top cover is the larger one. Besides, the results of maximum principle stress are shown in Fig IV-11.

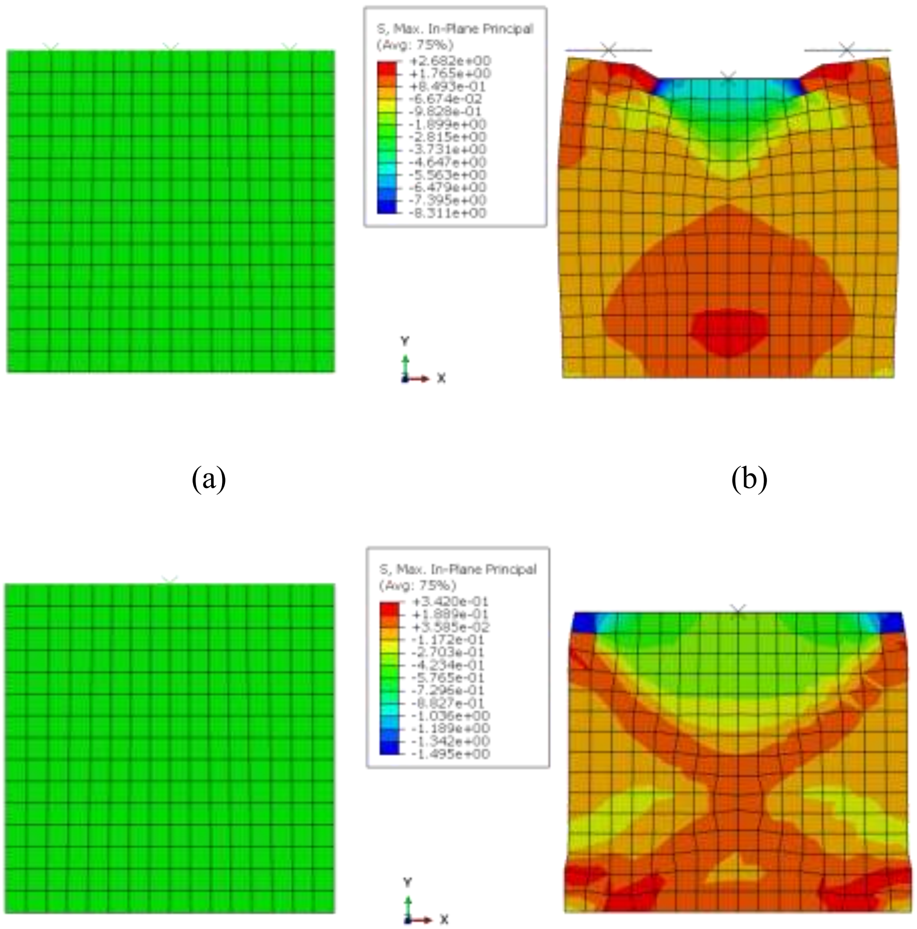

(a) (b)

(c) (d)

Fig IV-11 Maximum principle stress of Model 1 and Model 2 when the displacement of the cover is 15mm

(a): Original state of Model 1. (b): when displacement of the cover is 15mm of Model 1

(c): Original state of Model 2. (b): when displacement of the cover is 15mm of Model 2

In general, the increasing confining stress could make the particles have bigger stress. The triangular zones under the cover bare the biggest load. Therefore, the numbers and locations of the particles failures could be predicted. However, on the view of each particle, there are some uncertainties such as the material property, void location inside the particle, coordination of the particles. These uncertainties could also lead to an uncertainty of the specific order of the particle failure.

IV.3.3.Influence of particle failure to fabric of packing

In order to study the influence of particle breakage to the fabric of packing, the third and forth particle failures in Test IV-3 were selected for further analysis (Fig IV-9 and Table IV-3). These two particles were named as P-f3 and P-f4, respectively. The reason of selecting the two particles was that the locations of these two particles are lower than the other broken particles. Thus, more particles would be influence and bigger effect on the fabric of packing would be caused. The failure process of the two particles with their corresponding image number and displacement of top cover are shown in Fig IV-12.

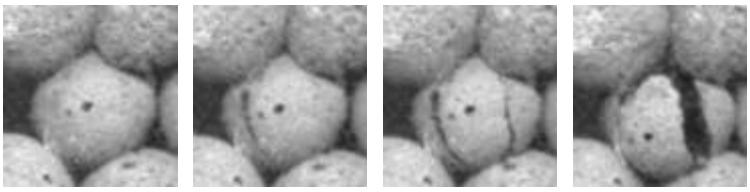

Image number	78	79	85	88
Displacement (mm):	13	13.17	14.17	14.67

(a)

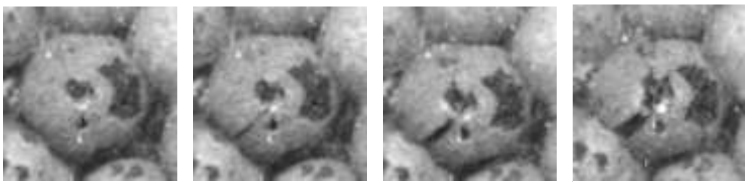

Image number:	86	87	96	99
Displacement (mm):	14.33	14.5	16	16.5

(b)

Fig IV-12 Failure process of two particles with corresponding image number and displacement of top cover (a): Failure process of P-f3. (b): Failure process of P-f4

It could be observed that, the breakage of P-f3 developed in two periods. In Image 79, a crack appeared and separated the particle to two sub-particles. The smaller one lost its baring capacity immediately however the bigger sub-particle continued baring load until Image 86 and another crack appeared. For P-f4, it failed in Image 87 and stopped carrying load.

Since a lot of particles were set in the PSC, the influence of the failure of one particle to the fabric of global packing behavior was too small to observe. Therefore, areas of interest were reduced to analyze the influence of particle failure to local packing behavior. The areas of interest are shown in Fig IV-13.

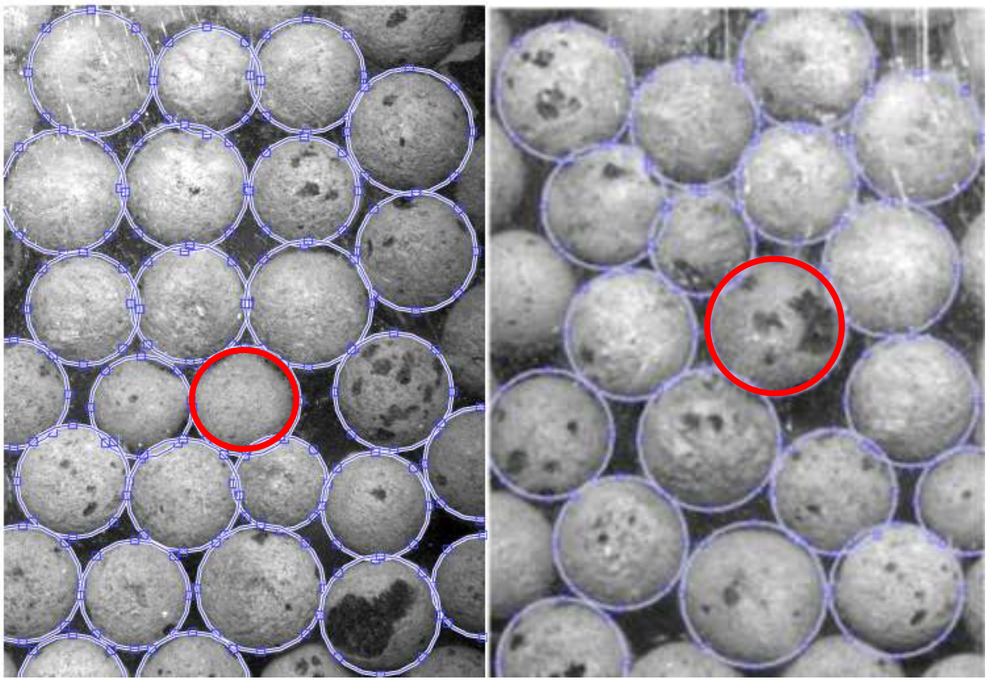

(a) (b)

Fig IV-13 Areas of interest (AOI) to analyze the influence of particle failure (a): P-f3 (b): P-f4

The evolution of coordination number and packing density in the AOI influenced by the particle failure is shown in Fig IV-14, Fig IV-15. It could be observed that, in the preliminary stage of the tests, without the influence of particle breakage, coordination number and packing density decrease slowly with some fluctuations. When the particle failure occurred on Image 78 of P-f3 and Image 86 of P-f4, there would be obvious drop on the coordination and packing density. After the particle failure, the coordination number and packing density continued decreasing at a bigger slope than before the particle failure. This phenomenon caused by two reasons. Firstly, the software identifies particles through searching circles in the image. When a crack appeared and separated a particle to two parts, the software would not judge the particle with a crack as a particle because it is not a circle any more. For the further calculation, this particle would be treated as void of particles collection. Secondly, the failure of one particle would make continues influence on the surrounding ones. In the structure with dense packing particles, every particle carries load. Thus, the failure of one particle could not lead to a collapse. Instead, the load it carries would be reassigned to other particles around it after a slight adjusting of the location of particles. For the rebuilt structure of particles, the coordination and the packing density drop faster under the influence of outside load.

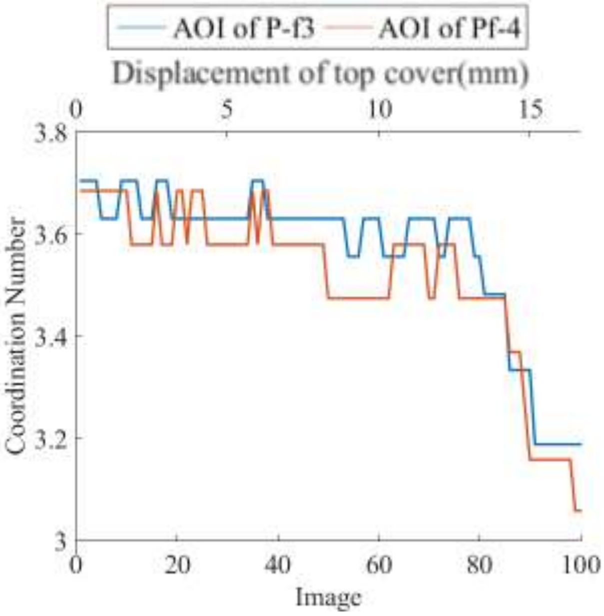

Fig IV-14Evolution of Coordination Number in the AOI

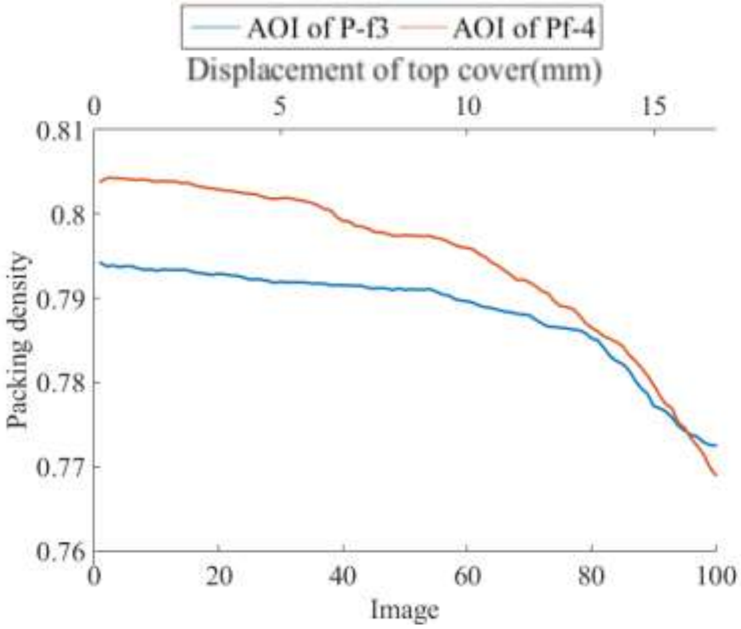

Fig IV-15 Evolution of Packing Density in the AOI

IV.3.4.Displacement analyze

As introduced in IV.2.2, all particles displacements vector could be analysed by the MATLAB code. For a certain particle *j,* its displacement vector could be expressed by

$$V_j = x_j i + y_j \qquad \text{IV-15}$$

If the whole 360° is divided into 24 zones averagely, each zone could contain 15°. If *m* is the number of a zone, the range of *m* is from 1 to 24. In zone *m*, there are *n* particles whose displacement directions are in this zone. In addition, a vector reflecting the mean of all particle displacement vectors in this zone would be calculated as

$$\overline{V_m} = \left(\sum_{j=1}^{n} x_j * i + \sum_{j=1}^{n} y_j\right)/n \qquad \text{IV-16}$$

When finishing calculation of $\overline{V_m}$ from *m=1* to *m=24*, the results of $\overline{V_m}$ of six tests at different time steps are shown in Table IV-4.

Image	Dis(mm)	Test IV-1	Test IV-2	Test IV-3	Test IV-4	Test IV-5	Test IV-6
10	10/6	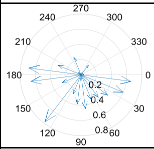	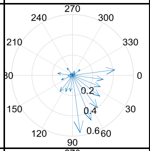	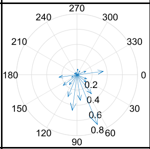	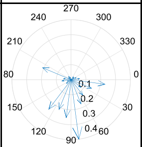	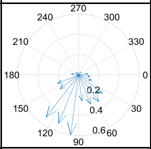	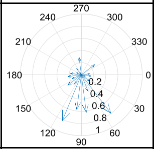
20	20/6	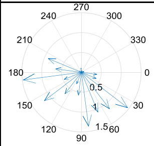	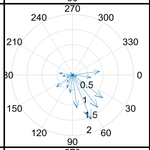	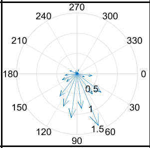	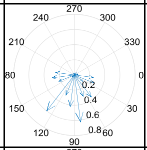	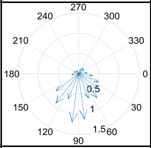	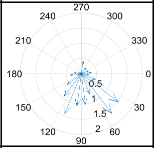
30	30/6	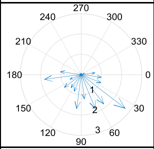	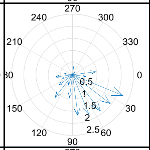	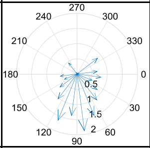	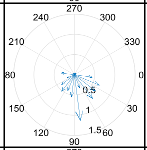	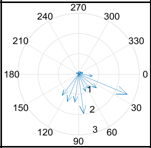	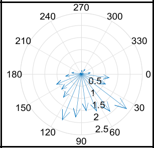
40	40/6	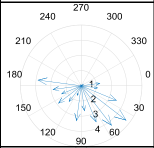	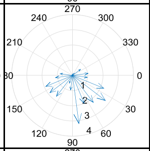	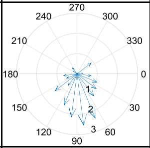	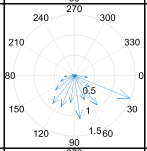	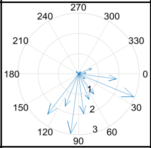	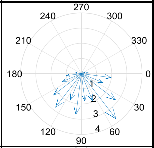
50	50/6	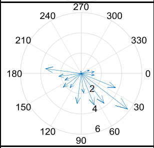	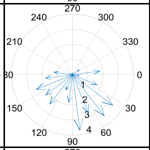	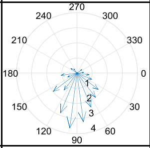	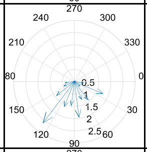	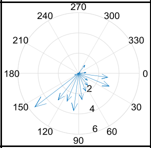	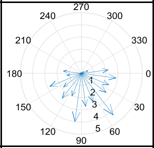
60	60/6	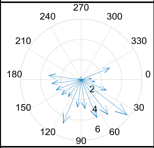	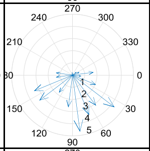	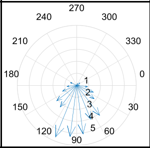	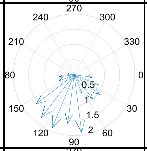	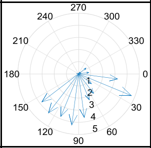	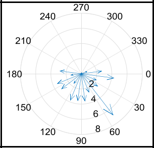
70	70/6	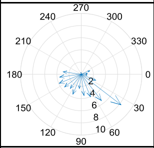	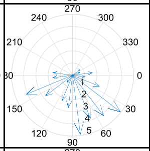	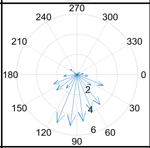	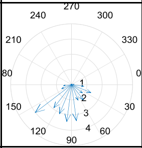	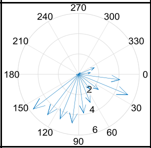	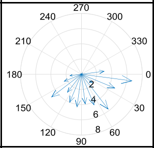
80	80/6	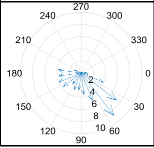	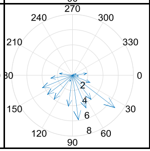	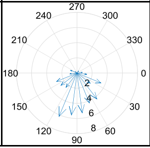	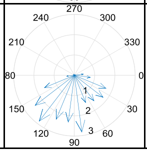	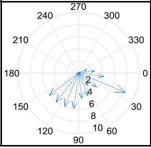	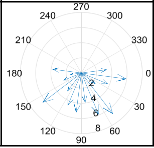

90	90/6	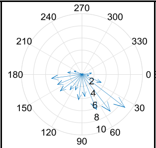	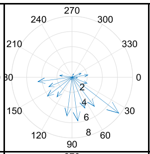	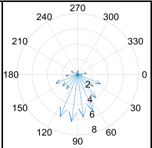	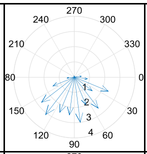	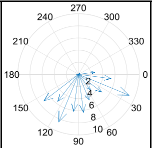	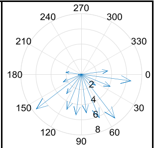
100	100/6	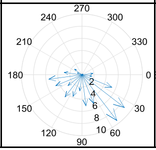	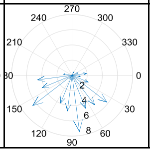	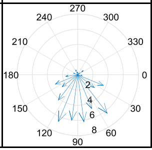	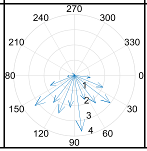	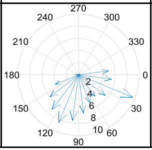	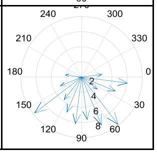

Table IV-4 The displacement vectors of the six tests

From the table, under the influence of downwards load, the direction of displacements of particles has some characteristics. At first, the particles move downwards in general. Meanwhile, since the disturbance effect of the cover of the PSC, particles also move to the two sides. To analyse the displacement characteristic in advance, some more calculations were performed. If there were l particles in one test, the vectorial sum of all displacement vectors of all particles could be calculated as

$$V_{sum} = \sum_{j=1}^{l} V_j = \sum_{j=1}^{l} x_j * i + \sum_{j=1}^{l} y_j \tag{IV-17}$$

The magnitude of V_{sum} is

$$|V_{sum}| = \sqrt{(\sum_{j=1}^{l} x_j)^2 + (\sum_{j=1}^{l} y_j)^2} \tag{IV-18}$$

The included angle of V_{sum} with straight down of the vertical direction is

$$\theta = \arctan\left(\sum_{j=1}^{l} y_j \Big/ \sum_{j=1}^{l} x_j\right) \tag{IV-19}$$

The results of V_{sum} and θ of the six tests at different time steps are shown in Fig IV-16 and Fig IV-17.

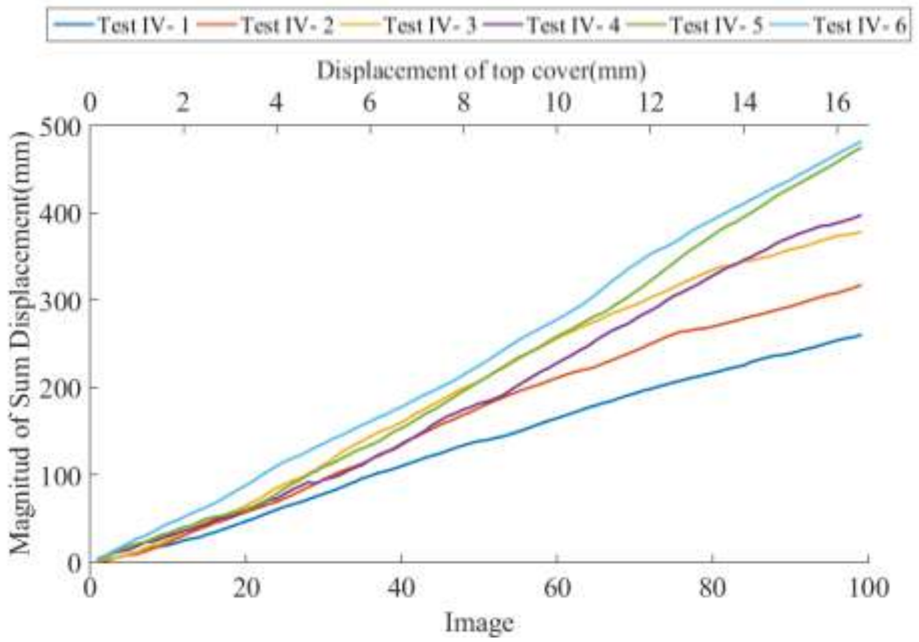

Fig IV-16 The magnitude of the sum displacement vectors

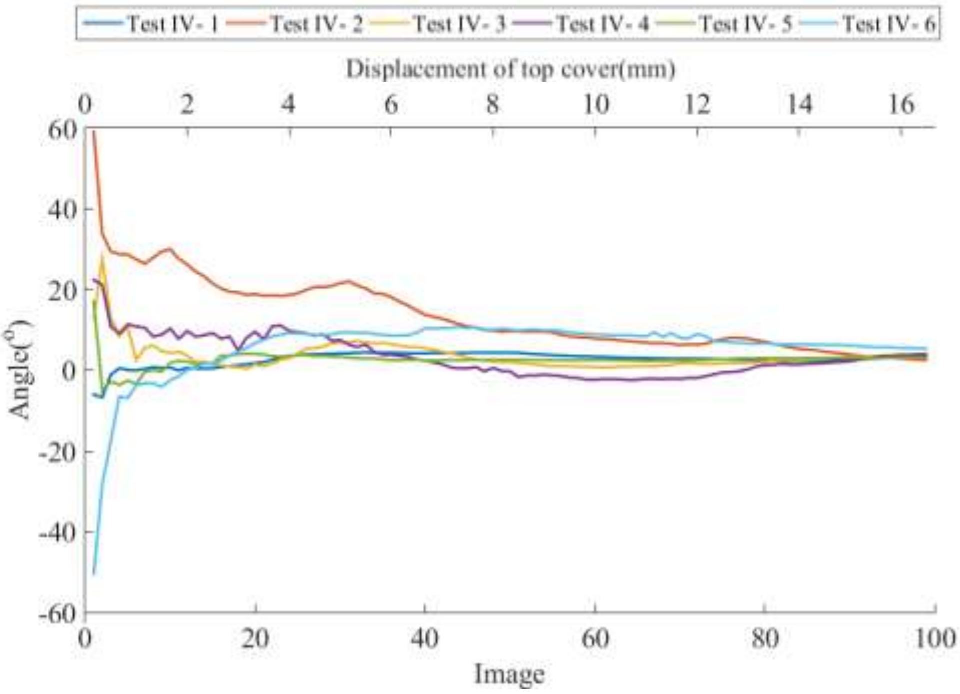

Fig IV-17 The included angle of the sum displacement vectors with the vertical direction

Fig IV-17 showed that at the beginning of the tests, the included angle of the sum displacement vectors with the vertical direction distributed disorderly. The reason is when accumulating the particles, it is difficult to ensure that particles located in the PSC totally evenly. Thus, under the disturbance of the cover, particles would move towards the zones which were comparably sparse at first. However, with the process of the tests, the allocation of the particle at different place of the PSC would become a balance under the effect of compaction. Therefore, the leftwards and rightwards horizontal displacement component of different particles could be offset in sum. Finally, the direction of the sum of displacement vector is almost vertical.

In Fig IV-16, it could be observed that the magnitudes of the sum displacement vectors increased through the tests. The values of the displacement magnitudes are not the same for different tests conditions. In Test IV-5 and Test IV-6, the magnitudes are larger than the others. It could be explained by the cover size. Particles have less space on the left or right sides if compressed with the large cover. Comparatively, in the other tests, with the small cover, particles could move to the left and right sides of the cover. For the tests with the small cover, it could be found that, with bigger confinement stress, the magnitude of the sum displacement vectors would be bigger. The reason is that with bigger lateral constraint, particles would have less possibility to move laterally. To verify this opinion, another calculation was performed. Besides, the displacement vectors of particles could be separated into horizontal component and vertical component. The mean of the absolute value of the horizontal component could be calculated as

$$\overline{|V_x|} = \frac{1}{N_p}\sum_{j=1}^{l}|x_j| \qquad \text{IV-20}$$

The results of $\overline{|V_x|}$ of six tests at different time steps are shown in Fig IV-18. It could be found that during the loading process, $\overline{|V_x|}$ increases with increasing displacement of the cover. If a comparison of different tests could be made, it could be found that, the confinement stress is a key factor influencing $\overline{|V_x|}$. The mean of the absolute value of the horizontal component of particles displacement vectors increase with the growing of the confinement stress.

The effect of horizontal component of particle displacement is leading to the real capacity of the PSC growing bigger. Thus particles would bare less stress. Comparing with Fig IV-9, it could be observed that, comparing different tests, with the increase of mean horizontal displacement, the number of particle failures decreased.

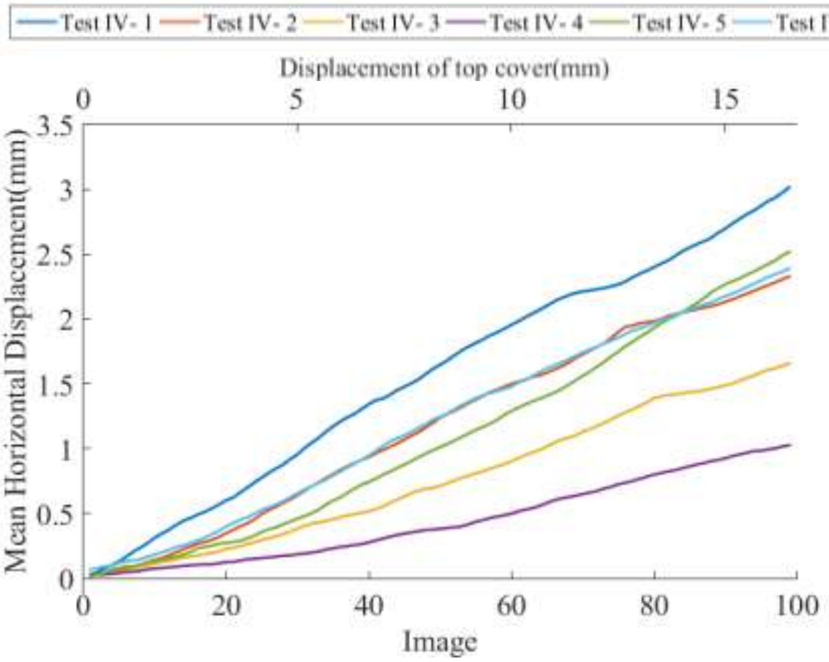

Fig IV-18 Mean of the absolute value of the horizontal component of particles displacement vectors

IV.4.Summary

This chapter aims to illustrate the mechanical and kinematical behavior of multiple particles when under vertical load. To achieve this goal, a Plane Strain Chamber (PSC) is used for the tests. Six biaxial compression tests were performed on spherical particles and photos were taken to record the experimental procedure. A series of MATLAB codes were written to calculate and analyze the photos. Finally, some conclusions could be drawn.

Two factors could cause an increase of the peak of the load with same displacement, the increasing of the size of the cover and the confining pressure. During the loading process, if the particles were submitted owing to the effect of load from the cover, gravity, confining pressure and baring reaction from the PSC. Consequently, a bigger contact area of the bigger cover could result in a bigger load. An increasing confining pressure could lead to an increasing stress, finally contributing to an increasing load. During the tests, the variation trend of the load is increasing. But if there is particle breakage or sudden particle movement or rotation, there would be a drop on the curve.

Secondly, following tests conditions, some particle may fail during tests. So an analysis had been made to understand the reason of particle failure. It has been concluded that, with a big confining pressure, the particles have large probability to fail because the increasing of the confining stress could lead to an increase of stress inside the particles. Moreover, particles located in the triangle zone under the cover had bigger stress and have bigger probability to fail. A failure of one particle would influence the packing of the surrounding ones. To be specific, it would lead to a decrease of coordination and packing density.

Thirdly, the displacement characteristic of particles when applying vertical load is also studied. The displacement vectors of all particles could be separated to vertical components and horizontal components. The directions of the horizontal components are towards the external of the particles assembly. Besides, the magnitudes of the horizontal components increase with the decrease of the confining pressure. Regarding the magnitude of the vertical component, the increasing of size of the cover and confining pressure could give rise to an increase of the magnitudes of the vertical components.

Chapter V. Conclusions and Perspectives

V.1.Conclusions

Uniaxial compression tests and biaxial compression tests have been carried out on single spherical particles and multi spherical particles. Besides, X-ray micro computed tomography technology has been used to obtain the 3D geometry of single particles. The reconstructed 3D geometry of particle has been imported into Abaqus to build a 3D geometry of the real particle. Results obtained with this model are compared with ideal particle. Photos were taken at constant interval to record the laboratory tests. In addition, software written with MATLAB code has been developed to analyze the photos from the aspect of packing fabric and mechanical and kinematical characteristic. Some conclusions have been drawn.

The uniaxial compression tests on single particles lead to particle failures. According to their emerging position, the failures of a spherical particle could be divided into two categories, respectively, failure from top and bottom and failure from the centre. For the failure from the top and bottom, it appeared from the beginning of the test. This type of failure could lead to the generation of two circular planes and is caused by tensile damage and compression damage. The tensile damage locates on the boundary of the circular plane from the beginning of the test. However, the appearance moment and location of compression damage is according to whether the particle is an ideal sphere. The compression damage appears when and where the compression equivalent plastic strain (PEEQ) reaches a certain value. If the particle is an ideal sphere, it appears at about ¼th of the radiuses below the contact surface with the loading machine. However, if the particle is not an ideal sphere, stress concentration caused by some defects may cause the PEEQ reaching the limit value in advance. Even, if there are some sharp protuberances at the surface of the particle, the compression damage may appear at the beginning of the test. For the second type of the failure, it appears just on the centre if the particle is a perfect sphere. Otherwise, it appears near the centre. This type of failure is caused by tensile damage. When the tensile equivalent plastic strain reaches the limit value, the failure appears and since then, it develops bigger gradually with the deformation of the particle. This process could not be observed from outside of the particle until the zone of the tensile damage reaches a certain volume. At the same time, some vertical cracks appear and separate the particle to several parts.

For the failure from the top and bottom, it is a local failure from the beginning to the end. However, for the failure from the centre, it is a local failure when it appears. As the test continues, it develops gradually but finally it could lead to a global failure.

If the particle has bigger coordination, the global failure occurs more quickly because the complex loading conditions could accelerate the evolution of the PEEQT at the centre of the particle.

The plane generated by the crack must bypass the centre of the particle and must be parallel to the direction of loading. Thus, for the particle only under load from vertical direction, the crack plane must be perpendicular to horizontal plane but it is impossible to foresee the detailed direction and appearing time of the crack plane. Besides, it is also possible to exist several crack planes which are perpendicular to horizontal plane and separate the particle to several parts. However, for the particle baring load from more than one direction, the direction of the crack plane will be parallel to the loading directions. If the normal of these loading directions is in one plane, the cracking plane of the particle could be virtually curtained.

During the preparation of the biaxial tests, after a vibrated filling process, the particles in our tests could almost reach each optimal packing status. The loading actions after this could not make the packing further denser. Instead, the perturbation of the cover could make the packing becoming looser. Moreover, due to the rubber bags on the left and right sides, the use of small cover could cause the junctions next to the cover and the rubber bags not close enough, and further leading to a looser packing density of the particles. But this effect disappeared gradually as the test went on. When the confining pressure is not very big, the increasing confining pressure could lead to a denser packing of particles. However, with the increase of confining pressure, the same pressure difference would result in smaller and smaller packing density difference.

In the biaxial compression tests, the packing densities of polysized particles are smaller than that of monosized particles. Because the diameter gaps between particles in different size are not big enough, the smaller particle could not fill the void between the larger ones. Instead, they would push apart the larger ones and give rise to a lower packing density. Besides, the packing on the upper parts and lower parts also have some differences. Briefly, the packing density on the upper part is smaller than that of lower part because of different vibration effect when filling the PSC and different perturbation effect of the cover during loading.

From the aspect of mechanical and kinematical behavior, other conclusions could be drawn with the biaxial tests. For the load-displacement curves, two factors could lead to an increase of the load with the same displacement, the size of the cover and the confining pressure. During the loading process, the stress among particles is the combined effect of load from the cover, gravity, confining pressure and baring reaction from the PSC. Thus, a bigger contact area of bigger cover could result in a bigger load. An increasing confining pressure could lead to an increasing stress of the particles and finally result in an increasing load on the cover from the loading system. During the tests, the variation trend of the load is increasing. But if there is particle breakage or sudden particle movement or rotation, there would be a drop on the curve. Moreover, under some certain condition, some particle may fail during the tests, so an analysis had been made on the reason of particle failure. It has been concluded that, with a big confining pressure, the particles have large probability to fail because the increasing confining stress could lead to an increase of stress on the particles. Moreover, particles located in the triangle zone under the cover have bigger probability to have bigger stress and have bigger probability to fail. Among a group of particles, a failure of one particle would influence the packing of the surrounding ones. To be specific, it would lead to a decrease of coordination and packing density.

In addition, the displacement characteristic of particles when applying vertical load is also studied. The displacement vectors of all particles could be separated to vertical components and horizontal components. Besides, the directions of the horizontal components are towards the external of the particles assembly. The magnitudes of the horizontal components increase with the decrease of the confining pressure. For the magnitude of the vertical component, the increasing size of the cover and confining pressure could cause an increase of the magnitudes of the vertical components.

V.2.Perspectives

Some improvement could be made on the experimental and analytical methods. At first, in our tests, the material used is a kind of spherical particles made by light expanded clays. This kind of study object is chosen because it is easy to observe. However, it is still far away from the common granular material which is needed in our daily life. Therefore, in future, it is better to make the study with material of practical application.

If other material is chosen, it is possible that, with the existing experimental apparatus, the tests could be conducted. If a kind of material with smaller volume, larger hardness and irregular geometry is chosen, the experimental apparatus need to be improved. For the multi particles tests, since a kind of particles with big volume is chosen, the number of particle in the PSC is small. This situation might lead to some uncertain influence during the tests and the effect of boundary is relative large. In future, tests with more particles should be conducted. Moreover, the front wall of the PSC should be changed to a new material which is more difficult to be scratched. In this case, the photo would be clearer to analyze.

Thirdly, for the analysis method, some improvement could be made. For example, to record the first-hand results, photos were treated as a tool. Then a code written by MATLAB distinguished the particles through comparing the gray level of each part of the pictures and then following calculation could be done. During this process, it is inevitable for some error range when judging the boundaries. This kind of error range could be caused by two reasons. The first reason is the photography technology and equipment, and the other reason is the image processing techniques. If the material with smaller volume and complex geometry would be used in future tests, the influence of this error range would become bigger. If some measures could be taken to eliminate the error range, it is believed that the results could be more accurate.

Lastly, in this thesis, Concrete Damaged Plastic model in the Abaqus environment is used for the analysis of single particle behavior. To analyse the behavior of multi particles, some more numerical methods could be tried such as BEM, DEM and F-DEM.

Reference

[1]. Duran, J. (2012). Sands, powders, and grains: an introduction to the physics of granular materials. Springer Science & Business Media.

[2]. Jaeger, H. M., Nagel, S. R., & Behringer, R. P. (1996). Granular solids, liquids, and gases.Reviews of modern physics, 68(4), 1259.

[3]. Hu W, Contribution to the scale effect of granular materials. Central University of Nantes, 2009

[4]. Radjai, F., Roux, J. N., & Daouadji, A. (2017). Modeling Granular Materials: Century-Long Research across Scales. Journal of Engineering Mechanics, 04017002.

[5]. Mitchell, J. K., & Soga, K. (2005). Fundamentals of soil behavior.

[6]. Yu, M. H. (2002). Advances in strength theories for materials under complex stress state in the 20th century. Applied Mechanics Reviews, 55(3), 169-218.

[7]. Hales, S. (1727). Vegetable Staticks: or, an account of some statical experiments on the Sap in Vegetables... Also, a specimen of an attempt to analyse the Air. W. & J. Innys.

[8]. Furnas, C. C. (1929). Flow of gases through beds of broken solids (Vol. 300). US Government Printing Office.

[9]. Jaeger, J. C. (1967, April). Failure of rocks under tensile conditions. In International Journal of Rock Mechanics and Mining Sciences & Geomechanics Abstracts (Vol. 4, No. 2, pp. 219-227). Pergamon.

[10]. Hardin B O. Crushing of soil particles [J]. Journal of Geotechnical Engineering ASCE, 1985, 111(10): 1177-1192.Yu, M. H. (2002). Advances in strength theories for materials under complex stress state in the 20th century. Applied Mechanics Reviews, 55(3), 169-218.

[11]. Lade P V, Yamamuro J A, Bopp P A. Significance of particle crushing in granular materials [J]. Journal of Geotechnical Engineering ASCE, 1996, 122(4): 309 –316.

[12]. Coop M R, Sorensen K K, Freitas T B, Georgoutsos G. Particle breakage during shearing of a carbonate sand [J]. Geotechnique, 2004, 54(3):157-163.

[13]. Yang Z X, Jardine R J, Zhu B T, Foray P, Tsuha C H C. Sand grain crushing and interface shearing during displacement pile installation in sand [J]. Geotechnique, 2010, 60(6): 469-482.

[14]. McDowell, G., Bolton, M. & Robertson, D. 1996. The fractal crushing of granular materials. Journal of the Mechanics and Physics of Solids (44): 2079–2101.

[15]. Lobo-Guerrero, S. 2006. Visualization of crushing evolution in granular materials under compression using DEM. International Journal of Geomechanics (6): 195–200.

[16]. Daouadji, A., Hicher, P. Y., & Rahma, A. (2001). An elastoplastic model for granular materials taking into account grain breakage. European Journal of Mechanics-A/Solids, 20(1), 113-137.

[17]. Daouadji, A., & Hicher, P. Y. (2010). An enhanced constitutive model for crushable granular materials. International journal for numerical and analytical methods in geomechanics, 34(6), 555-580.

[18]. Cheng, Y., Nakata, Y. & Bolton, M. 2008. Micro- and macro-mechanical bahavior of DEM crushable materials. Géotechnique (58): 471–480.

[19]. Miura, N., Murata, H. & Yasufuku, N. Stress-strain characteristics of sand in a particle-crushing region. Soils and Foundations (24): 77–89.

[20]. Golightly, C. R. (1990). Engineering properties of carbonate sands. Ph.D. dissertation, Bradford University

[21]. McDOWELLĆ, G. R., & BOLTONĆ, M. (1998). On the micromechanics of crushable aggregates.

[22]. Terzaghi, K., Peck, R. B., & Mesri, G. (1948). Soil mechanics in engineering practice. John Wiley & Sons.

[23]. Roberts, J. E. & de Souza, J. M. (1958). The compressibility of sand. Proc. Am. Soc. for Testing Mater. (ASTM) 58, 1269–1277.

[24]. Yoshimoto, N., Hyodo, M., Nakata, Y., Orense, R. P., Hongo, T., & Ohnaka, A. (2012). Evaluation of shear strength and mechanical properties of granulated coal ash based on single particle strength. Soils and Foundations, 52(2), 321-334.

[25]. Brown, E. T. (1981). International society on rock mechanics, suggested methods for rock characterization, testing and monitoring, ISRM suggested methods.

[26]. Li, D., & Wong, L. N. Y. (2013). The Brazilian disc test for rock mechanics applications: review and new insights. Rock mechanics and rock engineering, 46(2), 269-287.

[27]. Carneiro, F. L. L. B. (1943, September). A new method to determine the tensile strength of concrete. In Proceedings of the 5th meeting of the Brazilian Association for Technical Rules (pp. 126-129).

[28]. Mellor, M., & Hawkes, I. (1971). Measurement of tensile strength by diametral compression of discs and annuli. Engineering Geology, 5(3), 173-225.

[29]. Newman, D. A., & Bennett, D. G. (1990). The effect of specimen size and stress rate for the Brazilian test—a statistical analysis. Rock Mechanics and Rock Engineering, 23(2), 123-134.

[30]. McDowell, G. R. (2002). On the yielding and plastic compression of sand. Soils and foundations,42(1), 139-145.

[31]. Nakata, Y., Kato, Y., Hyodo, M., HYDE, A. F., & Murata, H. (2001). One-dimensional compression behaviour of uniformly graded sand related to single particle crushing strength. Soils and Foundations, 41(2), 39-51.

[32]. Cavarretta, I., Coop, M., & O'sullivan, C. (2010). The influence of particle characteristics on the behaviour of coarse grained soils. Géotechnique, 60(6), 413-423.

[33]. Salami, Y., Dano, C., & Hicher, P. Y. (2017). An experimental study on the influence of the coordination number on grain crushing. European Journal of Environmental and Civil Engineering, 1-17.

[34]. Tang, C. A., Xu, X. H., Kou, S. Q., Lindqvist, P. A., & Liu, H. Y. (2001). Numerical investigation of particle breakage as applied to mechanical crushing—part I: single-particle breakage. International journal of rock mechanics and mining sciences, 38(8), 1147-1162.

[35]. Cheng, Y. P., Nakata, Y., & Bolton, M. D. (2003). Discrete element simulation of crushable soil. Geotechnique, 53(7), 633-641.

[36]. Hossain, Z., Indraratna, B., Darve, F., & Thakur, P. K. (2007). DEM analysis of angular ballast breakage under cyclic loading. Geomechanics and Geoengineering: An International Journal, 2(3), 175-181.

[37]. McDowell, G. R., & Harireche, O. (2002). Discrete element modelling of soil particle fracture.GEOTECHNIQUE-LONDON-, 52(2), 131-136.

[38]. Cil, M. B., & Alshibli, K. A. (2012). 3D assessment of fracture of sand particles using discrete element method. Géotechnique Lett, 2(3), 161-166.

[39]. Yan, Y., Zhao, J., & Ji, S. (2015). Discrete element analysis of breakage of irregularly shaped railway ballast. Geomechanics and Geoengineering, 10(1), 1-9.

[40]. Sukumaran, B., & Ashmawy, A. K. (2001). Quantitative characterisation of the geometry of discret particles. Geotechnique, 51(7), 619-627.

[41]. Kh, A. B., Mirghasemi, A. A., & Mohammadi, S. (2011). Numerical simulation of particle breakage of angular particles using combined DEM and FEM. Powder Technology, 205(1), 15-29.

[42]. Ma, G., Zhou, W., & Chang, X. L. (2014). Modeling the particle breakage of rockfill materials with the cohesive crack model. Computers and Geotechnics, 61, 132-143.

[43]. Mahabadi, O. K., Lisjak, A., Munjiza, A., & Grasselli, G. (2012). Y-Geo: new combined finite-discrete element numerical code for geomechanical applications. International Journal of Geomechanics,12(6), 676-688.

[44]. Procopio, A. T., & Zavaliangos, A. (2005). Simulation of multi-axial compaction of granular media from loose to high relative densities. Journal of the Mechanics and Physics of Solids, 53(7), 1523-1551.

[45]. Harthong, B., Jérier, J. F., Dorémus, P., Imbault, D., & Donzé, F. V. (2009). Modeling of high-density compaction of granular materials by the discrete element method. International Journal of Solids and Structures, 46(18), 3357-3364.

[46]. Herman, G. T. (2009). Fundamentals of computerized tomography: image reconstruction from projections. Springer Science & Business Media.

[47]. Desrues, J., Chambon, R., Mokni, M., & Mazerolle, F. (1996). Void ratio evolution inside shear bands in triaxial sand specimens studied by computed tomography. Géotechnique, 46(3), 529-546.

[48]. Zhao, B., Wang, J., Coop, M. R., Viggiani, G., & Jiang, M. (2015). An investigation of single sand particle fracture using X-ray micro-tomography. Géotechnique, 65(8), 625-641.

[49]. Duan, J., Hu, C., & Chen, H. (2013). High-resolution micro-CT for morphologic and quantitative assessment of the sinusoid in human cavernous hemangioma of the liver. PLoS One, 8(1), e53507.

[50]. Druckrey, A. M., & Alshibli, K. A. (2016). 3D finite element modeling of sand particle fracture based on in situ X-Ray synchrotron imaging. International Journal for Numerical and Analytical Methods in Geomechanics, 40(1), 105-116.

[51]. Alshibli, K., Cil, M. B., Kenesei, P., & Lienert, U. (2013). Strain tensor determination of compressed individual silica sand particles using high-energy synchrotron diffraction. Granular matter, 15(5), 517-530.

[52]. Mitchell, J. K., & Soga, K. (2005). Fundamentals of soil behavior.

[53]. Oda, M. (1972). Initial fabrics and their relations to mechanical properties of granular material. Soils and foundations, 12(1), 17-36.

[54]. Arthur, J. R. F., & Phillips, A. B. (1975). Homogeneous and layered sand in triaxial compression.Geotechnique, 25(4), 799-815.

[55]. Oda, M., Nemat-Nasser, S., & Mehrabadi, M. M. (1982). A statistical study of fabric in a random assembly of spherical granules. International Journal for Numerical and analytical methods in Geomechanics, 6(1), 77-94.

[56]. Yu, A. B. (2002). DEM—An Effective Method for Particle Scale Research of Particulate Matter. InDiscrete Element Methods: Numerical Modeling of Discontinua (pp. 17-22).

[57]. Liu, L. F., Zhang, Z. P., & Yu, A. B. (1999). Dynamic simulation of the centripetal packing of mono-sized spheres. Physica A: Statistical Mechanics and its Applications, 268(3), 433-453.

[58]. McNaught, A. D., & McNaught, A. D. (1997). Compendium of chemical terminology (Vol. 1669). Oxford: Blackwell Science.

[59]. Salami, Y., Dano, C., & Hicher, P. Y. (2017). An experimental study on the influence of the coordination number on grain crushing. European Journal of Environmental and Civil Engineering, 1-17.

[60]. Jouannot-Chesney, P., Jernot, J. P., & Lantuéjoul, C. (2011). Practical determination of the coordination number in granular media. Image Analysis & Stereology, 25(1), 55-61.

[61]. Lochmann, K., Oger, L., & Stoyan, D. (2006). Statistical analysis of random sphere packings with variable radius distribution. Solid State Sciences, 8(12), 1397-1413.

[62]. Oda, M. (1977). Co-ordination number and its relation to shear strength of granular material. Soils and Foundations, 17(2), 29-42.

[63]. Fonseca, J., O'Sullivan, C., & Coop, M. R. (2010). Quantitative Description of Grain Contacts in a Locked Sand.

[64]. Wang, L. B., Frost, J. D., & Lai, J. S. (2001). Quantification of doublet vector distribution of granular materials. Journal of engineering mechanics, 127(7), 720-729.

[65]. Azéma, E., Radjai, F., Peyroux, R., & Saussine, G. (2007). Force transmission in a packing of pentagonal particles. Physical Review E, 76(1), 011301

[66]. Oda, M., Konishi, J., & Nemat-Nasser, S. (1980). Some experimentally based fundamental results on the mechanical behaviour of granular materials. Geotechnique, 30(4), 479-495.

[67]. Wang, Y. H., & Mok, C. M. (2008). Mechanisms of small-strain shear-modulus anisotropy in soils.Journal of geotechnical and geoenvironmental engineering, 134(10), 1516-1530.

[68]. Finney, J. L. (1970, November). Random packings and the structure of simple liquids. I. The geometry of random close packing. In Proceedings of the Royal Society of London A: Mathematical, Physical and Engineering Sciences (Vol. 319, No. 1539, pp. 479-493). The Royal Society.

[69]. Donev, A., Cisse, I., Sachs, D., Variano, E. A., Stillinger, F. H., Connelly, R., ... & Chaikin, P. M. (2004). Improving the density of jammed disordered packings using ellipsoids. Science, 303(5660), 990-993.

[70]. Baker, J., & Kudrolli, A. (2010). Maximum and minimum stable random packings of platonic solids.Physical Review E, 82(6), 061304.

[71]. Li, S., Zhao, J., Lu, P., & Xie, Y. (2010). Maximum packing densities of basic 3D objects. Chinese Science Bulletin, 55(2), 114-119.

[72]. Zhao, S., Zhang, N., Zhou, X., & Zhang, L. (2017). Particle shape effects on fabric of granular random packing. Powder Technology.

[73]. Deng, X. L., & Davé, R. N. (2013). Dynamic simulation of particle packing influenced by size, aspect ratio and surface energy. Granular Matter, 15(4), 401-415.

[74]. Nan, W., Wang, Y., Ge, Y., & Wang, J. (2014). Effect of shape parameters of fiber on the packing structure. Powder Technology, 261, 210-218.

[75]. Abreu, C. R., Tavares, F. W., & Castier, M. (2003). Influence of particle shape on the packing and on the segregation of spherocylinders via Monte Carlo simulations. Powder Technology, 134(1), 167-180.

[76]. Fu, G., & Dekelbab, W. (2003). 3-D random packing of polydisperse particles and concrete aggregate grading. Powder Technology, 133(1), 147-155.

[77]. Kong, C. M., & Lannutti, J. J. (2000). Effect of agglomerate size distribution on loose packing fraction. Journal of the American Ceramic Society, 83(9), 2183-2188

[78]. Berryman, J. G. (1983). Random close packing of hard spheres and disks. Physical Review A,27(2), 1053.

[79]. Zhang, H. P., & Makse, H. A. (2005). Jamming transition in emulsions and granular materials.Physical Review E, 72(1), 011301.

[80]. Yen, K. Z. Y., & Chaki, T. K. (1992). A dynamic simulation of particle rearrangement in powder packings with realistic interactions. Journal of Applied Physics, 71(7), 3164-3173

[81]. Dong, K. J., Yang, R. Y., Zou, R. P., & Yu, A. B. (2006). Role of interparticle forces in the formation of random loose packing. Physical review letters, 96(14), 145505.

[82]. Wong, H. H., & Kwan, A. K. (2005, May). Packing density: a key concept for mix design of high performance concrete. In Proceedings of the materials science and technology in engineering conference, HKIE materials division, Hong Kong (pp. 1-15).

[83]. De Larrard, F. (1999). Concrete mixture proportioning: a scientific approach. CRC Press.

[84]. Dupuy, L., Fourcaud, T., & Stokes, A. (2005). A numerical investigation into the influence of soil type and root architecture on tree anchorage. Plant and Soil, 278(1), 119-134.

[85]. Zhang, Z. P., Liu, L. F., Yuan, Y. D., & Yu, A. B. (2001). A simulation study of the effects of dynamic variables on the packing of spheres. Powder Technology, 116(1), 23-32.

[86]. Silbert, L. E., Ertaş, D., Grest, G. S., Halsey, T. C., & Levine, D. (2002). Geometry of frictionless and frictional sphere packings. Physical Review E, 65(3), 031304.

[87]. An, X. Z., Yang, R. Y., Dong, K. J., Zou, R. P., & Yu, A. B. (2005). Micromechanical simulation and analysis of one-dimensional vibratory sphere packing. Physical review letters, 95(20), 205502.

[88]. Casagrande, A. (1925). Characteristics of cohesionless soils affecting the stability of earth fills, J. Boston Soc. Civil Eng. Contributions to Soil Mech, 1940, 1936.

[89]. Ning, Z., Khoubani, A., & Evans, T. M. (2017). Particulate modeling of cementation effects on small and large strain behaviors in granular material. Granular Matter, 19(1), 7.

[90]. *Rothenburg, L., & Kruyt, N. P. (2004). Critical state and evolution of coordination number in simulated granular materials. International Journal of Solids and Structures, 41(21), 5763-5774*

[91]. *Timoshenko, S. (1953). History of strength of materials: with a brief account of the history of theory of elasticity and theory of structures. Courier Corporation.*

[92]. *Terzaghi, K. (1943). Theory of consolidation (pp. 265-296). John Wiley & Sons, Inc.*

[93]. *Wadell, H. 1932. "Volume, shape, and roundness of rock particles." J. Geol., 40, 443–451.*

[94]. *Krumbein, W. C. 1941. "Measurement and geological significance of shape and roundness of sedimentary particles." J. Sediment. Petrol., 112, 64–72.*

[95]. *Cho, G. C., Dodds, J., & Santamarina, J. C. (2006). Particle Shape Effects on Packing Density, Stiffness, and Strength: Natural and Crushed Sands. JOURNAL OF GEOTECHNICAL AND GEOENVIRONMENTAL ENGINEERING, 591.*

[96]. *Ashmawy, A. K., Hoang, V. V., & Sukumaran, B. (2003, January). Evaluating the influence of particle shape on liquefaction behavior using discrete element modeling. In The Thirteenth International Offshore and Polar Engineering Conference. International Society of Offshore and Polar Engineers.*

[97]. *Maeda, K., Sakai, H., Kondo, A., Yamaguchi, T., Fukuma, M., & Nukudani, E. (2010). Stress-chain based micromechanics of sand with grain shape effect. Granular Matter, 12(5), 499-505.*

[98]. *Igwe, O., Sassa, K., & Wang, F. (2007). The influence of grading on the shear strength of loose sands in stress-controlled ring shear tests. Landslides, 4(1), 43.*

[99]. *Wood, D. M., & Maeda, K. (2008). Changing grading of soil: effect on critical states. Acta Geotechnica, 3(1), 3.*

[100]. *Bandini, V., & COOP, M. R. (2011). The influence of particle breakage on the location of the critical state line of sands. Soils and foundations, 51(4), 591-600.*

[101]. *Roberts, J. E., & De Souza, J. M. (1958). The compressibility of sands. Massachusetts Institute of Technology.*

[102]. *de Bono, J. P., McDowell, G. R., & Wanatowski, D. (2014). DEM of triaxial tests on crushable cemented sand. Granular Matter, 16(4), 563-572.*

[103]. *Billam, J. (1972). Some aspects of the behaviour of granular materials at high pressures. In Stress-Strain behaviour of Soils, Proc. of the Roscoe Memorial Symp. (pp. 69-80).*

[104]. *Lo, K. Y., & RoY, M. A. R. I. U. S. (1973). Response of particulate materials at high pressures. Soils and Foundations, 13(1), 61-76.*

[105]. *Yamamuro, J. A., & Lade, P. V. (1996). Drained sand behavior in axisymmetric tests at high pressures. Journal of Geotechnical Engineering, 122(2), 109-119.*

[106]. *Yamamuro, J. A., & Lade, P. V. (1993). Effects of strain rate on instability of granular soils.*

[107]. *Santamarina, J. C., & Cho, G. C. (2004, March). Soil behaviour: the role of particle shape. InAdvances in geotechnical engineering: The skempton conference (Vol. 1, pp. 604-617). Thomas Telford, London.*

[108]. *Afshar, T., Disfani, M. M., Arulrajah, A., Narsilio, G. A., & Emam, S. (2017). Impact of particle shape on breakage of recycled construction and demolition aggregates. Powder Technology, 308, 1-12.*

[109]. *Marsal, R. J. (1965). Discussion of shear strength. In Proc. 6th International Conference on Soil Mechanics and Foundation Engineering, Montreal (Vol. 3, pp. 310-316).*

[110]. *Hardin, B. O. (1985). Crushing of soil particles. Journal of Geotechnical Engineering, 111(10), 1177-1192.*

[111]. *Rozenblat, Y., Portnikov, D., Levy, A., Kalman, H., Aman, S., & Tomas, J. (2011). Strength distribution of particles under compression. Powder technology, 208(1), 215-224.*

[112]. *Indraratna, B., Sun, Q. D., & Nimbalkar, S. (2014). Observed and predicted behaviour of rail ballast under monotonic loading capturing particle breakage. Canadian geotechnical journal, 52(1), 73-86.*

[113]. Thakur, P. K. (2011). Cyclic densification of ballast and associated deformation and degradation.

[114]. Lackenby, J., Indraratna, B., McDowell, G., & Christie, D. (2007). Effect of confining pressure on ballast degradation and deformation under cyclic triaxial loading.

[115]. Cheng, Y. P., Bolton, M. D., & Nakata, Y. (2005). Grain crushing and critical states observed in DEM simulations. P&G05, 2, 1393-1397.

[116]. Kou, S. Q., Liu, H. Y., Lindqvist, P. A., Tang, C. A., & Xu, X. H. (2001). Numerical investigation of particle breakage as applied to mechanical crushing—Part II: Interparticle breakage. International Journal of Rock Mechanics and Mining Sciences, 38(8), 1163-1172.

[117]. Fukumoto, T. (1992). Particle breakage characteristics of granular soils. Soils and foundations,32(1), 26-40.

[118]. FUKUMOTO, T. (1990). A grading equation for decomposed granite soil. Soils and Foundations,30(1), 27-34.

[119]. Einav, I. (2007). Breakage mechanics—part I: theory. Journal of the Mechanics and Physics of Solids, 55(6), 1274-1297.

[120]. Einav, I. (2007). Breakage mechanics—Part II: Modelling granular materials. Journal of the Mechanics and Physics of Solids, 55(6), 1298-1320.

[121]. Selig, E. T., & Waters, J. M. (1994). Track geotechnology and substructure management. Thomas Telford.

[122]. Ueng, T. S., & Chen, T. J. (2000). Energy aspects of particle breakage in drained shear of sands.Geotechnique, 50(1), 65-72.

[123]. Indraratna, B., & Salim, W. (2002). Modelling of particle breakage of coarse aggregates incorporating strength and dilatancy. Taylor, D. W. (1948). Fundamentals of soil mechanics (Vol. 66, No. 2, p. 161). LWW.

[124]. Hicher, P. Y., & Rahma, A. (1994). Micro-macro correlations for granular media. Application to the modelling of sands. EUROPEAN JOURNAL OF MECHANICS SERIES A SOLIDS, 13, 763-763.

[125]. Salim, W., & Indraratna, B. (2004). A new elastoplastic constitutive model for coarse granular aggregates incorporating particle breakage. Canadian Geotechnical Journal, 41(4), 657-671.

[126]. Russell, A. R., & Khalili, N. (2004). A bounding surface plasticity model for sands exhibiting particle crushing. Canadian Geotechnical Journal, 41(6), 1179-1192.

[127]. Chávez, C., & Alonso, E. E. (2003). A constitutive model for crushed granular aggregates which includes suction effects. Soils and Foundations, 43(4), 215-227.

[128]. Liu, H., & Ling, H. I. (2008). Constitutive description of interface behavior including cyclic loading and particle breakage within the framework of critical state soil mechanics. International journal for numerical and analytical methods in geomechanics, 32(12), 1495-1514.

[129]. Hu, W., Yin, Z., Dano, C., & Hicher, P. Y. (2011). A constitutive model for granular materials considering grain breakage. Science China Technological Sciences, 54(8), 2188-2196.

[130]. Daouadji, A., Hicher, P. Y., & Rahma, A. (2001). An elastoplastic model for granular materials taking into account grain breakage. European Journal of Mechanics-A/Solids, 20(1), 113-137.

[131]. Daouadji, A., & Hicher, P. Y. (2010). An enhanced constitutive model for crushable granular materials. International journal for numerical and analytical methods in geomechanics, 34(6), 555-580.

[132]. Marshall, E. A. (1967). The compression of a slab of ideal soil between rough plates. Acta Mechanica, 3(2), 82-92.

[133]. Hofmann, H., Babadagli, T., Yoon, J. S., Zang, A., & Zimmermann, G. (2015). A grain based modeling study of mineralogical factors affecting strength, elastic behavior and micro fracture development during compression tests in granites. Engineering Fracture Mechanics, 147, 261-275.

[134]. Guimaraes, M., Valdes, J., Palomino, A. & Santamarina, J. 2007.Aggregate production: Fines generation during rock crushing. International Journal of Mineral Processing (81): 237–247.

[135]. Feldkamp, L. A., Davis, L. C., & Kress, J. W. (1984). Practical cone-beam algorithm. JOSA A, 1(6), 612-619.

[136]. Lee, J., and G. L. Fenves, "Plastic-Damage Model for Cyclic Loading of Concrete Structures," Journal of Engineering Mechanics, vol. 124, no.8, pp. 892–900, 1998.

[137]. Lubliner, J., J. Oliver, S. Oller, and E. Oñate, "A Plastic-Damage Model for Concrete," International Journal of Solids and Structures, vol. 25, pp. 299–329, 1989.

[138]. Budeshtskii, R. I. (1971). Mathematical model of granular composite materials. Strength of Materials, 3(8), 912-916.

[139]. Wang, P. J., Xia, J. H., Li, Y. D., & Liu, C. S. (2007). Crossover in the power-law behavior of confined energy in a composite granular chain. Physical Review E, 76(4), 041305.

[140]. Lubachevsky, B. D., & Stillinger, F. H. (1990). Geometric properties of random disk packings.Journal of statistical Physics, 60(5-6), 561-583.

[141]. Roth, L. K., & Jaeger, H. M. (2016). Optimizing packing fraction in granular media composed of overlapping spheres. Soft matter, 12(4), 1107-1115.

[142]. Zhu, H. P., Zhou, Z. Y., Yang, R. Y., & Yu, A. B. (2008). Discrete particle simulation of particulate systems: a review of major applications and findings. Chemical Engineering Science, 63(23), 5728-5770.

[143]. Yuen, H. K., Princen, J., Illingworth, J., & Kittler, J. (1990). Comparative study of Hough transform methods for circle finding. Image and vision computing, 8(1), 71-77.

[144]. Devore, J. L. (2011). Probability and Statistics for Engineering and the Sciences. Cengage learning.

Abstract

The mechanical behaviour of granular materials is deeply related to both the individual particle properties and to the assembly of grains (fabric, void distribution …). Subjected to an external loading, the assembly deforms which is not only dependent on relative grain displacements but also on the grain deformation and to grain breakage when occurring.

Experimental and numerical studies of single particles were performed. Four approximately spherical particles of light expanded clay were tested to investigate the breakage phenomenon under diametric displacement-controlled compression load. Photos were taken with a frame rate of 4 images per second during the testing. Since the interior of a heterogeneous particle has significant influence on the failure initiation, an X-Ray micro tomography system was used to scan particles. Moreover, the post-processing enables us to obtain the real 3D volumetric structure. Then a 3D numerical model including pore structure was built in Abaqus for the same loading conditions. A comparison of results from laboratory tests and simulations was made. Based on the results, the crack initiation process, its location and classification of particle failures were set.

For purpose of understanding the anisotropy and in particular fabric of packing of granular material when disturbed under external loading, five biaxial compression tests were performed on an assembly of approximately spherical particles settled in a chamber under confining pressure. During the test, photos were taken by the camera and saved to a computer at periodic intervals. Software written with Matlab codes was used to process the photos, determine the displacement field and analyse the results. Focus on contact orientation, fabric tensor and its evolution during testing were put on. Impact of some key factors such as packing density, confining pressure, sizes of the covers, sizes of the particles and thickness of samples on the packing characteristic were analysed.

In order to understand mechanical behaviour and kinematic of multiple particles under external load considering particle breakage, six biaxial compression tests were performed on an assembly of approximately spherical particles. Photos were taken to record the location of each particle during the tests. Software written with of Matlab codes was used to process the photos and trace the displacement of all particles in order to analyze kinematical behaviour of the particles. A particular attention was payed to given particles subjected grain breakage within the assembly. Their contacts and relative displacements were introduced in the numerical model of single grain breakage and conclusions were derived.

Key words: granular material; particle breakage; packing density; anisotropy; uniaxial and biaxial compression tests.

Résumé

Le comportement mécanique de matériaux granulaires est intrinsèquement lié aux propriétés individuelles des grains constitutifs ainsi qu'à leur assemblage (texture, distribution des vides, contact entre grains…). Soumis à un chargement extérieur, cet assemblage se déforme incluant le déplacement relatif entre les particules mais également la déformation propre des grains jusqu'à leur rupture si elle se produit.

Pour étudier la rupture d'une seule particule, des études expérimentales et numériques ont été réalisées. Quatre particules sphériques formées de billes d'argile expansée légère ont été testées en compression à déplacement contrôlé jusqu'à la rupture (essai brésilien). Des photos ont été prises avec une fréquence d'acquisition de 4 images par seconde pour suivre la déformation des grains durant l'essai. La structure interne d'une particule a une influence significative sur l'initiation de la fissure. Pour approfondir cet effet, une micro-tomographie par rayons X a été utilisé pour scanner une particule afin d'obtenir la structure géométrique réelle en 3D. Ensuite, un modèle numérique 3D basé sur la géométrie des particules incluant la porosité interne a été construit avec Abaqus pour les mêmes conditions de chargement. Une comparaison des résultats des tests de laboratoire et des simulations a été faite. Sur la base des résultats, l'initiation des fissures, leur localisation dans le grain et la classification des ruptures de particules ont été établies.

Afin d'étudier le rôle de l'anisotropie et en particulier de la fabrique d'un matériau granulaire soumis à un chargement externe, cinq essais de compression biaxiaux ont été réalisé sur un assemblage de grains quai-sphériques placés dans une chambre confinée.

Des photos ont été prises pendant les tests et ont été enregistrées selon une fréquence définie. Un programme écrit sous Matlab a été utilisé pour traiter les photos, obtenir le champ de déplacement et analyser les résultats. Un intérêt particulier a concerné l'orientation des contacts, le tenseur de fabrique et son évolution durant le chargement. L'impact de certains facteurs clés tels que la densité de compactage, la pression de confinement, la taille des plateaux de chargement, la taille des particules et l'épaisseur des échantillons sur la déformation des échantillons ont été étudiés.

Une attention particulière s'est portée sur les grains subissant une rupture. Nous avons déterminé le nombre de contact sur ces grains et les avons reproduits, dans le modèle numérique (grain 3D) soumis à un chargement diamétral, par le biais de contraintes cinématiques.

Mots-clés: matériau granulaire; rupture de particules; densité de l'assemblage; essais de compression uniaxiale et biaxiale.

L'introduction Fracaise

École doctorale EMMA

THÈSE

Pour l'obtention du titre de :

DOCTEUR DE L'UNIVERSITÉ DE LORRAINE

Spécialité : ingénierie géotechnique

Présentée par : Yuqi ZHANG

Comportement mécanique du matériau granulaire en tenant compte de la rupture des particules

---

Thèse soutenue publiquement le janvier 2018 à Metz devant le jury composé de :

Pierre-Yves HICHER	Professor	Ecole Centrale de Nantes, France	Rapporteur
Belouettar SALIM	DR HDR	Luxembourg Institute of Science and Technology, Luxembourg	Rapporteur
Marion MARTINY	Professor	Université de Lorraine, France	Examinateur
Christophe DANO	MCF	l'Université Grenoble Alpes UGA, France	Examinateur
Nadia BENAHMED	Chargé de Recherche	Irstea, Unité de Recherche RECOVER/Equipe G2DR - FRANCE	Examinateur
Jrad MOHAMAD	MCF	Université de Lorraine, France	Invité
Ali DAOUADJI	Professor	INSA Lyon, France	Directeur
El Mostafa DAYA	Professor	Université de Lorraine, France	Co-Directeur

LEM3 - 7 Rue Félix Savart, 57073 Metz
Université de Lorraine

Résumé

Le comportement mécanique de matériaux granulaires est intrinsèquement lié aux propriétés individuelles des grains constitutifs ainsi qu'à leur assemblage (texture, distribution des vides, contact entre grains…). Soumis à un chargement extérieur, cet assemblage se déforme incluant le déplacement relatif entre les particules mais également la déformation propre des grains jusqu'à leur rupture si elle se produit.

Pour étudier la rupture d'une seule particule, des études expérimentales et numériques ont été réalisées. Quatre particules sphériques formées de billes d'argile expansée légère ont été testées en compression à déplacement contrôlé jusqu'à la rupture (essai brésilien). Des photos ont été prises avec une fréquence d'acquisition de 4 images par seconde pour suivre la déformation des grains durant l'essai. La structure interne d'une particule a une influence significative sur l'initiation de la fissure. Pour approfondir cet effet, une micro-tomographie par rayons X a été utilisé pour scanner une particule afin d'obtenir la structure géométrique réelle en 3D. Ensuite, un modèle numérique 3D basé sur la géométrie des particules incluant la porosité interne a été construit avec Abaqus pour les mêmes conditions de chargement. Une comparaison des résultats des tests de laboratoire et des simulations a été faite. Sur la base des résultats, l'initiation des fissures, leur localisation dans le grain et la classification des ruptures de particules ont été établies.

Afin d'étudier le rôle de l'anisotropie et en particulier de la fabrique d'un matériau granulaire soumis à un chargement externe, cinq essais de compression biaxiaux ont été réalisé sur un assemblage de grains quai-sphériques placés dans une chambre confinée.

Des photos ont été prises pendant les tests et ont été enregistrées selon une fréquence définie. Un programme écrit sous Matlab a été utilisé pour traiter les photos, obtenir le champ de déplacement et analyser les résultats. Un intérêt particulier a concerné l'orientation des contacts, le tenseur de fabrique et son évolution durant le chargement. L'impact de certains facteurs clés tels que la densité de compactage, la pression de confinement, la taille des plateaux de chargement, la taille des particules et l'épaisseur des échantillons sur la déformation des échantillons ont été étudiés.

Une attention particulière s'est portée sur les grains subissant une rupture. Nous avons déterminé le nombre de contact sur ces grains et les avons reproduits, dans le modèle numérique (grain 3D) soumis à un chargement diamétral, par le biais de contraintes cinématiques.

Mots-clés: matériau granulaire; rupture de particules; densité de l'assemblage; essais de compression uniaxiale et biaxiale.

Introduction Générale

Un matériau granulaire est une collection de particules macroscopiques discrètes de morphologie et de propriétés mécaniques différentes. Une caractéristique fondamentale de ce matériau est qu'il y aurait une perte d'énergie entre deux particules lorsqu'elles interagiraient entre elles. Le concept généralisé de matériau granulaire contient des solides, des liquides et des gaz. Cependant, dans cette thèse, le matériau granulaire étudié se réfère seulement à une collection de particules solides qui sont grandes et assez lourdes pour donner à leurs forces d'interaction une dominance par rapport aux forces intermoléculaires. Par conséquent, les liquides et les gaz ne sont pas étudiés dans cette thèse. En outre, les cendres solides qui sont moins cohésives et facilement suspendues dans le gaz en raison de ses minuscules tailles et poids légers ne sont pas considérées dans ce travail.

Le matériau granulaire est omniprésent dans de nombreux domaines. Le sucre, le sel et les céréales sont utilisés dans l'industrie de la transformation des aliments. En outre, le fonctionnement des poudres est également courant dans la fabrication de médicaments dans l'industrie pharmaceutique. Le sable, le sol et la roche font l'objet d'études en génie de la construction ou dans le domaine de l'ingénierie des routes et des ponts, tels que l'excavation des fondations et la pose de la plate-forme. De toute évidence, le comportement mécanique du matériau granulaire est différent de celui d'autres matériaux continus, ce qui peut avoir un impact énorme sur notre vie quotidienne. Par exemple, le barrage de Canoas Novos, au Brésil, était considéré comme le troisième plus haut barrage de remblai en béton au monde et coûtait 6671 millions de dollars. En 2006, l'eau s'est épuisée à la suite d'une rupture dans le mur du barrage. Une des raisons principales était que beaucoup de particules du sol en dessous du fond du barrage ont été écrasées, ce qui a provoqué une réduction de la résistance des fondations.

Jusqu'à présent, plusieurs chercheurs ont étudié le comportement complexe du matériau granulaire. Trois échelles différentes, macroscopique, mésoscopique et microscopique peuvent être utilisées pour étudier ce type de matériau. Jusqu'à présent, la mécanique des sols pourrait être un ensemble de théories sur les matériaux granulaires qui sont suffisamment matures pour être appliquées à résoudre des problèmes d'ingénierie pratiques. Les trois hypothèses de base de la mécanique des sols sont la continuité, l'homogénéité et l'isotrope. Par conséquent, cette théorie est encore disponible sur des échelles macro et mésoscopiques telles que Mohr-Coulomb élastique-idéalement modèle en plastique, modèles hypoplastiques ou élastoplastiques et ainsi de suite. Tous les modèles ci-dessus considèrent le matériau granulaire comme un milieu continu et homogène contenant un nombre infini mais suffisant de particules incassables et inséparables, conduisant à une mauvaise compréhension de la mécanique à l'échelle des particules.

En fait, la propriété des matériaux granulaires dépend aussi de l'échelle des particules qui est plus petite que l'échelle macroscopique, mais plus grande que la dimension atomique. Le comportement du matériau granulaire est fortement influencé par le comportement mécanique des particules individuelles et la disposition relative des vides et des particules. En 1727, Stephen Hales a commencé l'étude des arrangements géométriques d'un ensemble d'objets emballant au hasard. Il a également utilisé les motifs de fossettes sur les pois qui avaient été expansés dans un récipient fermé rempli d'eau. Cependant, le travail de Hales ne soulignait pas le comportement mécanique mais se limitait à la sève des légumes. La première étude d'emballage de matériaux granulaires du point de vue de la mécanique a commencé en 1929 par Furnas. En outre, Jaeger a étudié en 1967. la force de particule unique qui est une propriété fondamentale influençant le comportement du matériau granulaire. Depuis lors, les scientifiques ont examiné le comportement mécanique de particules individuelles en utilisant plusieurs méthodes. En ce qui concerne le comportement mécanique de plusieurs particules, les scientifiques ont découvert que sous une contrainte efficace élevée, des particules pouvaient s'écraser et agir comme un facteur important influençant le comportement physique et mécanique du matériau granulaire.

Dans la présente étude, des expériences et des simulations ont été effectuées pour étudier le comportement mécanique du matériau granulaire à l'échelle des particules en tenant compte des ruptures de particules et des arrangements de particules. Spécifiquement, des particules presque sphériques faites par de l'argile expansée seraient les échantillons expérimentaux. Grâce à des méthodes expérimentales et numériques, le comportement mécanique d'une seule particule en tenant compte de la rupture des particules sous l'influence de la pression serait étudié. Le tissu caractéristique d'un empilement de particules sphériques sera étudié avec une méthode expérimentale et analysé par un logiciel écrit avec le code MATLAB. Le comportement mécanique et cinématique de plusieurs particules en cas de charge biaxiale serait étudié.

Dans le premier chapitre, les antécédents de recherche et les conditions actuelles dans les domaines impliqués dans la thèse ont été passés en revue. Les théories de base utilisées dans les chapitres suivants seraient présentées.

Dans le deuxième chapitre, des essais de compression uniaxiale seraient effectués sur des particules individuelles approximativement sphériques. La technologie μ-CT sera appliquée pour construire la géométrie de la particule. La géométrie serait maillée et importée dans Abaqus pour une simulation plus poussée. Des comparaisons et des analyses seraient faites sur les résultats des tests de laboratoire et des simulations.

Dans le troisième chapitre, des tests biaxiaux seraient effectués sur plusieurs groupes de particules qui étaient placés dans une chambre de déformation plane composée de PMMA. Des photos ont été prises pour enregistrer les tests. Le logiciel a été compilé avec le code Matlab pour analyser le tissu de l'emballage du matériau granulaire lors de l'exécution de la charge biaxiale.

Dans le quatrième chapitre, des tests biaxiaux seraient effectués sur plusieurs groupes de particules avec différents paramètres de test. Des photos ont été prises pendant le processus des tests. Le comportement mécanique a été observé à partir des tests. Un logiciel compilé avec du code Matlab a été utilisé pour tracer le déplacement de chaque particule dans chaque test afin d'étudier la caractéristique cinématique de multiples particules sous un chargement biaxial.

Dans le cinquième chapitre, une conclusion serait faite de l'ensemble de la thèse et une prospective serait décrite.

Résultats des essais de compression uniaxiale

Certains essais de compression uniaxiale sur des particules uniques ont été développés. La technologie de tomographie par rayons X a été utilisée pour capturer la structure interne d'une particule. La géométrie 3D reconstruite de la particule a été importée dans Abaqus pour construire un modèle 3D d'une particule réelle. Les résultats de la particule réelle sont comparés aux résultats d'une particule idéale.

Les modèles de défaillances observées d'une particule sphérique peuvent être divisés en deux catégories selon l'origine de la fissure, à savoir la défaillance du haut et du bas et la défaillance du centre (Tableau 1).

S_1	Photo				
	Charge(N)	1.255	149.5	316.7	918.7
	Déplacement (mm)	0.005	0.300	0.600	1.081
S_2	Photo	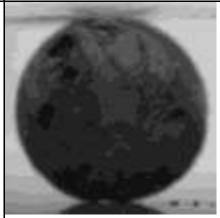	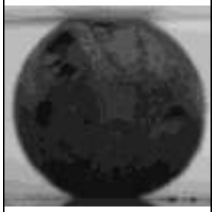	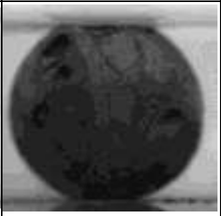	
	Charge (N)	1.929	222.8	396.2	573.2
	Déplacement (mm)	0.002	0.500	1.019	1.743

S_3	Photo	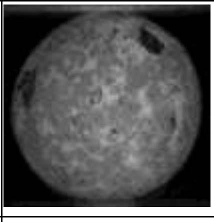	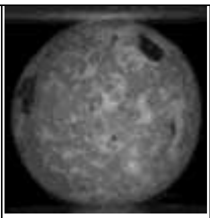	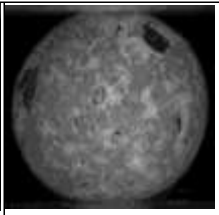	
	Charge (N)	3.064	125.6	253.78	450.7
	Déplacement (mm)	0.003	0.201	0.401	0.677
S_4	Photo	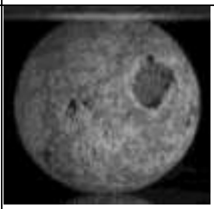	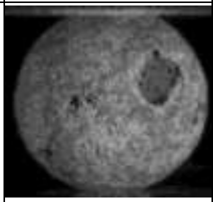	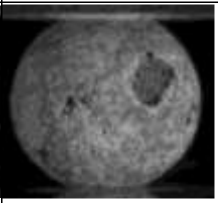	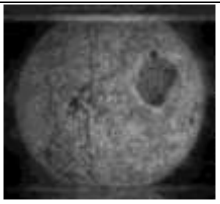
	Charge (N)	1.283	183.1	360.1	583.5
	Déplacement (mm)	0.002	0.302	0.601	1.032

Tableau 1 Breakage information of each single particle test

Lorsque la particule s'est rompue en haut et en bas, elle est apparue dès le début du test. Ce type de défaillance peut entraîner la génération de deux plans circulaires et est causé par des dommages de traction et des dommages de compression. L'endommagement à la traction se situe sur la limite du plan circulaire à partir du début de l'essai. Cependant, le temps d'apparition et l'emplacement des dommages de compression sont selon que la particule est une sphère idéale ou non. Les dommages de compression apparaissent quand et où la déformation plastique équivalente à la compression (PEEQ) atteint une certaine valeur. Si la particule est une sphère idéale, elle apparaît à environ ¼ des rayons au-dessous de la surface de contact avec la machine de chargement. Néanmoins, si la particule n'est pas une sphère idéale, la concentration des contraintes causée par certains défauts peut amener le PEEQ à atteindre la valeur limite à l'avance. Même s'il y a des protubérances aiguës à la surface de la particule, les dommages de compression peuvent apparaître au début du test.

Pour le second type d'échec, les fissures se développent au centre si la particule est une sphère parfaite et proche du centre si ce n'est pas le cas. Ce type de défaillance est causé par des dommages de traction. Lorsque la déformation plastique équivalente à la traction atteint la valeur limite, la rupture apparaît et augmente ensuite progressivement avec la déformation de la particule. Ce processus ne peut pas être observé de l'extérieur de la particule jusqu'à ce que la zone de la lésion de traction atteigne un certain volume lorsque certaines fissures verticales apparaissent soudainement et séparent la particule en plusieurs parties.

Pour l'échec du haut et du bas, c'est un échec local du début à la fin. Cependant pour l'échec du centre, c'est un échec local quand il apparaît et se développe graduellement mais finalement il pourrait mener à une panne globale. (Fig 1et Fig 2)

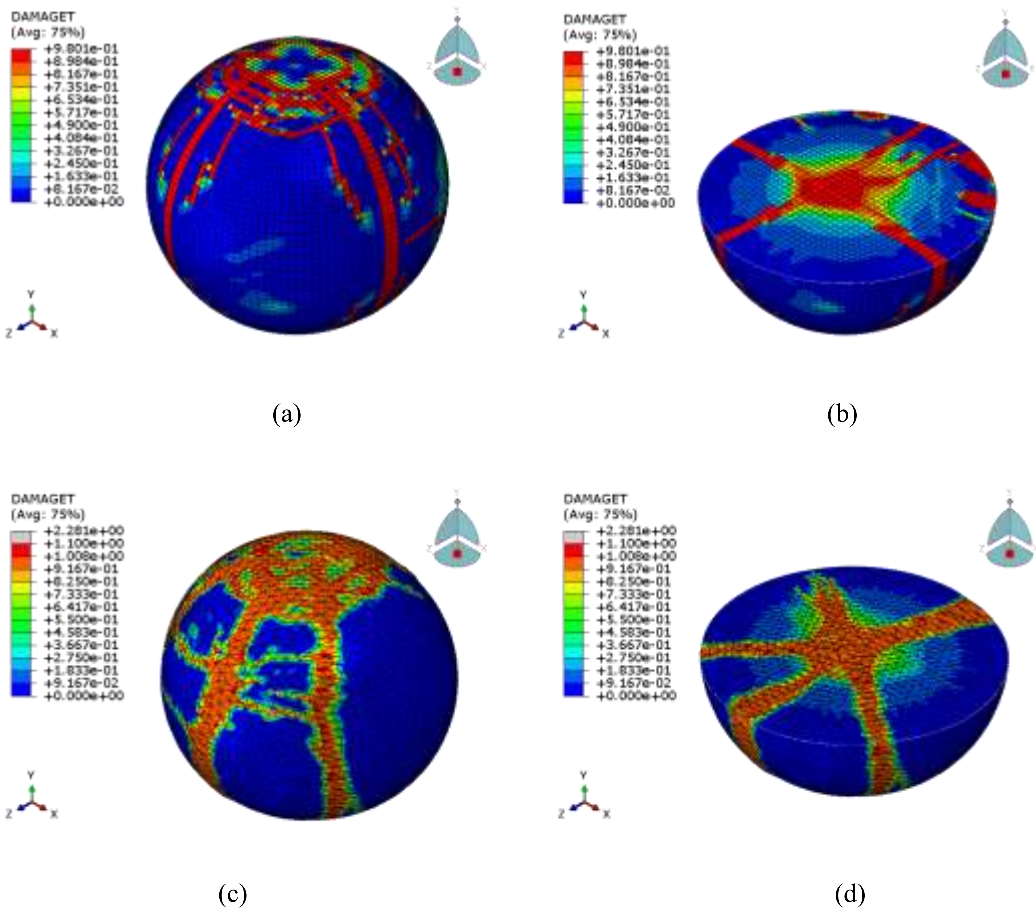

(a)(b) État d'échec de Model 1-1. (c)(d) État d'échec de Model 1-2

Fig 2 Failure state of simulation

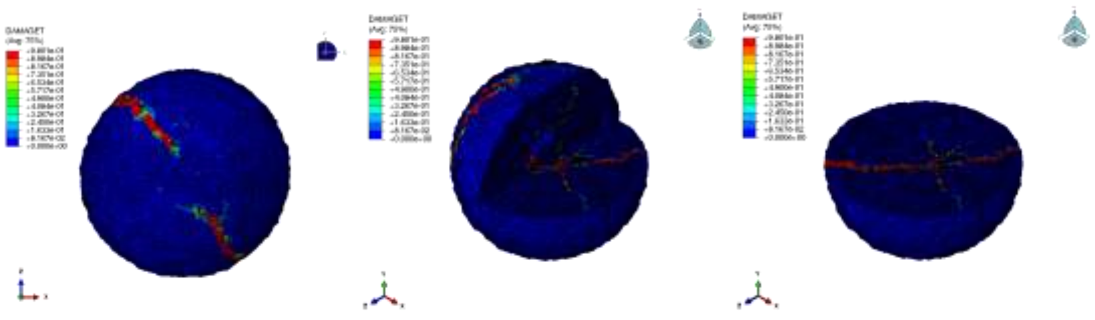

Fig 2 État d'échec de Model 1-3 de différents angles de vue

Si la particule a un plus grand nombre de coordination, la défaillance globale se produit plus rapidement parce que l'environnement de chargement complexe pourrait faire que le PEEQT au centre de la particule augmente plus rapidement.

Le plan de fissure qui a causé une défaillance globale doit contourner le centre de la particule et doit être parallèle à la direction de chargement. Ainsi, pour la particule à charge nue uniquement à partir de la direction verticale, il est impossible de prévoir la direction du plan de fissure uniquement avec la condition d'essai. Il est également possible qu'il existe plusieurs plans de fissure pour séparer la particule en plusieurs parties. Mais pour la charge de mise à nu des particules de plus d'une direction, comme le Model 2-2, Model 2-3, Model 2-4 dans l'ensemble 2, la direction du plan de fissure pourrait être ridée et il n'y aurait qu'un seul plan de fissure (Fig 3).

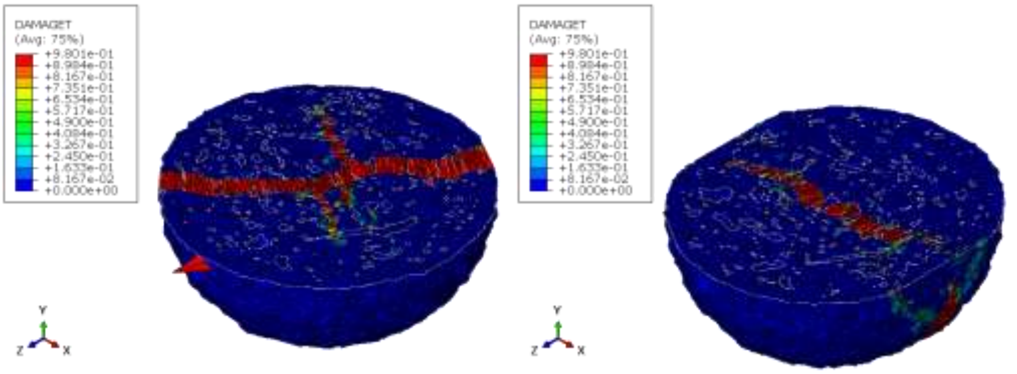

(a) Model 2-1 (b) Model 2-2

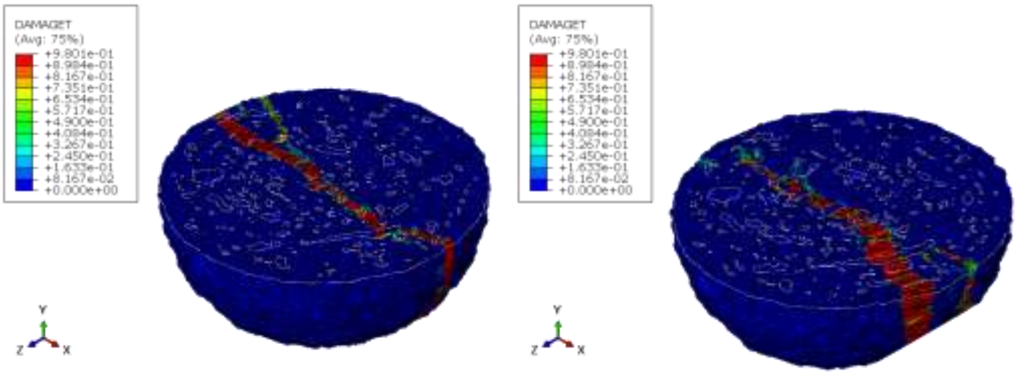

(c) Model 2-3 (d) Model 2-4

Fig 3 Les fissures des quatre modèles

Résultats des essais de compression biaxiale

L'objectif de cette partie est d'illustrer l'impact de divers facteurs sur la caractéristique d'emballage. Afin d'atteindre cet objectif, une Plane Strain Chamber (PSC) est assemblée pour les tests (Fig 4). Cinq essais de compression biaxiale ont été effectués sur des particules approximativement sphériques et des photos ont été prises pour enregistrer la procédure expérimentale. Un logiciel écrit avec du code MATLAB a été appliqué pour analyser les photos et calculer divers paramètres. Un paramètre appelé facteur d'orientation est introduit pour analyser les orientations de contact. Enfin, certaines conclusions pourraient être tirées.

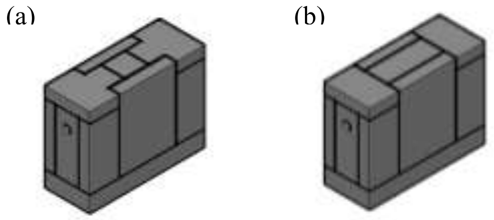

Fig 4 Image 3D de tous les composants et combinaisons des deux types de PSC

(a) Chambre assemblée avec une petite couverture (b) Chambre assemblée avec une grande couverture

Après un processus de remplissage vibré, les particules dans nos tests pourraient presque atteindre chaque statut d'emballage optimal. Les actions de chargement après cela ne pouvaient pas rendre l'emballage plus dense. Au lieu de cela, la perturbation de la couverture pourrait rendre l'emballage plus lâche. En raison des sacs en caoutchouc sur les côtés gauche et droit, l'utilisation d'un petit couvercle pourrait provoquer les jonctions du couvercle et les sacs en caoutchouc n'étaient pas assez proches, ce qui pourrait conduire à une densité plus faible des particules. Mais cet effet a disparu progressivement au fur et à mesure des tests. Lorsque la pression de confinement n'est pas très grande, l'augmentation de la pression de confinement peut conduire à un compactage plus dense des particules. Mais avec la croissance de la pression de confinement, la même différence de pression entraînerait une différence de densité de garnissage de plus en plus faible. Quatrièmement, dans nos essais, les densités de compactage des particules polysized sont plus petites que celles des particules monosized. Parce que les écarts de diamètre entre les particules de taille différente ne sont pas assez grands. La plus petite particule ne pouvait pas remplir le vide entre les plus grands. Au lieu de cela, ils vont séparer les plus grands et donner lieu à une densité d'emballage plus faible (Fig 4 et Fig 5).

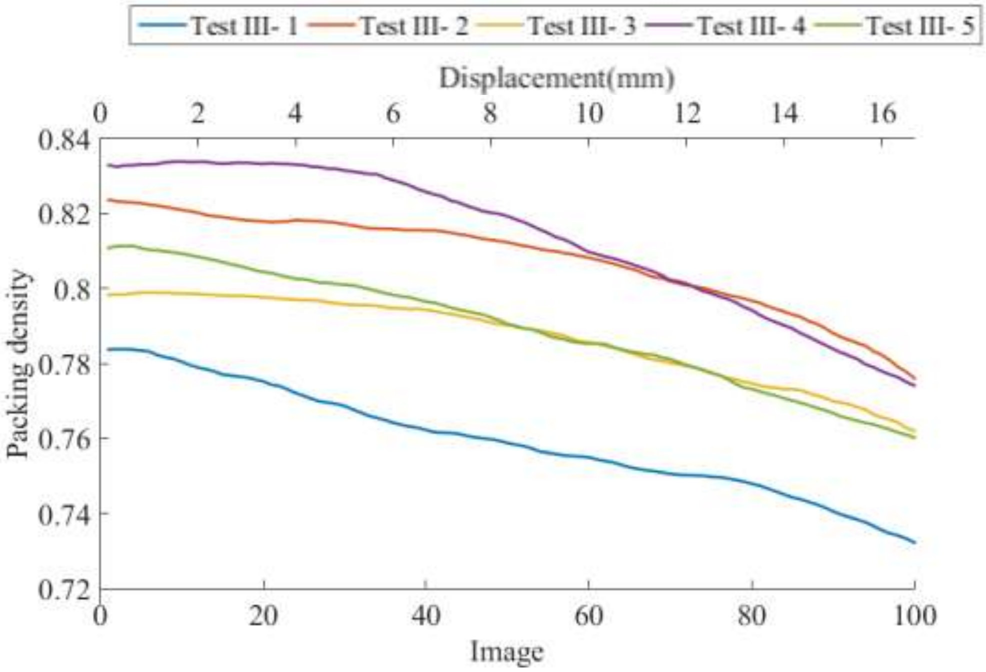

Fig 4 Evolution de la densité d'emballage des tests

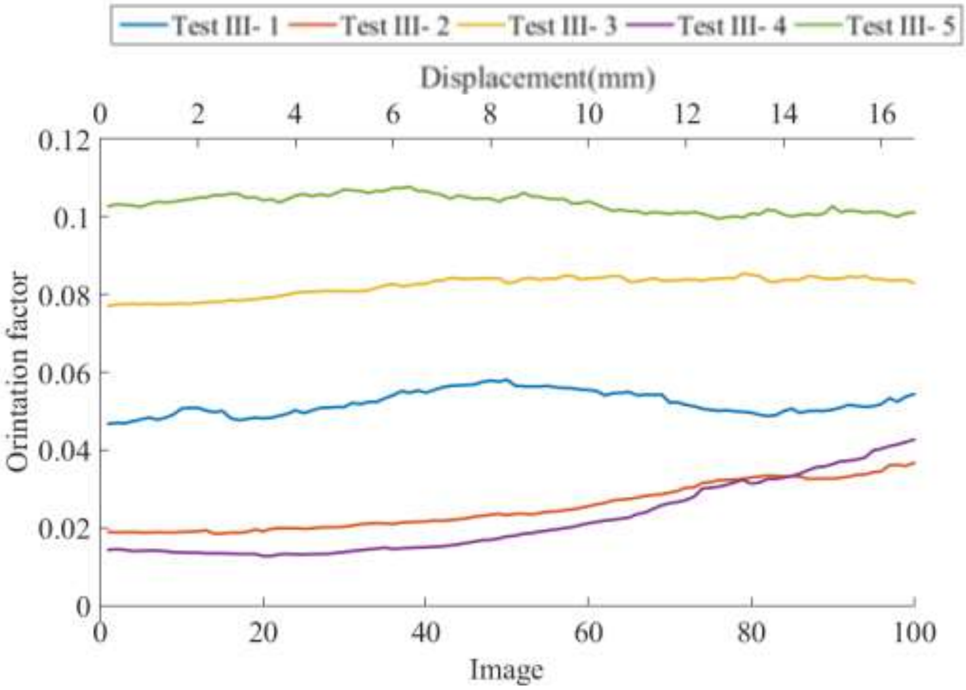

Fig 5 Facteurs d'orientation des tests de laboratoire

L'emballage sur les parties supérieures et inférieures présente également certaines différences. Brièvement, la densité d'empaquetage sur la partie supérieure est inférieure à celle de la partie inférieure en raison de l'effet de vibration différent lors du remplissage du PSC et de l'effet de perturbation différent du couvercle pendant le chargement (Tableau 2).

image	Déplacement (mm)	Entier	Haut	Bas
1	1/6	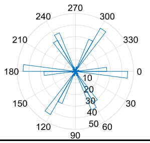	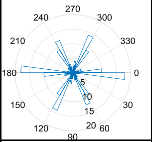	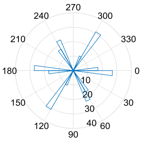
10	10/6	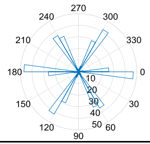	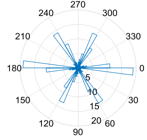	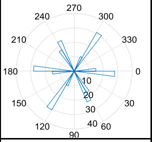
20	20/6	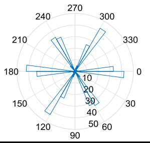	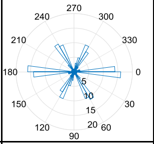	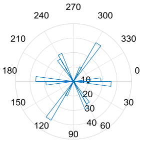
30	30/6	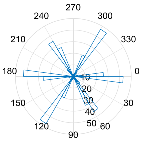	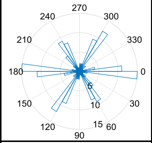	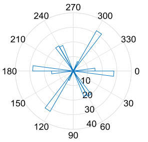
40	40/6	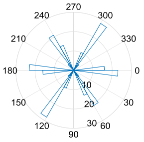	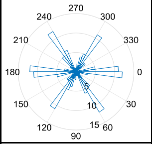	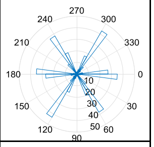
50	50/6	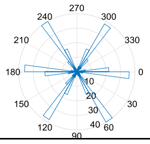	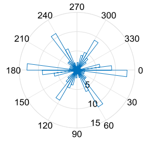	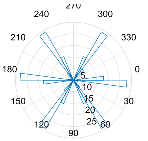
60	60/6	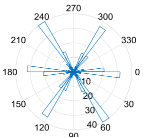	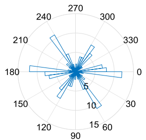	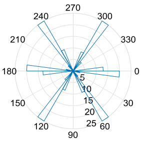
70	70/6	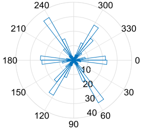	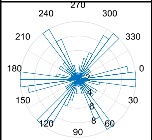	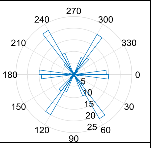
80	80/6	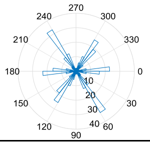	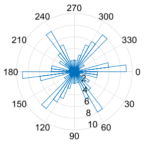	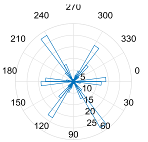
90	90/6	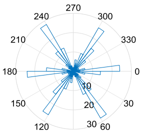	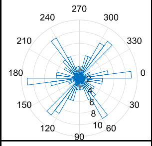	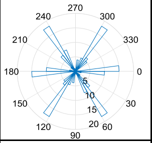
100	100/6	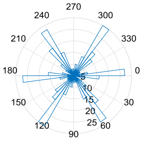	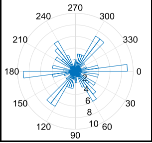	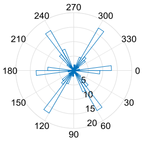

Tableau 2 Roses courbes de différentes parties de Test III-4

Deux facteurs pourraient provoquer une augmentation du pic de la charge avec le même déplacement, l'augmentation de la taille du couvercle et la pression de confinement. Pendant le processus de chargement, si les particules ont été soumises en raison de l'effet de la charge de la couverture, de la gravité, de la pression de confinement et de la réaction de dénudation de la CFP. Par conséquent, une plus grande surface de contact de la plus grande couverture pourrait entraîner une plus grande charge. Une pression de confinement croissante pourrait conduire à un stress croissant, contribuant finalement à une charge croissante. Pendant les essais, la tendance de variation de la charge augmente. Mais s'il y a rupture de particules ou mouvement soudain de particules ou rotation, il y aurait une chute sur la courbe. (Fig 6)

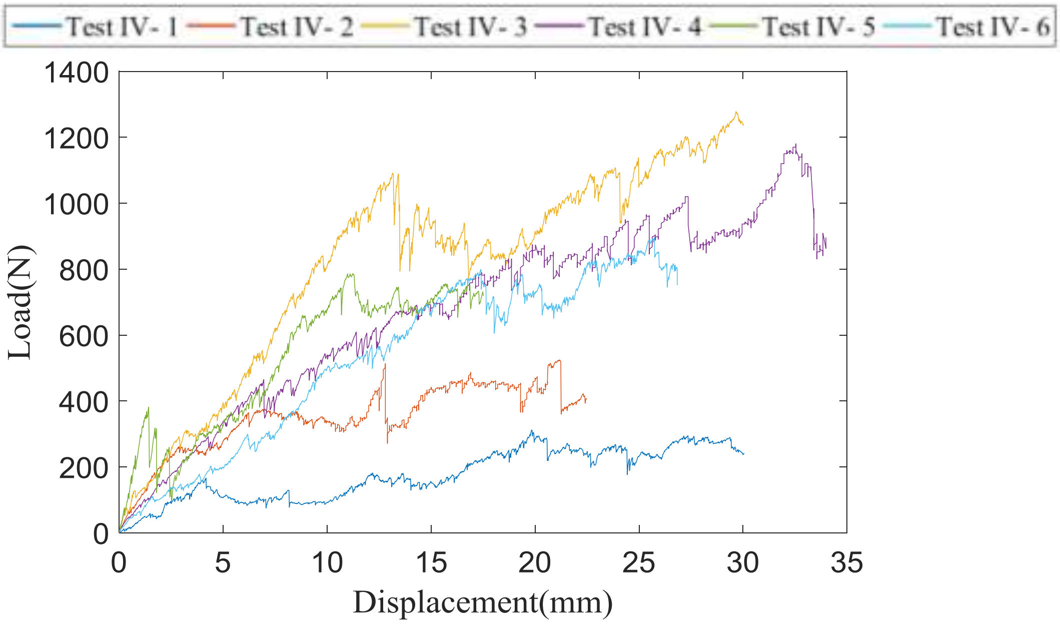

Fig 6 La courbe Load-Displacement des 6 tests

Après les tests, certaines particules peuvent tomber en panne pendant les tests. Donc, une analyse avait été faite pour comprendre la raison de la défaillance des particules. Il a été conclu que, avec une forte pression de confinement, les particules ont une grande probabilité de défaillance car l'augmentation de la contrainte de confinement pourrait conduire à une augmentation de la contrainte à l'intérieur des particules. De plus, les particules situées dans la zone triangulaire sous la couverture ont un stress plus important et ont une plus grande probabilité d'échouer. Une défaillance d'une particule influencerait l'empilement des particules environnantes. Pour être précis, cela entraînerait une diminution de la coordination et de la densité de l'emballage.

La caractéristique de déplacement des particules lors de l'application d'une charge verticale est également étudiée. Les vecteurs de déplacement de toutes les particules pourraient être séparés en composants verticaux et en composants horizontaux. Les directions des composants horizontaux sont vers l'extérieur de l'assemblage de particules. De plus, les amplitudes des composantes horizontales augmentent avec la diminution de la pression de confinement. En ce qui concerne l'amplitude de la composante verticale, l'augmentation de la taille de la couverture et de la pression de confinement pourrait entraîner une augmentation des amplitudes des composantes verticales (Tableau 3).

Image	Dis(mm)	Test IV-1	Test IV-2	Test IV-3	Test IV-4	Test IV-5	Test IV-6
10	10/6	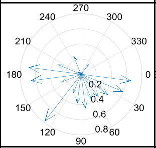	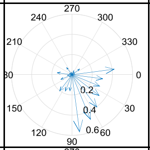	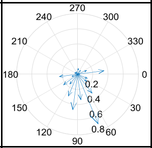	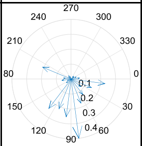	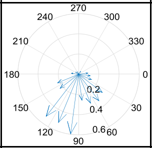	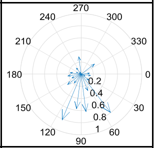
20	20/6	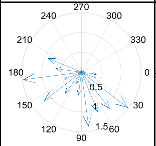	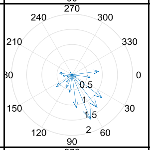	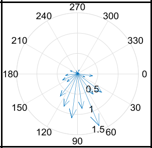	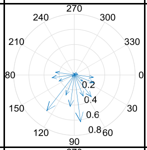	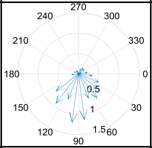	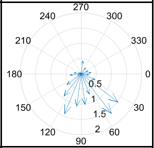
30	30/6	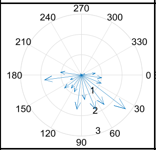	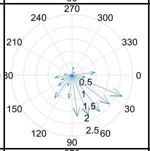	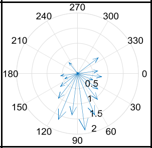	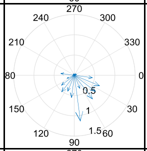	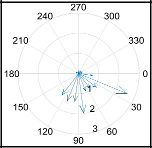	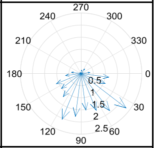
40	40/6	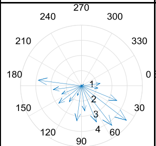	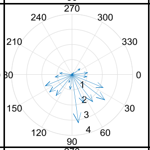	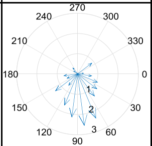	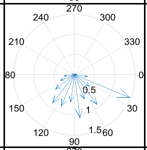	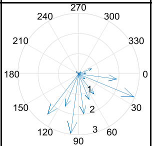	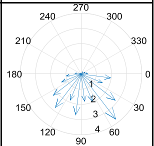
50	50/6	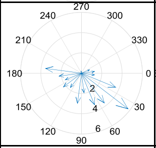	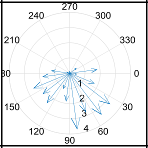	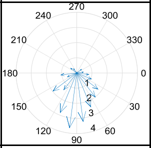	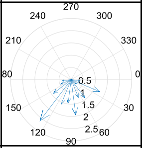	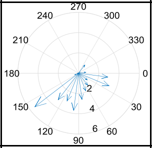	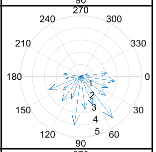
60	60/6	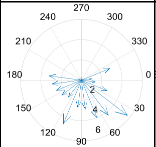	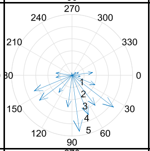	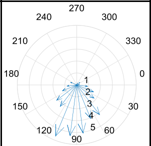	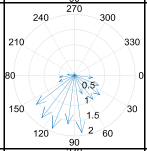	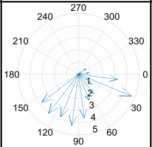	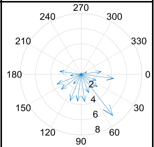
70	70/6	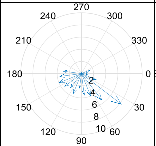	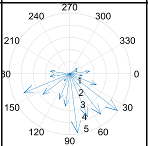	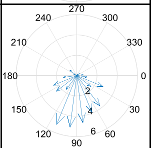	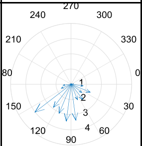	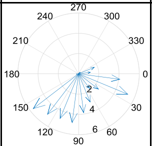	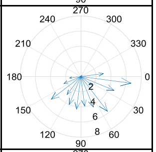
80	80/6	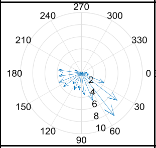	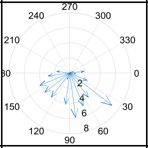	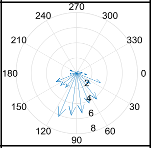	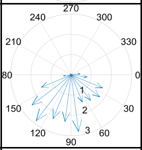	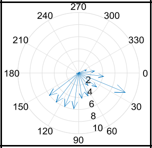	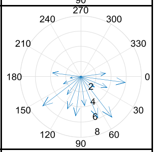
90	90/6	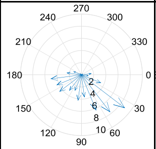	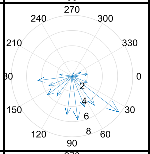	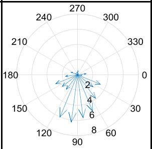	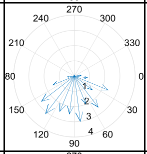	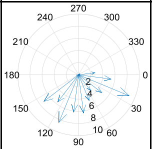	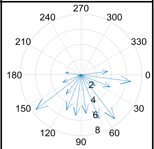
100	100/6	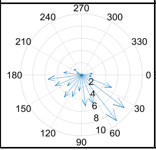	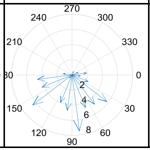	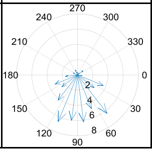	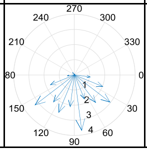	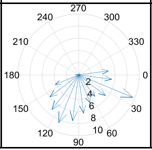	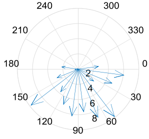

Tableau 3 Les vecteurs de déplacement des six tests